Uenzelmann-Neben, G., Bohaty, S.M., Childress, L.B., and the Expedition 392 Scientists
Proceedings of the International Ocean Discovery Program Volume 392
publications.iodp.org

Expedition 392 summary[1]

G. Uenzelmann-Neben, S.M. Bohaty, L.B. Childress, O.A. Archontikis, S.J. Batenburg, P.K. Bijl, A.M. Burkett, H.C. Cawthra, P. Chanda, J.J. Coenen, E. Dallanave, P.C. Davidson, K.E. Doiron, J. Geldmacher, D. Gürer, S.J. Haynes, J.O. Herrle, Y. Ichiyama, D. Jana, M.M. Jones, C. Kato, D.K. Kulhanek, J. Li, J. Liu, J. McManus, A.N. Minakov, D.E. Penman, C.J. Sprain, A.C. Tessin, T. Wagner, and T. Westerhold[2]

[1] Uenzelmann-Neben, G., Bohaty, S.M., Childress, L.B., Archontikis, O.A., Batenburg, S.J., Bijl, P.K., Burkett, A.M., Cawthra, H.C., Chanda, P., Coenen, J.J., Dallanave, E., Davidson, P.C., Doiron, K.E., Geldmacher, J., Gürer, D., Haynes, S.J., Herrle, J.O., Ichiyama, Y., Jana, D., Jones, M.M., Kato, C., Kulhanek, D.K., Li, J., Liu, J., McManus, J., Minakov, A.N., Penman, D.E., Sprain, C.J., Tessin, A.C., Wagner, T., and Westerhold, T., 2023. Expedition 392 summary. In Uenzelmann-Neben, G., Bohaty, S.M., Childress, L.B., and the Expedition 392 Scientists, Agulhas Plateau Cretaceous Climate. Proceedings of the International Ocean Discovery Program, 392: College Station, TX (International Ocean Discovery Program). https://doi.org/10.14379/iodp.proc.392.101.2023
[2] **Expedition 392 Scientists' affiliations.**

Contents

Keywords
International Ocean Discovery Program, IODP, *JOIDES Resolution*, Expedition 392, Agulhas Plateau Cretaceous Climate, Climate and Ocean change, Earth Connections, Site U1579, Site U1580, Site U1581, Site U1582, Cretaceous/Paleogene boundary, K/Pg boundary, Paleocene/Eocene Thermal Maximum, PETM, large igneous province, LIP, zeolite authigenesis, igneous sill intrusion, Campanian, Oligocene pelagic carbonates, paleoceanography, African–Southern Ocean gateway

Core descriptions

Supplementary material

References (RIS)

MS 392-101
Published 19 August 2023

Funded by NSF OCE1326927

Abstract

During International Ocean Discovery Program Expedition 392, three sites were drilled on the Agulhas Plateau and one site was drilled in the Transkei Basin in the Southwest Indian Ocean. This region was positioned at paleolatitudes of ~53°–61°S during the Late Cretaceous (van Hinsbergen et al., 2015) (100–66 Ma) and within the new and evolving gateway between the South Atlantic, Southern Ocean, and southern Indian Ocean basins. Recovery of basement rocks and sedimentary sequences from the Agulhas Plateau sites and a thick sedimentary sequence in the Transkei Basin provides a wealth of new data to (1) determine the nature, origin, and bathymetric evolution of the Agulhas Plateau; (2) significantly advance the understanding of how Cretaceous temperatures, ocean circulation, and sedimentation patterns evolved as CO_2 levels rose and fell and the breakup of Gondwana progressed; (3) document long- and short-term paleoceanographic variability through the Late Cretaceous and Paleogene; and (4) investigate geochemical interactions between igneous rocks, sediments, and pore waters through the life cycle of a large igneous province (LIP). Importantly, postcruise analysis of Expedition 392 drill cores will allow testing of competing hypotheses concerning Agulhas Plateau LIP formation and the role of deep ocean circulation changes through southern gateways in influencing Late Cretaceous–early Paleogene climate evolution.

1. Introduction

The warmest sustained greenhouse episode of the past ~150 My occurred during the mid-Cretaceous between ~95 and 80 Ma (e.g., Clarke and Jenkyns, 1999; Friedrich et al., 2012; Huber et al., 2018, 2002). Proxy data and climate models suggest CO_2 levels during this supergreenhouse interval may have been as high as 3500 parts per million by volume (ppmv) before declining to less than 560 ppmv following the Eocene–Oligocene transition (EOT) at ~34 Ma (Berner et al., 1983; Bice et al., 2006; DeConto and Pollard, 2003; Royer et al., 2004). High- and mid-latitude temperatures were exceptionally warm during the prolonged period of elevated CO_2 levels in the mid-Cretaceous, resulting in low meridional temperature gradients (Bice et al., 2006, 2003; Forster et al., 2007; Huber et al., 1995). However, Cretaceous warmth was also interrupted by periods of rapid global climate change during deposition of oceanic anoxic events (OAEs), which were associated with widespread reduction in basin ventilation and major changes in ocean temperature, hydrology, and circulation (Arthur et al., 1985, 1987; Jenkyns, 2003, 2010; Schlanger and Jenkyns, 1976; Sinninghe Damsté et al., 2010). The timing, magnitude, and oceanographic and ecological consequences of the Cretaceous greenhouse warming are poorly documented in the southern

high latitudes. Furthermore, greenhouse climate conditions with CO_2 levels approaching those of the Cretaceous–Paleogene interval are predicted for the near future (Intergovernmental Panel on Climate Change, 2022), highlighting the value of using Cretaceous–Paleogene records to better understand the operation of the Earth system in greenhouse periods.

Expedition 392 drill sites on the Agulhas Plateau and Transkei Basin were located at mid to high latitudes during the Late Cretaceous (65°–58°S) (Hay et al., 1999; Sewall et al., 2007; Tetley et al., 2019) and positioned in the gateway between the newly opening South Atlantic, Southern Ocean, and southern Indian Ocean basins. Climate models indicate significant regional cooling arising from the Cenozoic opening of Southern Ocean gateways, pointing toward a progressive deepening of southern gateways and eventual strengthening of the Antarctic Circumpolar Current (ACC) as the major cause for cooler deep ocean temperatures (Sijp et al., 2014; Toggweiler and Russell, 2008). Analogous arguments point to a critical role for deep circulation in controlling Late Cretaceous climate evolution (e.g., Frank et al., 1999; MacLeod and Huber, 1996; Robinson and Vance, 2012; Voigt et al., 2013). Therefore, because of its position at the narrow junction between the Indian and Atlantic oceans and expanding Southern Ocean, basement and sedimentary records recovered during Expedition 392 from the Agulhas Plateau will allow direct testing of these models through precise determination of the timing of large igneous province (LIP) volcanism and emplacement of the plateau and its subsequent paleoceanographic history, including documentation of ocean temperature, circulation, and sedimentation patterns during the Cretaceous and Paleogene.

2. Background

2.1. Geological setting

2.1.1. Tectonic history of the African–Southern Ocean gateway

During the Early Cretaceous, the African–Southern Ocean gateway was closed and the South American, African, and Antarctic continents were connected (Figure **F1**). Breakup of this region of Gondwana commenced at ~146 Ma and was associated with the formation of two oceanic plateaus (Figure **F1**): the Mozambique Ridge (~136–120 Ma) and the Agulhas Plateau (105–95 Ma) (Gohl and Uenzelmann-Neben, 2001; Gohl et al., 2011; König and Jokat, 2010; Parsiegla et al., 2008; Uenzelmann-Neben et al., 1999). These seafloor elevations constituted barriers for circulation of deep and intermediate water masses as indicated by neodymium (Nd) isotopic evidence for different water masses bathing the Falkland Plateau and the western flank of the Kerguelen Plateau between ~95 and 78 Ma (Murphy and Thomas, 2012, 2013). A deepwater connection between the South Atlantic and the Indian Ocean opened with the separation of the Falkland Plateau from Africa between ~120 and 100 Ma (König and Jokat, 2010).

The origin and development of structural units in the African–Southern Ocean gateway (Agulhas Plateau, Mozambique Ridge, Maud Rise, Astrid Ridge, Madagascar Ridge, and Gunnerus Ridge) are heavily debated. Seismic studies and plate tectonic reconstructions suggest that the Agulhas Plateau is a LIP that formed no earlier than 105 Ma (Parsiegla et al., 2008) in combination with the Northeast Georgia Rise and Maud Rise (Gohl and Uenzelmann-Neben, 2001; König and Jokat, 2010; Parsiegla et al., 2008; Uenzelmann-Neben et al., 1999). In contrast, Gohl et al. (2011) suggested the existence of a southeast African super-LIP between ~140 and 95 Ma, which formed as a result of an intense period of magmatism (Charvis et al., 1995; Fischer, 2017; Gohl and Uenzelmann-Neben, 2001; Jacques et al., 2019) and consisted of the Northeast Georgia Rise, Agulhas Plateau, Maud Rise, Astrid Ridge, Mozambique Ridge, and Transkei Rise. This southeast African super-LIP is conjectured to be the same size and age as the Kerguelen-Heard LIP. It is unclear whether this LIP includes continental fragments, and the formation age of this super-LIP, as well as its later separation into Mozambique Ridge, Astrid Ridge, Northeast Georgia Rise, Agulhas Plateau, and Maud Rise, remain unresolved.

2.1.2. African–Southern Ocean gateway circulation

In the Cretaceous greenhouse world, the role of oceanic poleward heat transport as a main driver of long-term climate change is uncertain. Low latitudinal thermal gradients may have affected pat-

terns of runoff and evaporation, which may have shifted areas of deepwater formation. Additionally, constricted interbasin connections could have led to largely internal circulation of deepwater masses in relatively small, enclosed Cretaceous oceanic basins (120–80 Ma) (Friedrich et al., 2008; MacLeod et al., 2011, 2008). Numerical simulations of Cretaceous (Albian and Cenomanian/Turonian boundary) circulation predict no overturning circulation in the African–Southern Ocean gateway, although weak circulation connecting the Pacific, Atlantic, and Indian Ocean basins is indicated (Uenzelmann-Neben et al., 2017). Cooling due to atmospheric CO_2 reduction through the Late Cretaceous, perhaps stimulated by enhanced carbon burial (Robinson et al., 2010; Robinson and Vance, 2012) and/or evolving tectonic barriers via the formation of oceanic plateaus (Frank and Arthur, 1999), may have altered southern high-latitude circulation patterns, and the resulting redistribution of heat may have had regional consequences for climate as well. Better depth-resolved, empirical constraints on circulation coupled with modeling experiments from critical regions like the southwest Indian Ocean are needed to test and refine these hypotheses.

In the Agulhas Plateau region today, surface and deep currents transport warm and salty waters through the African–Southern Ocean gateway from the Indian Ocean into the southern Atlantic Ocean via the Agulhas Current and Agulhas rings, whereas cold water flows eastward into the Indian Ocean (Figure **F2**) (de Ruijter et al., 1999, 2006; Lutjeharms, 1996, 2006; Lutjeharms and Ansorge, 2001; Mantyla and Reid, 1995; Read and Pollard, 1999; Tomczak and Godfrey, 1994;

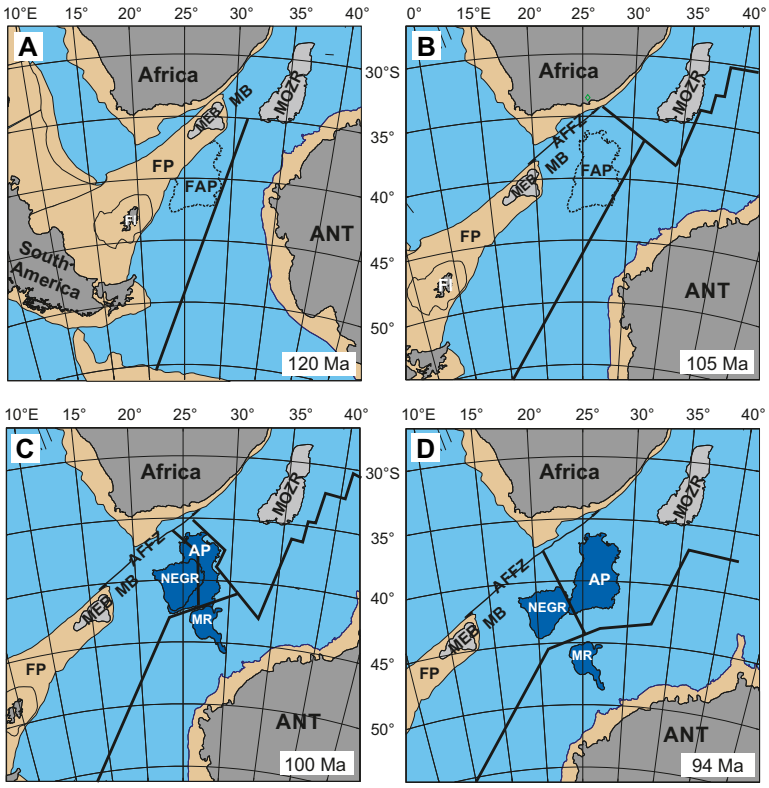

Figure F1. Plate tectonic reconstructions using rotation poles published by Parsiegla et al. (2008). Rotation was performed with respect to Africa, thus the paleolatitude of the Agulhas Plateau may not be correct; it was likely higher. Thick lines = estimated location of paleospreading system (black = spreading axis). MB = Maurice Ewing Basin, MOZR = Mozambique Ridge, FAP = future position of Agulhas Plateau (AP), ANT = Antarctica, FI = Falkland Islands, AFFZ = Agulhas-Falkland Fracture Zone. A. 120 Ma. AP region was still occupied by Falkland Plateau (FP) with Maurice Ewing Bank (MEB) leaving no space for evolution of AP at this time. B. 105 Ma. AP region was cleared. This is the first possibility for formation of AP. C. 100 Ma. Reconstructions of AP, Northeast Georgia Rise (NEGR), and Maud Rise (MR) (with recent boundaries) show overlap between AP and NEGR, which is due to different dimensions of these structures at 100 Ma. D. 94 Ma. Formation of entire LIP (AP, NEGR, and MR) is complete. Bouvet triple junction is located at southwest tip of AP (Marks and Tikku, 2001), and subsequent spreading causes separation of the three fragments of the AP-NEGR-MR LIP. Reproduced from Parsiegla et al. (2008). By permission of Oxford University Press on behalf of the Royal Astronomical Society. This figure is not included under the Creative Commons CC-BY 4.0 license of this publication. For permissions, please email journals.permissions@oup.com.

Toole and Warren, 1993; van Aken et al., 2004; You et al., 2003). Water mass exchange in this region is controlled by seafloor topography, requiring a deep and wide gateway. Lutjeharms (1996, 2006) observed that the Agulhas Current hugs the shelf break of the Agulhas Passage and the path of Agulhas rings is influenced by the Agulhas Ridge topography. Both the Agulhas Current and Agulhas rings maintain the energy transfer between the Indian and Atlantic Oceans (Biastoch et al., 2008, 2009). Seafloor features such as the Mozambique Ridge and Agulhas Plateau constitute barriers for the flow of these oceanic currents and lead to modifications in flow paths.

During the Cretaceous, the presence of large magmatic obstructions is hypothesized to have caused constriction of the African–Southern Ocean gateway and hence hindered water mass exchange between the Atlantic and Indian basins. There are two possible ways that LIP formation complicated the opening of the African–Southern Ocean gateway: (1) a southeast African super-LIP (140–95 Ma) (Gohl et al., 2011) or (2) the formation of two LIPs between 140 and 120 Ma (Mozambique Ridge and Astrid Ridge) (König and Jokat, 2010) and 105 and 95 Ma (Northeast Georgia Rise, Agulhas Plateau, and Maud Rise) (Parsiegla et al., 2008; Uenzelmann-Neben et al., 1999). The second hypothesis allows deepwater circulation between the Tethys/Indian Ocean and Southern Ocean/South Atlantic from ~120 Ma onward. Convergence of Falkland and Kerguelen intermediate water masses may have then initiated following tectonic subsidence of the intervening barriers in the Southern Ocean basin. Therefore, instead of the gateway slowly opening and allowing increasingly deeper water mass exchange, geophysical studies (Fischer et al., 2016; Gohl et al., 2011; König and Jokat, 2010; Schlüter and Uenzelmann-Neben, 2008a) indicate prolonged restricted circulation in the opening gateway (e.g., Transkei Basin). In this model, only surface current flow occurred between the Tethys/Indian Ocean and the evolving Southern Ocean/South Atlantic, whereas deep and intermediate water masses were blocked by this barrier. With the full clearance of the South American plate and the separation of the Agulhas Plateau–Northeast Georgia Rise–Maud Rise LIP into three parts (Figure **F1**), changes in the seafloor topography may have allowed open-ocean circulation across the African–Southern Ocean gateway by ~94 Ma. However, the question remains in which direction the resulting surface ocean flow was directed. To test this proposed history, drilling of Cretaceous basement and sediments from the Agulhas Plateau during Expedition 392 was intended to provide constraints on the timing and nature of African–Southern Ocean gateway evolution from the onset of Agulhas Plateau–Northeast Georgia Rise–Maud Rise LIP formation (younger than 105 Ma) to a fully open gateway (~94 Ma) (König and Jokat, 2010; Parsiegla et al., 2008). Recovery of sediments on the Agulhas Plateau and in the Tran-

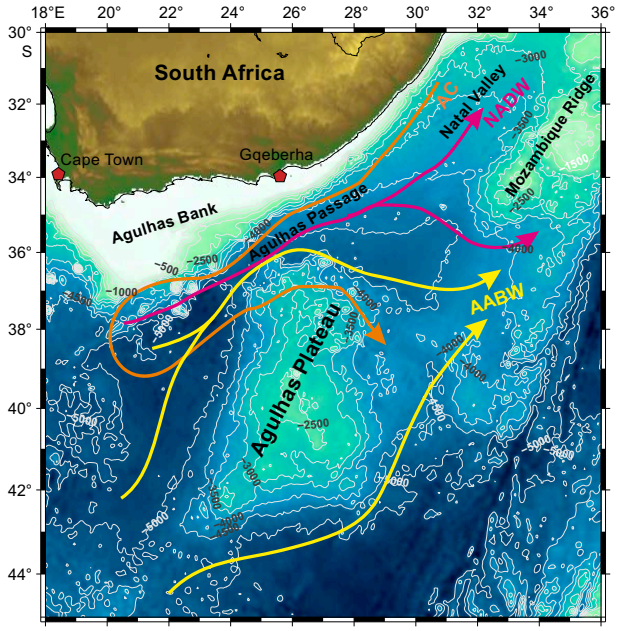

Figure F2. Currents and water masses active in the African–Southern Ocean gateway. AC = Agulhas Current, NADW = North Atlantic Deep Water, AABW = Antarctic Bottom Water.

skei Basin were further intended to provide long records of changing paleodepth, paleoceanography, and paleoclimate spanning the mid-Cretaceous through the Paleogene, documenting the formation of the plateau in presumed subaerial or shallow-water environments and its subsidence to bathyal depths.

2.2. Seismostratigraphic model

Prior to drilling, the seismostratigraphic model developed for the proposed Expedition 392 drill sites (Figure **F3**) was tentative because only the uppermost part of the sedimentary sequence of the Agulhas Plateau had previously been sampled by scientific drilling at only one location (International Ocean Discovery Program [IODP] Expedition 361 Site U1475 on the southwest Agulhas Plateau) (Hall et al., 2017), and therefore the interpretations for ages of reflectors should be applied with caution. The seismostratigraphic models for the Agulhas Plateau and Transkei Basin sequences were based on analysis of reflection characteristics (e.g., amplitude, frequency content of units, and continuity of reflections) and were tied to the ages of conventional gravity/piston cores (Tucholke and Carpenter, 1977) where possible and to Site U1475 for the post-Miocene sequences (Gruetzner et al., 2019).

For the Agulhas Plateau, Tucholke and Carpenter (1977) and Tucholke et al. (1984) identified four distinct seismic horizons above acoustic basement and constructed a first seismostratigraphic model (see table T2 in Uenzelmann-Neben et al. [2020]). An unconformity above acoustic basement was cored where it crops out high on the western flank of the plateau and was found to be minimally Maastrichtian in age (~72–66 Ma). The underlying reflections terminate against the Upper Cretaceous reflector, thus documenting erosion (Uenzelmann-Neben, 1998, 2002).

A 9 My hiatus across the Paleocene/Eocene boundary in the Agulhas Plateau sedimentary sequence (Tucholke et al., 1984) is interpreted as Reflector LE, which shows strong amplitudes and is mostly conformable to bounding beds (Figure **F4**). Intensified bottom currents (e.g., due to the formation and strengthening of the ACC [Tucholke et al., 1984]) led to the formation of a second regional hiatus between ~33 and 29 Ma (Reflector LO) (Figure **F4**) that is of medium to strong amplitude and represents an unconformity observed on the Agulhas Plateau (Uenzelmann-Neben, 2002). Reflector MM (presumed middle Miocene) is also likely a result of deepwater erosion and redeposition (Tucholke et al., 1984). This reflection shows weaker amplitudes and frequent wedge-outs at the seafloor (Figure **F4**). A regional hiatus of late Miocene–early Pliocene age (~10–

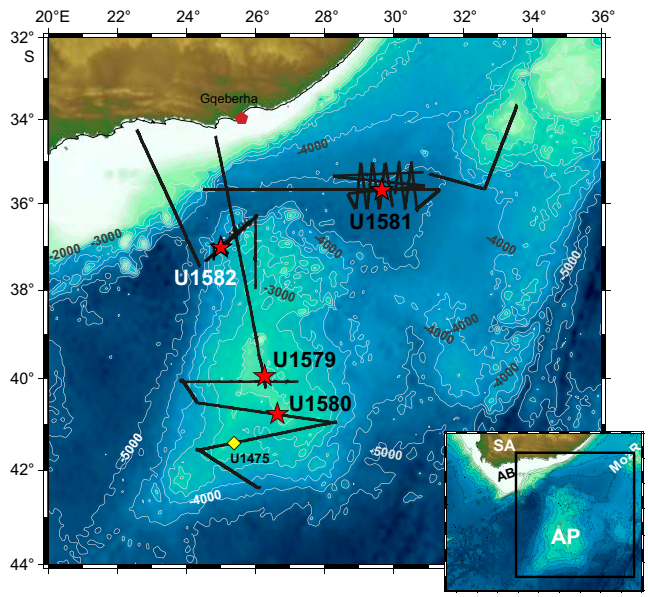

Figure F3. Agulhas Plateau (AP) and Transkei Basin bathymetry (Sandwell and Smith, 1997). Expedition 392 sites (red stars) on seismic lines (black lines) (Uenzelmann-Neben, 1998, 2005, 2014). Yellow diamond = Expedition 361 Site U1475 (Gruetzner et al., 2019; Hall et al., 2017). SA = South Africa, AB = Agulhas Bank, MOZR = Mozambique Ridge.

6 Ma) is attributed to erosion and redeposition of sediments by Circumpolar Deep Water in the ACC (Tucholke et al., 1984) and represented by a strong reflection (Reflector LP), which is often found very close to and thus indistinguishable from the seafloor. Reflector LP is dated to 5.7 Ma (Gruetzner et al., 2019) and interpreted to represent the onset of a period of increased Atlantic Meridional Overturning Circulation. A relatively thin veneer of Pliocene–Pleistocene sediments (~0–50 m) rests on top of the lower Pliocene reflection across most areas of the Agulhas Plateau, forming thicker drift packages only in localized areas. Several reflections in the Pliocene–Pleistocene sequence have been associated with climate-induced changes in circulation (Gruetzner et al., 2019).

In the Transkei Basin, the top of the oceanic crust is imaged as a high-amplitude, partly rugged reflection (Schlüter and Uenzelmann-Neben, 2007). An undisturbed sedimentary sequence overlying basement identified as Subunit 1A is separated from the overlying heavily faulted Subunit 1B by Horizon K-T (presumed Cretaceous/Paleogene [K/Pg] boundary) of medium reflection amplitude (see table T3 in Uenzelmann-Neben et al. [2020]) (Figure **F5**). Sedimentary Unit 1 is topped by Horizon E (presumed late Eocene). In Subunit 1A, a reflection band with higher amplitudes was interpreted to represent black shales (Schlüter and Uenzelmann-Neben, 2008a). The overlying Unit 2 marks a short transition zone and appears as a small but very high–amplitude reflection band with a thickness of ~25 m. The interface between Units 2 and 3 is characterized by Reflector O and is assumed to the Eocene/Oligocene boundary (Figure **F5**). Unit 3 shows signs of increasing energy level and also thickens up to 70 m. The Unit 3/4 boundary is represented by Reflector M, which was hypothesized to be middle Miocene in age. In contrast to Unit 3, overlying Unit 4 thickens up to 130 m, whereas the amplitudes weaken. Units 4 and 5 are separated by the lower Pliocene Reflector P (Figure **F5**). The youngest Unit 5 shows high-amplitude reflections (Schlüter and Uenzelmann-Neben, 2007).

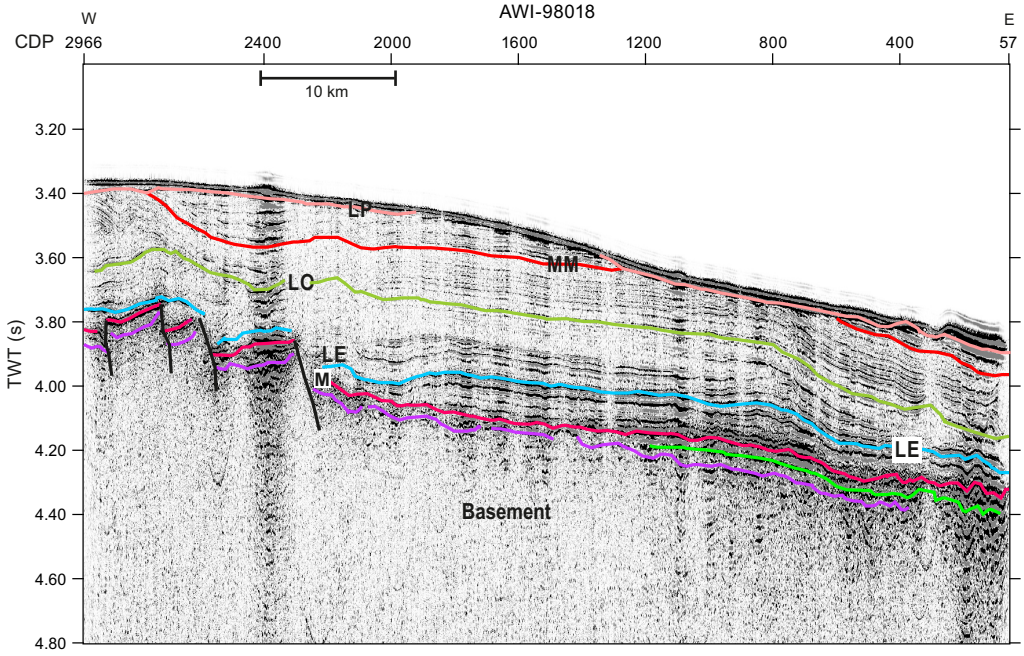

Figure F4. Pre-Expedition 392 seismostratigraphic model developed for the Agulhas Plateau (Allen and Tucholke, 1981; Tucholke and Carpenter, 1977; Uenzelmann-Neben, 2001, 2002). CDP = common depth point, TWT = two-way traveltime, M = Maastrichtian, LE = lower Eocene, LO = lower Oligocene, MM = middle Miocene, LP = lower Pliocene.

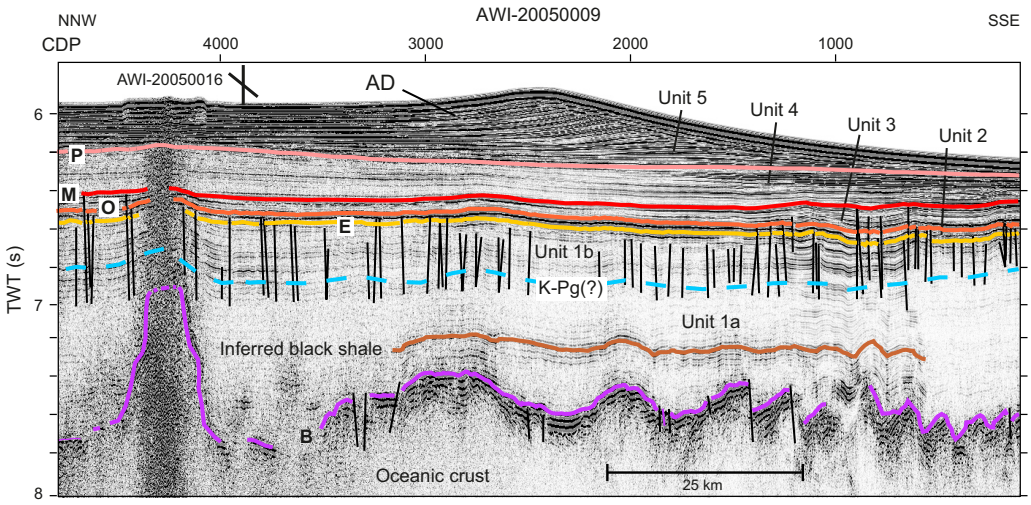

Figure F5. Pre-Expedition 392 seismostratigraphic model developed for the Transkei Basin (Schlüter and Uenzelmann-Neben, 2007). CDP = common depth point, TWT = two-way traveltime, B = top basement, K-Pg(?) = Cretaceous/Paleogene(?) boundary, E = late Eocene, O = Eocene/Oligocene boundary, M = middle Miocene, P = early Pliocene.

3. Scientific objectives

Expedition 392 drilling was aimed at addressing the following scientific questions and objectives (Figure **F3**).

3.1. Objective 1: did Indian Ocean LIPs related to the breakup of Gondwana tap a similar source and show a similar temporal and geochemical evolution to coeval and older Pacific LIPs?

It is hypothesized that the Agulhas Plateau, Northeast Georgia Rise, and Maud Rise initially formed a superplateau similar to the combined Ontong Java–Manihiki–Hikurangi Plateau (Davy et al., 2008; Hoernle et al., 2010; Timm et al., 2011) before being broken up by seafloor spreading in the mid-Cretaceous. Basement rocks recovered on the Agulhas Plateau will test whether the Agulhas Plateau–Northeast Georgia Rise–Maud Rise super-LIP formed at the Bouvet triple junction (Gohl et al., 2007; Parsiegla et al., 2008) (much like the Shatsky Rise in the northwestern Pacific [Sager et al., 1999]) or through interactions between the Bouvet and Marion hotspots with the Southwest Indian Ridge (Georgen et al., 2001). Continuous, 15–20 km long reflections observed in Agulhas Plateau basement structures are similar to lava flow sequences drilled at Shatsky Rise (Tamu Massif) that rapidly accumulated at inferred melt production rates of 0.63–0.84 km^3/y over a time interval of 3–4 My (Geldmacher et al., 2014; Gohl and Uenzelmann-Neben, 2001; Expedition 324 Scientists, 2010; Sager et al., 2013; Uenzelmann-Neben et al., 1999). These rates imply the involvement of a mantle plume.

A fundamental question concerning Cretaceous LIPs is whether they tapped a common magmatic reservoir in the lower mantle, and if so, what is the composition of this reservoir and its homogeneity/heterogeneity (e.g., Jackson and Carlson, 2011; Jackson et al., 2010). Most lavas from Ontong Java Plateau show a homogeneous isotopic composition characterized by the Kwaimbaita/Kroenke component, similar to the composition of proposed common mantle components with intermediate isotopic compositions compared to oceanic intraplate volcanic rocks (e.g., Prevalent Mantle [PREMA], Focal Zone [FOZO], and Common Component) (Hanan et al., 2004; Stracke et al., 2005; Zindler and Hart, 1986). However, the stratigraphically youngest plateau lavas in some areas display a compositionally distinct (Enriched Mantle 1 [EM1]) type; e.g., (Zindler and Hart, 1986) Singgalo composition. On the other hand, recent studies of lavas from the Manihiki Plateau (Timm et al., 2011), Shatsky Rise (Heydolph et al., 2014), and Mozambique Ridge (Jacques et al.,

2019) show considerably more compositional variation, suggesting that even single LIP events tap heterogeneous sources similar to ocean island basalts.

Another important question about LIPs concerns their longevity: do they represent single short-term events occurring over a few million years, or are these volcanic provinces active over longer time periods (e.g., Bryan and Ernst, 2008)? Although the main Tamu Massif of Shatsky Rise formed between ~144 and 143 Ma, magnetic data suggest the three massifs formed over a longer time interval from M20 to M4 (146–127 Ma). The uppermost lava group at the Tamu Massif (Shatsky Rise) yielded an age (133 Ma) ~10 My younger than the main sequence of lavas (144–143 Ma) (Geldmacher et al., 2014), providing evidence for volcanic rejuvenation. These lavas are geochemically identical to the main plateau stage lavas and therefore appear to have tapped the same source. At Ontong Java Plateau, the stratigraphically youngest Singgalo lavas have a distinct trace element and isotopic composition from the main Kwaimbaita/Kroenke lavas (Tejada et al., 2004, 1996, 2002). The uppermost lavas at Manihiki Plateau drilled at Deep Sea Drilling Project (DSDP) Site 317 have a distinct Singgalo-type chemical composition compared to the main low-Ti plateau lavas with Kwaimbaita/Kroenke-type compositions (Hoernle et al., 2010; Timm et al., 2011). Alkalic rejuvenated lavas with distinct (high μ [HIMU]-type) incompatible element and isotopic compositions occur on Ontong Java, Hikurangi, and Manihiki Plateaus (e.g., Hoernle et al., 2010; Timm et al., 2011). Seismic data from the Manihiki Plateau revealed several formation stages: the initial phase forming the nucleus (older than 125 Ma), the extension (125–116 Ma), and the secondary phase (100–65 Ma) (Pietsch and Uenzelmann-Neben, 2015). Seismic and geochemical data from Mozambique Ridge indicate a rapid, partly contemporaneous formation of the four segments and later postsedimentary magmatism (Fischer, 2017; Jacques et al., 2019). These observations pose the question of whether rejuvenated volcanism is a common feature on oceanic plateaus, and if so, what is its origin?

Key questions include the following:

- What are the age, origin, and temporal and geochemical evolution of the uppermost Agulhas Plateau volcanic sequences?
- Do the uppermost Agulhas Plateau lavas show evidence for subaerial volcanism?
- Does the Agulhas Plateau show geochemical affinities and melt production rates similar to other LIPs (e.g., Shatsky, Ontong Java, Manihiki, Hikurangi, and Kerguelen Plateaus), requiring elevated mantle temperatures and/or lower mantle source (high $^3He/^4He$ and solar Ne isotope ratios) and thus the presence of a mantle plume from the lower mantle?
- Is there evidence for late-stage volcanism on the Agulhas Plateau as has been observed at Shatsky Rise and the Ontong Java, Manihiki, and Hikurangi Plateaus? How much younger is it compared to the main plateau stage, and does it show compositional differences in major (alkalic versus tholeiitic) and trace element and isotopic (e.g., more enriched) composition?
- How does Agulhas volcanism correlate with the separation of Africa and Antarctica and the formation of other plateaus in the African–Southern Ocean gateway (e.g., Mozambique Ridge)?

3.2. Objective 2: did sedimentation on the Agulhas Plateau start immediately after crustal emplacement at ~100 Ma under subaerial conditions?

Following the separation of the Falkland Plateau from southern Africa during the breakup of Africa, South America, and Antarctica (Figure **F1**), the onset of free water mass exchange between the Tethys/Indian Ocean and evolving South Atlantic/Southern Ocean emerged. However, the emplacement of LIPs appears to have obstructed the opening of this gateway. König and Jokat (2010) suggested that the Mozambique Ridge formed between 140 and 122 Ma and parts of the Astrid Ridge (Antarctica) were possibly still attached to the Mozambique Ridge (Fischer, 2017; Gohl et al., 2011). It is unclear whether this LIP was submarine or emplaced subaerially, but it likely formed an obstacle for the flow of intermediate and deepwater masses (Fischer and Uenzelmann-Neben, 2018). Another barrier for oceanic circulation was created with the formation of the Agulhas Plateau–Northeast Georgia Rise–Maud Rise LIP between 105 and 95 Ma, after which the Northeast Georgia Rise and Maud Rise detached from the Agulhas Plateau by seafloor

spreading (Figure **F1**) (Gohl and Uenzelmann-Neben, 2001; Gohl et al., 2011; Parsiegla et al., 2008), leading to a widening and deepening of the gateway. Based on crustal thickness and estimated subsidence, Parsiegla et al. (2008) speculated that the central part of the Agulhas Plateau (present water depths are <3000 m) formed subaerially. The Transkei Basin formed between the Mozambique Ridge and Agulhas Plateau–Northeast Georgia Rise–Maud Rise LIPs and the African continent. Plate tectonic reconstructions (König and Jokat, 2010; Parsiegla et al., 2008) suggest that this basin may have been a restricted subbasin until ~80 Ma (Schlüter and Uenzelmann-Neben, 2008a; Uenzelmann-Neben, 2010).

Key questions regarding initial sedimentation on the Agulhas Plateau include the following:

- Under what environmental conditions were sediments deposited shortly after formation of the Agulhas Plateau—subaerial, shallow or deep water, or warm or cool conditions?
- How did emplacement of the plateau influence the climate, oceanic environments, and Earth's biota?
- What can we deduce about water mass changes during early stages of the plateau's evolution? Did emplacement of the Agulhas Plateau LIP interrupt an already incipient circulation?

3.3. Objective 3: did bottom currents associated with deep- and intermediate water masses as well as climatic events leave an imprint in the sedimentary record in the form of seismic reflections and unconformities?

Tucholke and Carpenter (1977) and Tucholke et al. (1984) identified five distinct horizons in their interpretation of Agulhas Plateau seismic reflection data sets, of which they dated the oldest horizon from piston cores and dredge samples as Maastrichtian (see table T2 in Uenzelmann-Neben et al. [2020]). These horizons were subsequently related to regional hiatuses resulting from local sea level highstands, initiation and spreading of the ACC, and activity of Antarctic Bottom Water (Uenzelmann-Neben, 2001, 2002). For the Transkei Basin, Schlüter and Uenzelmann-Neben (2007) presented a seismostratigraphic model tied to the model of Niemi et al. (2000) (see table T3 in Uenzelmann-Neben et al. [2020]) that showed the importance of dating the horizons with respect to possible erosion and the evolution of ocean circulation, which may represent significant climatic episodes (e.g., OAE 3). The Cretaceous sedimentary record of the Transkei Basin represents an archive of the circulation initially restricted by the emplacement and elevation of both the Mozambique Ridge and Agulhas Plateau. Dating of these sedimentary units and unconformities in the Transkei Basin and mapping their regional extent will help us to identify traces of deep- and intermediate water masses, their onset, the intensification and/or weakening of the circulation, and changes to the circulation pathways. This information will provide insight into both long-term and short-lived changes in bottom water circulation through the Late Cretaceous–early Paleogene interval in relation to the tectonic isolation and opening of this gateway.

3.4. Objective 4: what was the paleotemperature history at southern high latitudes across the rise and decline of the Cretaceous supergreenhouse and through the early Paleogene?

Planktonic foraminiferal oxygen isotope records from Falkland Plateau DSDP Site 511 indicate Cretaceous sea-surface temperatures that at times exceeded 30°C (Huber et al., 2002), yet climate simulations require unrealistically high atmospheric pCO_2 levels of 6500–7500 ppm to match these extremely warm subantarctic temperatures (Bice et al., 2003). Although it is unlikely that the mid-Cretaceous experienced such high pCO_2 levels, paleoceanographic and preservational explanations for the low $\delta^{18}O$ values (e.g., diagenesis and low salinity) have been ruled out. Organic geochemical biomarker proxies (notably TEX86) have broadly confirmed both absolute sea-surface temperatures for the South Atlantic as well as the broad-scale cooling trend of the Late Cretaceous (O'Brien et al., 2017; O'Connor et al., 2019), but the precise timing and tempo of cooling following peak Turonian temperatures is debated (e.g., Andò et al., 2013; Friedrich et al., 2012), and this uncertainty compromises parallel efforts to relate changes in the tectonic configuration of gateways and geochemically inferred patterns of circulation to climate evolution. Cretaceous fora-

minifera and inoceramid bivalves from the sequences recovered at Expedition 392 sites should allow construction of oxygen isotope, Mg/Ca, and, depending on organic biomarker preservation, TEX_{86} paleotemperature estimates spanning the mid-Cretaceous supergreenhouse through the early Paleogene, providing a robust temperature history and reducing uncertainties about ocean circulation evolution and paleoenvironmental history of the high southern latitudes.

Recent advances in paleoclimate modeling offer potential avenues for reconciling model–data disparities for Cretaceous temperature and CO_2 estimates through consideration of cloud and biological feedbacks (Kump and Pollard, 2008; Poulsen and Zhou, 2013), emission of non-CO_2 greenhouse gases (Beerling and Royer, 2011), and regional increases in ocean heat transport (Poulsen and Zhou, 2013). Moreover, water isotope–enabled Earth system models are increasingly common, making direct comparisons between proxy data and simulations feasible (e.g., Zhou et al., 2008). Determining whether extreme warm conditions were localized or widespread through the Southern Ocean will provide an important test of possible warming mechanisms.

Specific questions to address include the following:

- What was the thermal history of the Cretaceous, and was this linked to changes in atmospheric CO_2, tectonic evolution, or some other forcing?
- Were surface water temperatures over the Agulhas Plateau cool enough at any time during the Cretaceous and early Paleogene to allow for growth of Antarctic ice sheets?
- Can Earth system models simulate the conditions recorded at Agulhas Plateau during the Cretaceous? What assumptions about CO_2 levels are required to reproduce these conditions?

3.5. Objective 5: how did the progressive opening of the African–Southern Ocean gateway influence Cretaceous to Paleogene circulation?

Significant changes in ocean and atmospheric circulation related to evolving bathymetry in oceanic gateways are one possible driver of global-scale climate change through the Cretaceous and Cenozoic. Many studies have proposed enhanced formation and export of Southern Component Waters starting in the Campanian (e.g., Jung et al., 2013; Murphy and Thomas, 2012; Robinson et al., 2010; Robinson and Vance, 2012; Voigt et al., 2013), promoted by the opening of the South Atlantic and establishment of connections to all major oceanic basins. However, incomplete records that lack robust age control from southern high-latitude areas currently hinder deepwater circulation reconstructions for the Cretaceous and early Paleogene. The source regions for different deepwater masses in evolving southern gateways are also controversial (see **African–Southern Ocean gateway circulation**), and resolving fundamental questions on circulation history requires analyses of samples from various depths in or near gateways across which circulation may have reversed.

Specific questions to address include the following:

- What is the role and impact of the Agulhas Plateau on the evolving communication of deep and intermediate water masses in and between ocean basins? Was there a co-development of Pacific-sourced deepwater circulation in the South Atlantic in the early Paleogene?
- When and how did the opening of Southern Ocean gateways influence Late Cretaceous and early Paleogene regional ocean circulation and heat transport? Did early opening of the African–Southern Ocean gateway and Drake Passage cause invigorated deepwater circulation and a strengthening of surface frontal systems in the eastern South Atlantic?
- Can the onset and evolution of the Agulhas Current be reconstructed in detail? The removal of surficial to Oligocene sedimentary layers suggests that the presently observed circulation has been stable since at least the Neogene (Uenzelmann-Neben and Huhn, 2009). When can we identify the earliest traces of this important water mass exchange between the Indian and the South Atlantic oceans?

3.6. Objective 6: what forcing factors caused Cretaceous OAEs, and what effects did these events have on high-latitude climate, oceanography, and biota?

Despite the nearly four decades since OAEs were discovered, no study has satisfactorily established the primary forcing factors that caused their formation. If increased organic productivity was the dominant cause for OAEs, why are biotic and geochemical indicators of nutrient upwelling generally not found in sediments deposited across those time intervals (Jenkyns, 2010)? On the other hand, if OAEs were caused by sluggish overturning circulation during times of high atmospheric CO_2 (Poulsen and Zhou, 2013) and oxygen-poor water masses in isolated basins (Poulsen et al., 2003), then why is there an offset in the timing of carbon isotope excursions that accompany each of the OAEs relative to peak phases of LIP eruptions and other major volcanic episodes (Jenkyns, 2010), and why are some peak carbon isotope excursions diachronous (Tsikos et al., 2004)? Recovery of complete OAE intervals with well-preserved organic matter and microfossils at the Expedition 392 drill sites will help resolve these controversies. Importantly, new OAE records from the Agulhas Plateau and Transkei Basin will shed light on relative variations in surface productivity and indicate whether there were cooling feedbacks associated with increased organic carbon burial during the OAEs and also whether there were significant changes in bottom circulation prior to, during, and after the OAE intervals. The presence of organic-rich shale with up to ~6% total organic carbon (TOC) from upper Cenomanian–lower Turonian sequences at multiple sites in the Bight Basin (Totterdell et al., 2008) and Mentelle Basin (Chen et al., 2022; Huber et al., 2019; Petrizzo et al., 2021) on the southern/southwestern Australian margin provides evidence that euxinic waters may have been present elsewhere in the southern high latitudes during OAE 2. As noted above, interpretation of the seismic profiles indicates that sediments as old as late Albian may be accessible at relatively shallow burial depths on the Agulhas Plateau, which should allow for preservation of primary geochemical signals across the OAE 1d, OAE 2, and OAE 3 intervals, and a sedimentary section extending down through OAE 3 may be recovered at the Transkei Basin site.

Key questions to address include the following:

- Was there an increase in C_{org} burial during the $\delta^{13}C$ excursion intervals that define Cretaceous OAEs? If so, was the interval of increased C_{org} burial pulsed or continuous?
- How did surface productivity, paleotemperatures, the vertical thermal and $\delta^{13}C$ gradients, and bottom circulation change in the eastern South Atlantic across the OAE intervals?
- Did changes in Agulhas Plateau microfossil assemblages correspond to observed OAE geochemical and sedimentological shifts, and if so, can the cause for those changes be determined?

4. Site summaries

4.1. Site U1579

4.1.1. Background and objectives

Site U1579 is located on the shallowest part of the central Agulhas Plateau (39°57.0725′S, 26°14.1793′E) at 2492 m water depth. The Agulhas Plateau rises up to 2200 m above the surrounding seafloor, with the shallowest central area rising to ~1800 m on average. The central and southern parts of the plateau have a smoother topography, whereas the northern plateau is characterized by a rough topography. The sedimentary column is thicker on the central and southern Agulhas Plateau, whereas the northern plateau shows a very thin or no sedimentary cover. Basement highs characterize the plateau and have been interpreted to represent magmatic edifices. The plateau has been subject to erosion resulting in wedge-out of sequences and the formation of unconformities, which are interpreted to have resulted from oceanic currents flowing across and past the plateau since the Paleogene. The seismic data show that Site U1579 is positioned between two basement highs in a small sediment-filled depression. The seismostratigraphic model developed prior to drilling (see **Background**) provides a framework for interpreting the drill core results. The deepest horizon interpreted is characterized by a rugged

topography and has been interpreted as top of basement (Figure **F6**). Below this horizon, reflections have been observed dipping away from the basement highs. The sedimentary column shows a chaotic layer (ZS) with a strong top reflection immediately above basement. Two further strong seismic horizons can be observed separating layers of potentially Campanian, Maastrichtian, and Paleocene age, which will be confirmed in postcruise analysis. These reflections and the Campanian and Maastrichtian sequences follow the basement topography. The younger sequences show continuous reflections of weaker amplitude. The youngest part of the sedimentary column is affected by strong erosion at the seafloor (Figure **F6**).

Site U1579 was chosen to recover both Cretaceous and Paleogene sedimentary records and basement. Integration of seismic profiles with the drilling results allows for direct dating of the observed Seismic Unconformities M, LE, and LO (purple, blue, and green in Figure **F6**) and interpretation of their causes. Recovery of the sediment/basement interface will provide information on the age of the oldest sediments above the basement, as well as the water depth and environment at the time of deposition. At this site, records spanning the transition from the Cretaceous supergreenhouse and through the Paleogene were drilled. Based on precruise seismostratigraphic interpretations, critical interval of ocean–climate transitions such as Oi1, Paleocene/Eocene Thermal Maximum (PETM), K/Pg boundary, OAEs 2 and 3 were expected to be documented in the sedimentary record. The nature and age of the basement would also be unraveled by drilling at this site.

4.1.2. Operations

Expedition 392 started on 5 February 2022, and following a 1-week quarantine period, the science party boarded on 7 February under the COVID Mitigation Protocols Established for Safe JR Operations (COPE). The majority of incoming freight was loaded by the previous crew, and on 8 February the offgoing core and surface freight was loaded into two reefers. Fuel bunkering was completed via barge, and a load of fresh and frozen produce was brought aboard. The final installation, testing, and commissioning of the new 50 kVA uninterruptible power supply (UPS) for the *JOIDES Resolution* Science Operator (JRSO) network was done on 8 and 9 February, requiring temporary blackouts of shipboard IT services. COVID-19 rapid antigen testing was conducted for all shipboard personnel on 8 February, and PCR testing was conducted on 9 February.

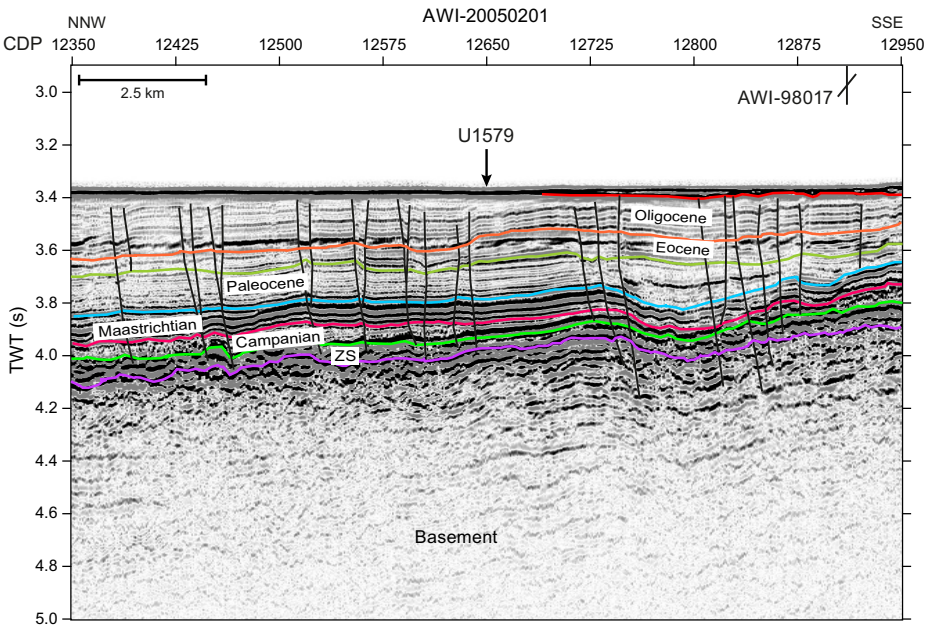

Figure F6. Seismic Line AWI-20050201 showing the location of Site U1579. Preliminary interpretation of seismic units according to the chronostratigraphic model is shown. The marked green reflection corresponds in structure to Reflector M of the pre-Expedition 392 seismostratigraphic model (Figure F4), the magenta reflection to Reflector LE, and the blue reflection to Reflector LO. CDP = common depth point, TWT = two-way traveltime, ZS = zeolitic silicified sediments.

The vessel departed Cape Town, South Africa, from Repair Quay 3 on 10 February at 1024 h (all times are local ship time [UTC + 2 h]). The pilot disembarked at 1045 h, beginning the sea voyage to Site U1579. Within minutes of the vessel reaching full throttle, the newly commissioned 50 kVA UPS began rejecting the ship's power and running off the batteries, and the vessel was therefore throttled back to half speed at 1116 h. It was decided to take the UPS offline, after which the vessel was returned to full throttle at 1448 h, and the sea voyage continued at full speed. The 557 nmi transit was completed in 52.1 h at an average speed of 10.8 kt. We arrived at Site U1579 at 1430 h on 12 February.

Site U1579 hole locations, water depths, and the number of cores recovered are listed in Table **T1**. The first core of Expedition 392 was taken in Hole U1579A at 0500 h on 13 February in 2498.32 m of water. We used the advanced piston corer (APC) system to take Cores 1H–8H, and the last material was recovered at 74.78 m core depth below seafloor, Method A (CSF-A). The advanced piston corer temperature (APCT-3) tool was run on Cores 4H and 7H. After firing Core 9H from 74.6 m CSF-A, the core barrel became stuck. The core barrel was retrieved; however, all that was recovered was a sheared overshot and the sinker bars, and the decision was made to abandon the hole. A total of 9 cores were taken in Hole U1579A over an 84.1 m interval (recovery = 87%). Total time on Hole U1579A was 33.12 h (1.38 days).

Hole U1579B was spudded at 0910 h on 14 February. We used the APC system to take Cores 1H–6H (0–57.0 m CSF-A) and switched to half-length APC (HLAPC) coring for Cores 7F–24F (57.0–

Table T1. Hole summary, Expedition 392. DSF = drilling depth below seafloor. **Download table in CSV format.**

Hole	Latitude	Longitude	Water depth (m)	Penetration DSF (m)	Interval cored (m)	Core recovered (m)	Recovery (%)	Drilled interval (m)	Drilled interval (*N*)	Total cores (*N*)	APC cores (*N*)	HLAPC cores (*N*)	XCB cores (*N*)	RCB cores (*N*)
U1579A	39°57.0659′S	26°14.1729′E	2498.32	84.1	84.1	73.5	87.4		0	9	9	0	0	0
U1579B	39°57.0565′S	26°14.1729′E	2492.92	167.2	167.2	167.1	99.9		0	27	6	18	3	0
U1579C	39°57.0588′S	26°14.1785′E	2492.92	186.9	93.4	74.3	79.5	93.5	7	18	0	15	3	0
U1579D	39°57.0725′S	26°14.1793′E	2492.92	727.2	597.2	440.8	73.8	130.0	1	64	0	0	0	64
		Site U1579 totals:		1165.4	941.9	755.7	85.2	223.5	8	118	15	33	6	64
U1580A	40°47.1535′S	26°36.4137′E	2560.33	533.9	533.9	351.0	65.8		0	68	0	0	0	68
U1580B	40°47.1542′S	26°36.4282′E	2560.33	77.8	37.8	23.8	62.9	40.0	1	4	0	0	0	4
		Site U1580 totals:		611.7	571.7	374.8	64.3	40.0	1	72	0	0	0	72
U1581A	35°40.8654′S	29°39.0055′E	4591.35	300.5	300.5	273.2	90.9		0	40	28	9	3	0
U1581B	35°40.8660′S	29°39.0192′E	4591.35	997.1	708.1	539.5	76.2	289.0	1	73	0	0	0	73
		Site U1581 totals:		1297.6	1008.6	812.7	83.6	289.0	1	113	28	9	3	73
U1582A	37°1.5002′S	24°59.7168′E	3429.36	48.0	48.0	18.5	38.5		0	7	0	0	0	7
U1582B	37°1.5003′S	24°59.7114′E	3429.36	55.6	19.3	10.1	52.2	36.3	1	4	0	0	0	4
		Site U1582 totals:		103.6	67.3	28.6	45.4	36.3	1	11	0	0	0	11
		Expedition 392 totals:		3178.3	2589.5	1971.8	76.1	588.8	11	314	43	42	9	220

Hole	Date started (2022)	Time started (h UTC)	Date finished (2019)	Time finished (h UTC)	Time on hole (h)	Time on hole (days)
U1579A	12 Feb	1300	13 Feb	2210	33.12	1.38
U1579B	13 Feb	2210	15 Feb	1445	40.56	1.69
U1579C	15 Feb	1445	17 Feb	0900	42.24	1.76
U1579D	17 Feb	0900	25 Feb	0530	188.4	7.85
				Site U1579 totals:	304.32	12.68
U1580A	25 Feb	1130	7 Mar	0500	233.52	9.73
U1580B	7 Mar	0500	8 Mar	1230	31.44	1.31
				Site U1580 totals:	264.96	11.04
U1581A	9 Mar	2200	14 Mar	0630	104.4	4.35
U1581B	16 Mar	1015	26 Mar	1315	243.12	10.13
				Site U1581 totals:	347.52	14.48
U1582A	27 Mar	1245	29 Mar	0300	38.16	1.59
U1582B	1 Apr	1045	3 Apr	1045	48	2
				Site U1582 totals:	86.16	3.59
				Expedition 392 totals:	1002.96	41.79

141.6 m CSF-A). The extended core barrel (XCB) system was used to take the final cores (25X–27X). A total of 27 cores were taken in Hole U1579B over a 167.08 m interval (recovery = 99%). The rate of penetration (ROP) for XCB cores (3) averaged 11 m/h. Total time on Hole U1579B was 40.56 h (1.69 days).

Hole U1579C was spudded at 1720 h on 15 February. The hole was drilled down with a center bit to 56.5 m. We used the HLAPC system to take Cores 2F–21F (56.5–130.5 m CSF-A), with five small (0.5–1.5 m) advances without recovery for stratigraphic correlation. We then drilled down an additional 31.5 m and used the XCB system to take Cores 23X–25X, although Core 23X did not recover any material. Heave made it difficult to keep the bit on bottom, and the decision was made to terminate coring in Hole U1579C following the retrieval of Core 25X at the final depth of 186.9 m CSF-A. A total of 18 cores were taken in Hole U1579C over a 93.4 m interval (recovery = 80%). The ROP for XCB cores (3) averaged 9.6 m/h. Total time on Hole U1579C was 42.24 h (1.76 days).

Hole U1579D was spudded at 2124 h on 17 February and drilled down to 130 m CSF-A. We used the rotary core barrel (RCB) system to take Cores 2R–65R (130.0–727.2 m CSF-A). On 24 February, the bit was released in the bottom of the hole at 0310 h and the hole was displaced with heavy mud in preparation for logging. The 48 m long quadruple combination (quad combo) tool string consisted of the Hostile Environment Litho-Density Sonde (HLDS), Dipole Shear Sonic Imager (DSI), Hostile Environment Natural Gamma Ray Sonde (HNGS), High-Resolution Laterolog Array (HRLA), and Magnetic Susceptibility Sonde (MSS). The downlog was paused to conduct a high-resolution uplog from 450 to 250 m wireline log matched depth below seafloor (WMSF). After resuming the downlog, the tool tagged bottom at 727.7 m WMSF, and an uplog was done. Pipe was tripped back to the rig floor, and Hole U1579D ended at 0735 h. A total of 64 cores were taken in Hole U1579D over a 597.2 m interval (recovery = 73.8%). The ROP for RCB coring averaged just under 20 m/h in the sediment to 2.0 m/h in basalt (average = 8.2 m/h). Total time on Hole U1579D was 188.4 h (7.85 days).

4.1.3. Principal results

4.1.3.1. Lithostratigraphy

A ~727 m thick sequence of sediments and basalt was recovered at Site U1579 (Figure **F7**; see Figures **F2** and **F3**, both in the Site U1579 chapter [Bohaty et al., 2023a]). The main sedimentary succession down to ~697 m CSF-A is divided into Lithostratigraphic Units I–III, and Lithostratigraphic Unit II is further divided into Lithostratigraphic Subunits IIa–IIc (see Table **T2** in the Site U1579 chapter [Bohaty et al., 2023a]). Lithostratigraphic Units I–II represent a ~634 m thick sequence of calcareous sediments of Pleistocene–Santonian age that overlie a ~62 m thick sequence of zeolitic siliciclastic sediments (Lithostratigraphic Unit III). Below Lithostratigraphic Unit III, a ~24 m interval of basalt designated as Lithostratigraphic Unit IV overlies another ~5 m of zeolitic siliciclastic sediments (Lithostratigraphic Unit V) and ~2 m of basalt (Lithostratigraphic Unit VI).

Lithostratigraphic Unit I (Hole U1579A = 0–1.31 m CSF-A; Hole U1579B = 0–6.13 m CSF-A) consists of light gray foraminiferal ooze with average carbonate concentrations of ~90 wt% $CaCO_3$ (see Figure **F2** in the Site U1579 chapter [Bohaty et al., 2023a]). Lithostratigraphic Unit I is differentiated from the underlying white nannofossil ooze of Lithostratigraphic Unit II on the basis of a greater abundance of foraminifera and a darker light gray color. The light gray color reflects a greater abundance of sand-sized glauconite grains, disseminated pyrite, and clay. Lithostratigraphic Unit II consists of ~630 m of Miocene–Campanian carbonate ooze and chalk. The primary sedimentary components of this unit are calcareous nannofossils and recrystallized calcite with varying abundance of foraminifera and clay (see Figure **F3** in the Site U1579 chapter [Bohaty et al., 2023a]). Lithostratigraphic Unit II is divided into Lithostratigraphic Subunits IIa–IIc on the basis of lithification (ooze versus chalk), color, and the occurrence of thin silicified horizons. Lithostratigraphic Unit III (Hole U1579D = 634.72–697.00 m CSF-A) consists of ~60 m of greenish gray well-lithified zeolitic siliciclastic sediments (sandstones, siltstones, and claystones) with glauconite. Rare carbonate bioclasts and foraminifera suggest marine deposition. The variety of processes influencing the composition of Lithostratigraphic Unit III (volcanism, siliciclastic sedi-

mentation, and alteration) suggests a complex history of sedimentation and postdepositional diagenesis.

Lithostratigraphic Unit V (Hole U1579D = 720.77–725.47 m CSF-A) is a ~5 m interval of greenish gray sediments that were recovered between basalt units (Lithostratigraphic Units IV and VI; see below). Lithostratigraphic Unit V is of a similar lithologic character to Lithostratigraphic Unit III but is physically separated from Lithostratigraphic Unit III by basalt (Lithostratigraphic Unit IV). Like Lithostratigraphic Unit III, Lithostratigraphic Unit V consists of well-lithified greenish gray zeolitic siltstone and sandstone sediments with glauconite. The contact between the sediments of Lithostratigraphic Unit V and the underlying basalt of Lithostratigraphic Unit VI at 725.47 m CSF-A provides important clues to the emplacement of the basalt. Lithostratigraphic Unit V is ~50 cm thick and gradually lightens downcore from greenish gray to light greenish gray, and individual grains and sedimentary structures become less distinct. This change in sedimentary character is

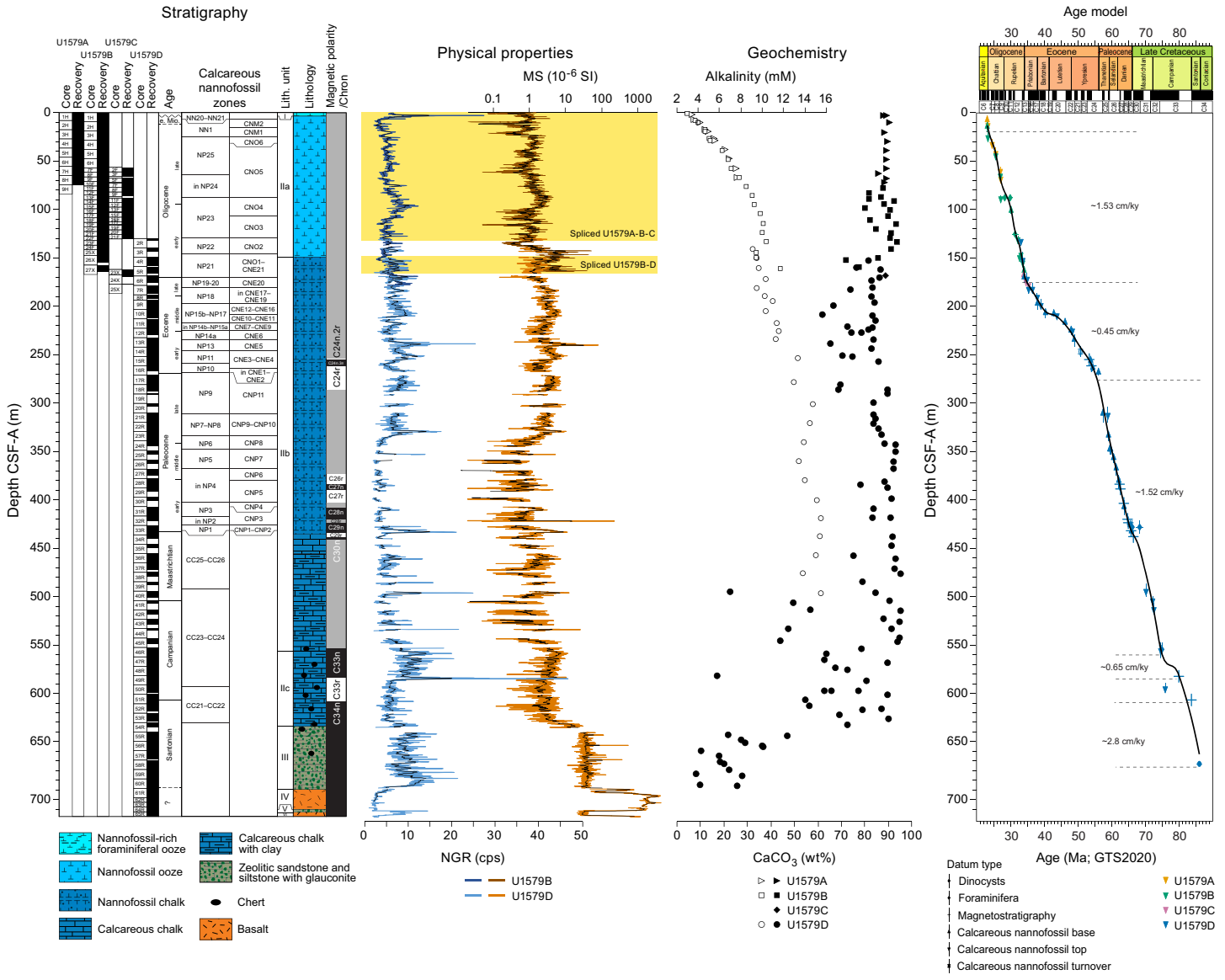

Figure F7. Stratigraphic summary, Site U1579. Calcareous nannofossil zones: NP following Martini (1971); CC following Sissingh (1977); CN following Agnini et al. (2014). Physical properties of NGR: dark blue = U1579B, light blue = U1579D, black = 15-point moving average, cps = counts per second. WRMSL MS: brown = U1579B, orange = U1579D, black = 25-point moving average. Alkalinity measurements (open symbols = Holes U1579A, U1579B, and U1579D) are from pore waters. Carbonate content (black closed symbols = all holes) is from bulk sediments. Age model is based on biostratigraphy and magnetostratigraphy, with estimated sedimentation rates. Yellow rectangles = stratigraphic intervals for which a splice is constructed.

interpreted as evidence for contact metamorphism due to heating following intrusion of Lithostratigraphic Unit VI.

4.1.3.2. Igneous petrology

Igneous rocks were encountered at 697.00 m CSF-A in Hole U1579D below sedimentary Lithostratigraphic Unit III (Figure **F7**; see Figure **F12** in the Site U1579 chapter [Bohaty et al., 2023a]). A 23.77 m massive interval of igneous rock (Lithostratigraphic Unit IV) was cored between 697.0 and 720.77 m CSF-A, below which a 4.57 m sedimentary sequence (Lithostratigraphic Unit V) was encountered (720.77–725.47 m CSF-A). This sequence is underlain by another massive igneous unit (Lithostratigraphic Unit VI; 725.47–727.29 m CSF-A), of which 1.82 m was cored before drilling in Hole U1579D was terminated at a final depth of 727.29 m CSF-A. Lithostratigraphic Unit IV (Igneous Unit 1; 697.00–720.77 m CSF-A) is composed of plagioclase-clinopyroxene phyric basalt. The unit grades downsection toward less vesicular and more coarse-grained textures, and the central portion of the unit is well crystallized and medium grained. From the central part of the unit downsection, the groundmass grain size decreases to fine grained and eventually aphanitic at its lower contact. No abrupt or significant lithologic changes (e.g., different mineralogy or multiple cooling units) could be recognized in the 23.77 m igneous succession of Lithostratigraphic Unit IV (Igneous Unit 1) (see Figure **F12** in the Site U1579 chapter [Bohaty et al., 2023a]). Lithostratigraphic Unit VI (Igneous Unit 2; 725.47–727.285 m CSF-A) is composed of nearly aphyric basalt, is moderately vesicular (all vesicles are filled with alteration minerals), and shows a fine-grained groundmass.

The igneous Lithostratigraphic Units IV and VI in Hole U1579D are tentatively interpreted to be sills based on systematic lithologic variations toward their upper and lower margins and the characteristics of the sediments at the contact zones. Both units show relatively wide (>20 cm) chilled (and altered) zones without significant brecciation. Lithostratigraphic Unit IV, which was completely cored, also shows a spatial increase in groundmass grain size toward its center. Accordingly, both units show more characteristics of sills than lava flows. Importantly, the sediments at the contact zones above both the upper and lower igneous bodies show alteration reactions such as brick red colored streaks characteristic of thermal baking as well as bleaching and recrystallization, supporting an igneous sill interpretation (see Figure **F14** in the Site U1579 chapter [Bohaty et al., 2023a]).

4.1.3.3. Micropaleontology

The sedimentary succession recovered at Site U1579 contains calcareous nannofossils, foraminifera, siliceous microfossils, and palynomorphs in varying abundance and preservation (see Figure **F15** in the Site U1579 chapter [Bohaty et al., 2023a]). Calcareous nannofossils are generally abundant and moderately to well preserved above 635 m CSF-A (Lithostratigraphic Units I and II) and provide the primary means of biostratigraphic age control for the calcareous sediments recovered at Site U1579. Planktonic foraminifera are also generally abundant and moderately to well preserved above 635 m CSF-A and also provide age control for the calcareous sediments. Benthic foraminifera, however, are present in significantly fewer numbers. Radiolarians, together with sparse silicoflagellates and diatoms, are present only in the EOT interval. Palynomorphs, including dinoflagellate cysts (dinocysts), pollen, and spores, are found in discrete organic-rich layers below 635 m CSF-A and provide important age control in the lower part of the sedimentary succession (Lithostratigraphic Unit III), which is nearly devoid of carbonate and siliceous microfossils.

4.1.3.4. Paleomagnetism

Paleomagnetic measurements were performed on all archive section halves from Site U1579, in addition to 131 discrete samples. The primary purpose of these measurements was to determine magnetic polarity stratigraphy. However, additional rock magnetic experiments (anisotropy of magnetic susceptibility [AMS] and isothermal remanent magnetization [IRM] acquisition) were performed to further inform the reliability of magnetic signals, magnetic fabric, and environmental/postdepositional processes.

In Lithostratigraphic Unit I and Lithostratigraphic Subunit IIa (foraminiferal and nannofossil oozes; 0 to ~144 m CSF-A), a reliable magnetostratigraphy was not determined because of the low magnetization intensities of the samples. In Lithostratigraphic Subunits IIb and IIc (nannofossil

chalks; ~144–635 m CSF-A), the determination of a complete magnetostratigraphy was also not possible, again because of the low magnetization of the samples. Using biostratigraphic constraints, however, in some regions of Lithostratigraphic Subunits IIb and IIc it is possible to determine distinct polarities and correlate these to chrons within the geomagnetic polarity timescale (GPTS) from the Geologic Time Scale 2020 (GTS2020) (Gradstein et al., 2020; Ogg, 2020) (see Figure **F26** and Table **T14** in the Site U1579 chapter [Bohaty et al., 2023a]). In Lithostratigraphic Unit III (zeolitic sandstone, siltstone, and claystone with glauconite; ~635–697 m CSF-A), magnetization intensity increases and polarity determination and chron correlation was possible. The identified chrons at Site U1579 include Chrons C24n.3n, C27n, C27r, C28n, C28r, C29n, C29r, C33r, and C34n. All of the zeolitic sandstone to siltstone with glauconite and the basalt units have normal polarity that are assigned to Chron C34n (Figure **F7**). Further postcruise analysis of discrete samples in shore-based laboratories may allow for identification of additional polarity zones and overall refinement of the polarity stratigraphy for Site U1579.

4.1.3.5. Stratigraphic correlation

The physical properties records of Holes U1579A–U1579D were compared and correlated, where possible, to establish a common depth scale. Tie points were identified using natural gamma radiation (NGR), magnetic susceptibility (MS) from Whole-Round Multisensor Logger (WRMSL), color reflectance data, high-resolution digital core images, and red-green-blue (RGB) color space data extracted from the digital core images. A composite record was spliced for the upper 147 m core composite depth below seafloor (CCSF) of the recovered stratigraphic succession (Figure **F7**). Small recovery gaps in the composite record exist at 66.42–67.02 and 94.00–94.13 m CCSF. From 147.49 to 164.32 m CCSF, a complete composite record could not be established due to a lack of overlapping cores from parallel holes. From 164.32 to 182.52 m CCSF, a composite record was made stitching cores together from Holes U1579B and U1579D. Below 182.52 m CCSF, cores from Hole U1579D do not have parallel drilled sections.

Recognition of matching patterns in NGR records from cores and total spectral gamma ray (HSGR) wireline logging data from the HNGS in Hole U1579D permitted translation of core depth scales from the CSF-A scale to the WMSF scale. The correlation between NGR signals in the retrieved sediment core and HNGS downhole logging data sets is excellent, allowing the segments of recovered core intervals to be tightly correlated to the continuous wireline logging data.

4.1.3.6. Chronostratigraphy

Calcareous nannofossils, planktonic and benthic foraminifera, dinocysts, and magnetostratigraphy provide age control for the Santonian–lower Miocene sediments recovered at Site U1579 (Figure **F7**; see Figure **F37** in the Site U1579 chapter [Bohaty et al., 2023a]). Very few age constraints were identified in shipboard work for the lowermost part of the sedimentary sequence recovered at Site U1579 (below ~607 m CSF-A). However, an early Santonian age (86.8–85.2 Ma) is indicated based on the dinocyst assemblage, which is consistent with the interpretation of the persistent normal polarity in this interval to represent Magnetochron C34n (the Cretaceous Normal Superchron). Calcareous nannofossil, planktonic foraminiferal, and benthic foraminiferal biostratigraphy and magnetostratigraphy further constrain the age of the sedimentary sequence between 607.59 and 505 m CSF-A to the Campanian stage of the Late Cretaceous (83.7–72.2 Ma), which is overlain by Maastrichtian sediment (Figure **F7**). The K/Pg boundary was recovered in Core 392-U1579D-33R (66.04 Ma; 433.255 m CSF-A), with the base of the Paleocene tentatively identified at the base of a thin greenish gray clay. This placement was confirmed by benthic foraminiferal biostratigraphy, in addition to the top of Cretaceous calcareous nannoflora, which demarcates the end of the Cretaceous. The identification of the top of Chron C30n at ~438.46 m CSF-A supports this interpretation. The position of the K/Pg boundary at Site U1579 will be confirmed in postcruise research with more refined biostratigraphic analysis and the addition of chemostratigraphic analysis (e.g., iridium stratigraphy and bulk carbonate carbon isotope stratigraphy).

Calcareous nannofossil biostratigraphy provides the primary means of age control for Paleocene–lower Miocene sediments recovered in the upper part of Site U1579, with support from planktonic foraminiferal biostratigraphy and magnetostratigraphy (see Figure **F37** in the Site U1579 chapter [Bohaty et al., 2023a]). Core 392-U1579D-16R (267.14 m CSF-A) represents the basal Eocene (~56.0 Ma). Between the K/Pg boundary and basal Eocene, 14 nannofossil biohorizons and six

paleomagnetic reversals provide good age control for the Paleocene sediments (Figure **F7**). The Eocene/Oligocene boundary (33.9 Ma) is identified between ~175 and ~168 m CSF-A. Between the basal Eocene and Eocene/Oligocene boundary, 18 nannofossil biohorizons and 2 paleomagnetic reversals provide good age control for the Eocene section of Site U1579 (Figure **F7**; see Figure **F37** in the Site U1579 chapter [Bohaty et al., 2023a]).

Near the top of the recovered sedimentary section at Site U1579, a disconformity separates a thin veneer (~1–6 m thick) of Pleistocene sediments from the underlying sediments, which are dated to approximately the Oligocene/Miocene boundary (23.04 Ma) based on calcareous nannofossil biostratigraphy (Figure **F7**). Thirteen calcareous nannofossil and three foraminiferal datums provide good age control for the Oligocene sediments recovered at Site U1579 (~168 to 1–6 m CSF-A) (see Figure **F37** in the Site U1579 chapter [Bohaty et al., 2023a]).

4.1.3.7. Geochemistry

The geochemistry program at Site U1579 was designed to characterize the composition of bulk sediment and interstitial water (IW) and report on the presence and abundance of volatile hydrocarbons for routine safety monitoring. In total, 73 headspace samples were analyzed for routine safety monitoring. Methane concentrations are overall very low throughout Site U1579, generally ranging 0–12.4 ppmv, with the highest methane concentration of 21.2 ppmv observed at 386.92 m CSF-A (see Figure **F38** in the Site U1579 chapter [Bohaty et al., 2023a]). Higher hydrocarbons are not detected, except at 420.94 m CSF-A, where traces of iso-pentane (0.14 ppmv) are present.

IW samples were analyzed for Holes U1579A–U1579D to 497.08 m CSF-A, below which IW was not extractable. IW alkalinity, pH, and major anion and cation concentrations all show distinctive downhole trends. From the seafloor to 496.98 m CSF-A, alkalinity values increase from 2.9 to 15.4 mM and pH values decrease from ~7.7 to ~7.0 (Figure **F7**; see Figure **F39** in the Site U1579 chapter [Bohaty et al., 2023a]). Sulfate decreases from ~29 mM immediately below the seafloor to 22.7 mM at ~280 m CSF-A, and then remains relatively constant downhole to ~497 m CSF-A (see Figure **F40** in the Site U1579 chapter [Bohaty et al., 2023a]). Chloride and sodium both increase downhole above their seawater values (557 and 481 mM, respectively) to roughly 610 and 510 mM, respectively, at ~497 m CSF-A (see Figure **F40** in the Site U1579 chapter [Bohaty et al., 2023a]). Calcium increases downhole from 10.7 mM immediately below the seafloor to 27.5 mM at ~497 m CSF-A, and magnesium decreases downhole from 51.6 to 46.0 mM at ~279 m CSF-A before increasing to ~49 mM at the base of the record (see Figure **F40** in the Site U1579 chapter [Bohaty et al., 2023a]).

Sediment samples were analyzed for carbon and nitrogen concentration in Holes U1579A–U1579D to 695.68 m CSF-A. In the upper ~450 m of the sedimentary sequences, carbonate concentration is high (~60–95 wt%) (Figure **F7**; see Figure **F42** in the Site U1579 chapter [Bohaty et al., 2023a]), which is consistent with the deposition of largely pelagic nannofossil ooze and chalks. Significant variability in carbonate content is observed between ~150 and 300 m CSF-A, and generally lower carbonate concentrations are found below ~450 m CSF-A. Below ~630 m CSF-A (Lithostratigraphic Unit III), carbonate content decreases to an average of ~24 wt%; the carbonate in this lower interval may include other carbonate minerals such as siderite and dolomite. The average TOC content of Site U1579 sediment samples is 0.3 ± 0.2 wt%, with minimum and maximum concentrations of 0 and 1.0 wt%, respectively. The low organic carbon content reflects the calcareous ooze and chalk character of Lithostratigraphic Units I and II (Figure **F7**).

Three samples from the Igneous Units 1 and 2 were also analyzed for major and selected trace elements using inductively coupled plasma–atomic emission spectrometry (ICP-AES). Based on classic discrimination diagrams for igneous rocks, all samples classify as tholeiitic basalts (see Figure **F44** in the Site U1579 chapter [Bohaty et al., 2023a]).

4.1.3.8. Physical properties

Physical properties of sediments and igneous rocks recovered at Site U1579 were measured on whole-round core sections, split half core sections, and discrete samples from each hole at the site to a total depth of 727.3 m CSF-A. In the upper 182 m of the site, the holes overlap stratigraphically, and physical properties data were used to construct a composite splice (see **Stratigraphic correlation**).

NGR and MS vary between the lithostratigraphic units (Figure **F7**). Lithostratigraphic Unit I is characterized by relatively high NGR and low MS values, and Lithostratigraphic Subunit IIa (Hole U1579B = 6.13–147.10 m CSF-A) has lower average values for both parameters. Greater variability is observed in Lithostratigraphic Subunits IIb and IIc (Hole U1579D = 149.40–634.72 m CSF-A). In the basalts of Lithostratigraphic Units IV (697.00–720.77 m CSF-A) and VI (725.47–727.29 m CSF-A), NGR values are lower and MS shows the highest values.

Moisture and density (MAD) analyses were performed on 139 discrete samples. Bulk density increases downhole following a general trend of porosity reduction (see Figure **F48** in the Site U1579 chapter [Bohaty et al., 2023a]). Density values are higher in Lithostratigraphic Subunit IIc (556.31–634.72 m CSF-A) but low in Lithostratigraphic Unit III (634.72–697.00 m CSF-A). Contact *P*-wave velocities were measured with the *P*-wave caliper (PWC) system from working-half sections (1–2 per core; total = 163) and from three discrete cubic samples (nine measurements) (see Figure **F50** in the Site U1579 chapter [Bohaty et al., 2023a]). In Lithostratigraphic Unit I and Lithostratigraphic Subunit IIa (Hole U1579B = 0–147.10 m CSF-A), *P*-wave velocities vary in a narrow range of 1560–1600 m/s. Higher *P*-wave velocities of ~2000–2150 m/s characterize the nannofossil chalk of Lithostratigraphic Subunit IIb to ~500 m CSF-A. In the chert-rich nannofossil chalk of Lithostratigraphic Subunit IIc, velocity significantly increases to 2500–3500 m/s between 556 and 635 m CSF-A. Average *P*-wave velocities in the underlying altered zeolitic siltstones and sandstones (Lithostratigraphic Units III and V) and basalts (Lithostratigraphic Units IV and VI) are 2500–3000 m/s and 4500–5600 m/s, respectively.

Thermal conductivity measured on soft-sediment whole-round sections show a general increase downhole (see Figure **F48** in the Site U1579 chapter [Bohaty et al., 2023a]). Values are higher in the basalts of Lithostratigraphic Unit IV (697.00–720.77 m CSF-A), and lower values in this range reflect more vesicular textures and interbedded sediments.

4.1.3.9. Downhole measurements

Two high-quality equilibrium borehole temperature measurements were recorded with the APCT-3 while coring Hole U1579A. Additionally, Hole U1579D was logged using the quad combo tool string, which consisted of the MSS, HNGS, HRLA, DSI, and HLDS (see Figure **F51** in the Site U1579 chapter [Bohaty et al., 2023a]). A high-resolution pass between 450 and 250 m WMSF covering the condensed Eocene–Oligocene interval was followed by a normal resolution pass over the full depth of Hole U1579D. HSGR logging data vary with lithology, and the highest values are in the zeolitic silicified silt- and sandstones. Lithostratigraphic Unit IV basalts (below 697 m WMSF) show the lowest HSGR values. Increased resistivity in HRLA logs corresponds to zones of chalk beds with claystone and chert in Lithostratigraphic Subunit IIc (~556–635 m WMSF; see **Lithostratigraphy**). The highest resistivity values (100–300 Ωm) were recorded in Lithostratigraphic Unit IV basalts (see Figure **F51** in the Site U1579 chapter [Bohaty et al., 2023a]). The density logs from the HLDS generally follow the *P*-wave velocity trends from the DSI. There is a distinct offset between the *P*-wave velocities measured on the cores and downhole. In Lithostratigraphic Subunit IIb (200–556 m WMSF), the *P*-wave velocity is 2000–2500 m/s, which is about 300 m/s higher than measured in the laboratory.

4.2. Site U1580

4.2.1. Background and objectives

Site U1580 is located on the southern central Agulhas Plateau (40°47.1535′S, 26°36.4137′E) at 2560 m water depth. The site lies about 100 km southeast of Site U1579. Bathymetric data show Site U1580 to be located on the flank of a bathymetric high that is underlain by a number of basement highs, as revealed by seismic data. A rugged topography characterizes the top of the interpreted basement. Below this horizon, reflections have been observed dipping away from the basement highs in all directions. The basement highs have thus been interpreted as extrusion centers (Figure **F8**). The seismic data show a chaotic layer topped by Reflector M with a strong reflection amplitude. Another strong seismic horizon, Reflector LE, can be observed. Both Reflectors M and LE follow the basement topography. The sequence above Reflector LE shows parallel to subparallel continuous reflections of middle to strong amplitude. The youngest part of this sequence is affected by erosion at the seafloor (Figure **F8**).

Site U1580 was chosen to recover both Cretaceous and Paleogene sedimentary records and basement samples. This site was especially dedicated to recover an extended record of basement material to unravel the nature of the basement and provide information on its formation age. Potential late-stage magmatism and its effect on sedimentary sequences and the environment are additional objectives. Integration of seismic profiles with the drilling results will allow direct dating of the observed Seismic Unconformities M and LE and interpreting their causes, and recovery of the sediment/basement interface will provide information on the age of the oldest sediments above the basement as well as the water depth and environment at the time of deposition. At this site, a sediment sequence from the mid-Cretaceous to mid-Paleogene was expected to be drilled, spanning the long-term climate transition from the Cretaceous greenhouse to the mid-Paleogene icehouse. Critical intervals of ocean–climate transitions such as Oi1 glaciation, the PETM, the K/Pg boundary, and OAEs 2 and 3 were expected to be documented in the sedimentary record. The nature and age of the basement would also be unraveled by drilling at this site.

4.2.2. Operations

The vessel arrived at Site U1580 at 1306 h on 25 February 2022. The thrusters were lowered, and the vessel switched from cruise mode to dynamic positioning (DP) mode at 1326 h. Hole U1580A was spudded using the RCB system at 2015 h, with Core 1R recovering 6.82 m. For the next several days, RCB coring continued through Core 42R, advancing from 9.7 to 407.4 m and recovering 250.38 m (63%). Site U1580 hole locations, water depths, and the number of cores recovered are listed in Table **T1**.

At ~1700 h on 1 March, the ROP on Core 392-U1580A-43R slowed to almost zero and no noticeable progress was being made. Following an additional short advance with no recovery in Core 44R, the bit deplugger (a core barrel with a pointed, metal tip) was dropped twice in an attempt to clear any material blocking the bit. Core 45R then advanced 3.2 m and recovered 3.25 m. It was determined from recovered pieces that a chert layer of loosened rock was slowing the ROP and preventing recovery.

The sediment/basalt contact was difficult to determine based on coring parameters, likely due to multiple chert/silicified horizons in the sediments immediately overlying the basalts that resulted in very low overall ROP. Although core recovery was low, pieces of basalt were recovered in Cores

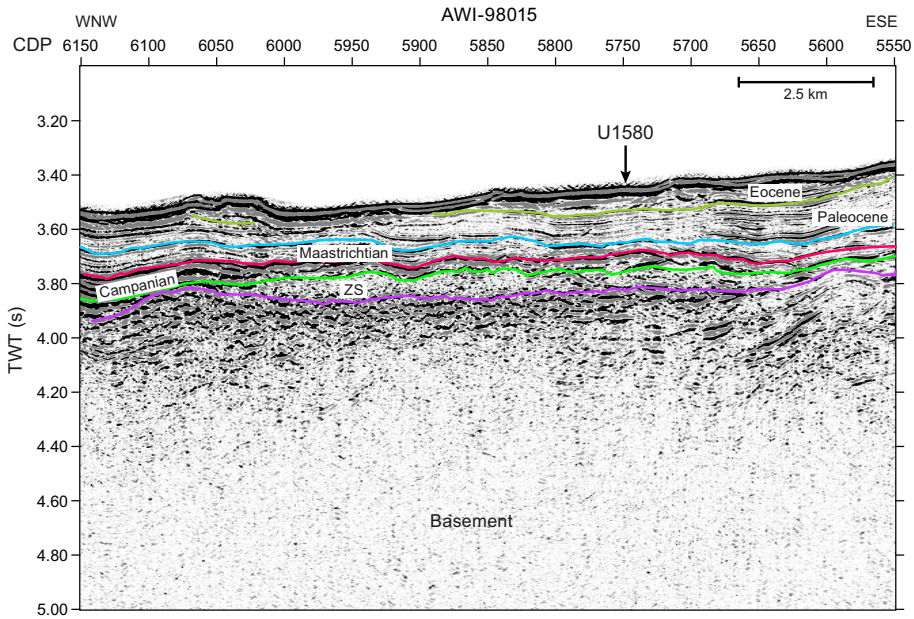

Figure F8. Seismic Line AWI-98015 showing Site U1580. Preliminary interpretation of seismic units according to the chronostratigraphic model is shown. The marked green reflection corresponds in structure to Reflector M of the pre-Expedition 392 seismostratigraphic model (Figure F4), the magenta reflection to Reflector LE, and the blue reflection to Reflector LO. CDP = common depth point, TWT = two-way traveltime, ZS = zeolitic silicified sediments.

392-U1580A-43R and 45R, and an intact basalt contact was cored at ~419–420 m CSF-A in Core 47R on 2 March. Coring in Hole U1580A continued until 1630 h on 5 March to a final depth of 533.9 m CSF-A. The basalt below ~495 m CSF-A cored at a ROP of 3–5 m/h, which is very fast for hard rock, and with good recovery. The overall ROP for RCB in Hole U1580A was 4.4 m/h.

At 1630 h on 5 March, the driller pumped a final sweep to clean the hole, flushing the mud completely out of the hole. The mechanical bit release tool was lowered, and the bit dropped at 1715 h. The drill string was tripped up to 80.7 m CSF-A in preparation for downhole logging. At 2145 h, the first logging string, the triple combination (triple combo), was assembled. The triple combo consists of the HNGS, HLDS, and MSS. The triple combo continued downlogging to a tag depth of 524.2 m WMSF. The logging run was completed, and the tool was out of the hole at 0630 h on 6 March. For the next downhole logging run, the Formation MicroScanner (FMS)-sonic suite was assembled and deployed at 0900 h. The FMS-sonic tool consists of the FMS, DSI, and HNGS. Two passes were conducted, with both reaching the bottom of the hole at ~521.5 m WMSF. The tools were back at the surface at 1535 h. For the final downhole logging run, the Ultrasonic Borehole Imager (UBI) tool string consisted of the UBI, General Purpose Inclinometry Tool (GPIT), and HNGS.

The UBI tool string was run in the hole at 1610 h. One pass was completed to 504.5 m WMSF. The second pass was aborted due to technical difficulties, and it was later determined that the transducer subassembly motor was sticking. The UBI logging run was completed with the tools at the surface at 0020 h on 7 March. The drill pipe cleared the rig floor at 0705 h, ending Hole U1580A. A total of 68 cores were taken in Hole U1580A over a 533.9 m interval (recovery = 65.7%). Total time on Hole U1580A was 233.52 h (9.73 days).

A new C-4 RCB bit was prepared, and after lowering the drill pipe to near the seafloor, the vessel was offset 20 m east. An RCB core barrel with center bit was installed, and Hole U1580B was spudded at 1710 h from a seafloor depth of 2571.5 m drilling depth below rig floor (DRF). The hole was drilled to 40.0 m CSF-A, and we used the RCB system to take Cores 2R–5R (to 77.8 m CSF-A). The drill pipe was tripped back to the ship and cleared the rig floor at 1430 h, ending Hole U1580B. The ROP for RCB coring averaged 7.2 m/h, and the 40 m drill down averaged 14.6 m/h. A total of four cores were taken in Hole U1580B over a 37.8 m interval (recovery = 62.9%). Total time on Hole U1580B was 31.44 h (1.31 days).

4.2.3. Principal results

4.2.3.1. Lithostratigraphy

Site U1580 consists of a 528.58 m sequence of calcareous and siliciclastic sediments and basalt. Basalt and sediments are interbedded in the lowermost ~120 m of the section. Fourteen lithostratigraphic units are defined (Figure **F9**; see **Lithostratigraphy** and Figure **F2**, both in the Site U1580 chapter [Bohaty et al., 2023b]), and Lithostratigraphic Units II and III are further divided into five subunits (IIa, IIb, IIc, IIIa, and IIIb). Lithostratigraphic Units I–III, V, VII, IX, XI, and XIII are largely composed of calcareous chalks and siliciclastic sandstones, siltstones, and claystones (see Figure **F2** in the Site U1580 chapter [Bohaty et al., 2023b]), whereas Lithostratigraphic Units IV, VI, VII, X, XII, and XIV are basalt (see **Igneous petrology** in the Site U1580 chapter [Bohaty et al., 2023b]).

Lithostratigraphic Unit I (0.00–3.42 m CSF-A) consists of light gray to light brown foraminiferal ooze with nannofossils. The lower contact with Lithostratigraphic Unit II at 3.42 m CSF-A is severely disturbed by drilling and is marked by a downcore change to white nannofossil ooze below the contact. Lithostratigraphic Unit II (3.42–293.51 m CSF-A) is a ~290 m sequence of Eocene–Campanian nannofossil ooze and chalk that is divided into Lithostratigraphic Subunits IIa–IIc. Lithostratigraphic Subunit IIa (3.42–16.73 m CSF-A) is ~13 m thick and is characterized by massively bedded pale yellow to light greenish gray nannofossil ooze with foraminifera. Lithostratigraphic Subunit IIb (19.40–207.11 m CSF-A) consists of ~188 m of white to light greenish gray nannofossil chalk. Lithostratigraphic Subunit IIb is more well-lithified (chalk versus ooze in the overlying subunit) and has higher carbonate content than Lithostratigraphic Subunit IIa. Lithostratigraphic Subunit IIc (207.11–293.51 m CSF-A) is 86 m thick and consists of light greenish gray calcareous chalk with cyclic bands of greenish gray or reddish brown clayey calcareous

chalk, with occasional chert layers. The boundary between Lithostratigraphic Subunits IIb and IIc is associated with an increase in MS and NGR values between ~200 and 220 m CSF-A. Carbonate content in Lithostratigraphic Subunit IIc is generally high (~80–95 wt%) (Figure **F9**); however, it is more variable than in Lithostratigraphic Subunits IIa and IIb, which likely reflects lower carbonate content in the brown and green clay-rich intervals. The K/Pg boundary occurs in Lithostratigraphic Subunit IIc near ~209.1 m CSF-A in an interval characterized by intense bioturbation and alternating bands of darker reddish brown clayey nannofossil chalk and lighter greenish gray nannofossil chalk with clay.

The Lithostratigraphic Unit II/III boundary at 293.51 m CSF-A is marked by a gradational change from reddish white clayey calcareous chalk to green zeolitic clastic sediments, corresponding to a notable decrease in carbonate content (see **Geochemistry** in the Site U1580 chapter [Bohaty et al., 2023b]) and a sharp increase in MS, drop in thermal conductivity, and increase in porosity (see **Physical properties** in the Site U1580 chapter [Bohaty et al., 2023b]) (Figure **F9**). Lithostratigraphic Unit III is 114 m thick and is divided into Lithostratigraphic Subunits IIIa and IIIb. Litho-

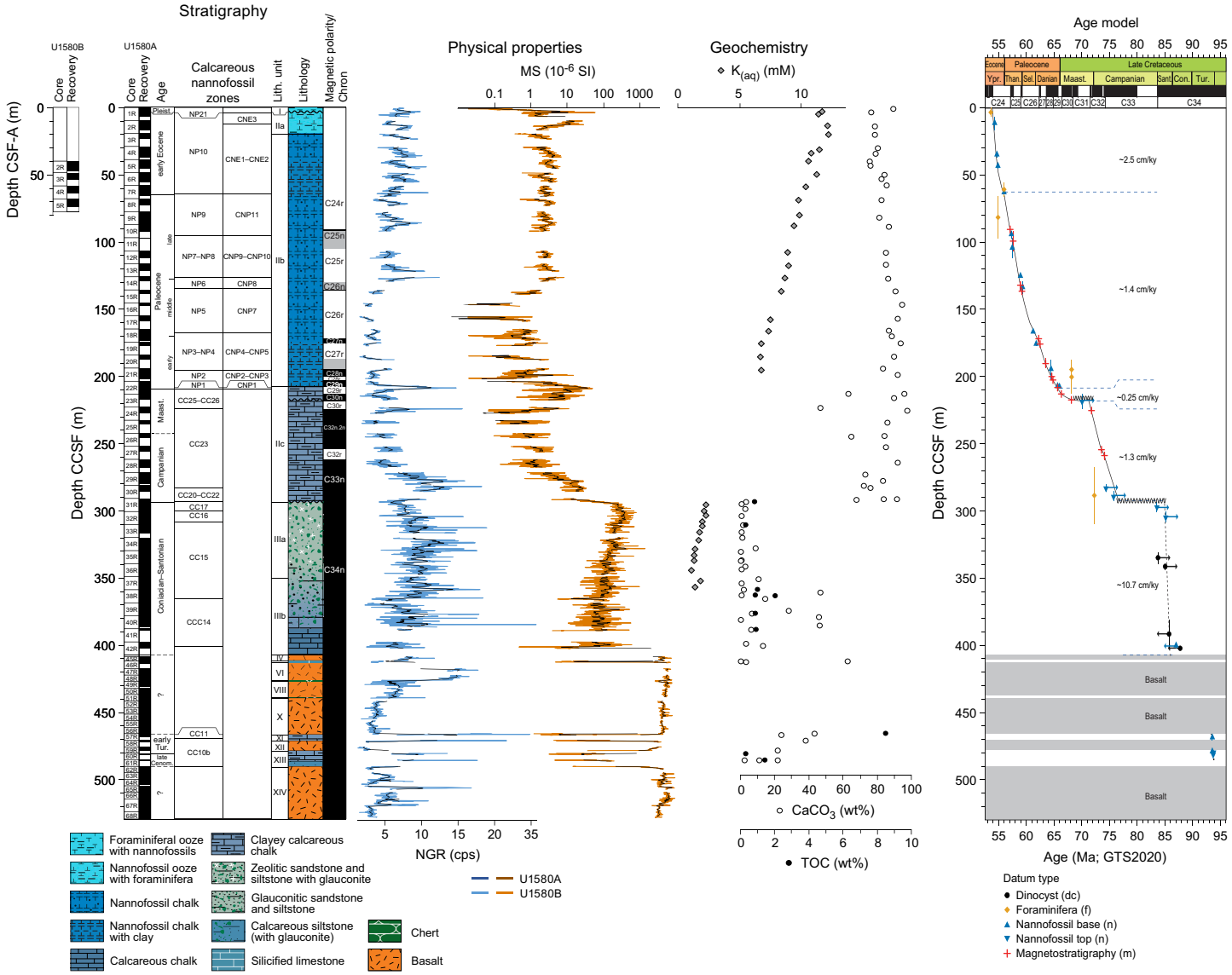

Figure F9. Stratigraphic summary, Holes U1580A and U1580B. Calcareous nannofossil zones: NP following Martini (1971); CC following Sissingh (1977); CN following Agnini et al. (2014). Black NGR data = 15-point moving average, cps = counts per second, black WRMSL MS data = 25-point moving average in black). K concentrations (gray diamonds) are from pore waters. Carbonate content (open circles) is from bulk sediments. TOC content (black circles) is measured on SRA. Age model is based on biostratigraphy and magnetostratigraphy, with reference to the GTS2020 (Gradstein et al., 2020) with estimated sedimentation rates.

stratigraphic Subunit IIIa (293.51–349.98 m CSF-A) is characterized by green zeolitic sandstones, siltstones, and claystones with glauconite (Figure **F9**) and has lower abundances of calcareous microfossils and carbonate content relative to the overlying units (see **Geochemistry** in the Site U1580 chapter [Bohaty et al., 2023b]). Lithostratigraphic Subunit IIIb (349.98–407.46 m CSF-A) is composed of green glauconitic siltstone and sandstone as well as light green calcareous chalk and light red calcareous sandstones, siltstones, and claystones. The light green intervals of Lithostratigraphic Subunit IIIb are calcareous chalk and contain common to abundant calcareous microfossils as well as carbonate mineral grains.

The first downhole occurrence of igneous rocks in Hole U1580A is at 407.46 m CSF-A (407.46 m CCSF), which is defined as the top of Lithostratigraphic Unit IV (Figure **F9**). The contact between Lithostratigraphic Subunit IIIb and the underlying basaltic Lithostratigraphic Unit IV was not recovered. Below Lithostratigraphic Unit IV at Site U1580, sediments are interbedded with basalts (see **Igneous petrology**), consisting of Lithostratigraphic Units V, VII, IX, XI, and XIII. Lithostratigraphic Unit V (411.76–412.82 m CSF-A; 411.76–413.16 m CCSF) consists of bluish gray to light reddish gray, thinly laminated silicified limestone and chert. Lithostratigraphic Unit VII (426.25–426.27 m CSF-A; 423.78–423.80 m CCSF) is a thin ~2 cm interval of calcareous chalk that is bounded by basalt above and below, which preliminary downhole log analysis suggests may be representative of a sedimentary interval up to ~1–2 m thick (see **Downhole measurements** in the Site U1580 chapter [Bohaty et al., 2023b]). Lithostratigraphic Unit IX (438.97–439.49 m CSF-A; 439.90–440.42 m CCSF) is a 52 cm interval of black chert that contains several white intersecting calcite veins. Lithostratigraphic Unit XI (466.63–471.60 m CSF-A; 467.09–471.60 m CCSF) consists of gray to black calcareous chalk, nannofossil-rich claystone, silicified limestone, and chert and includes an interval of abundant inoceramid (bivalve) fragments. Lithostratigraphic Unit XIII (478.53–490.54 m CSF-A; 478.53–490.54 m CCSF), the lowermost sedimentary unit recovered at Site U1580, consists of mixed lithologies including greenish gray, light brownish gray, and gray calcareous chalk; black claystone; siltstone; and clayey calcareous chalk.

4.2.3.2. Igneous petrology

A sequence of igneous units of varying thickness intercalated with sedimentary intervals was recovered in Lithostratigraphic Units IV, VI, VIII, X, XII, XIII, and XIV in the lowermost ~120 m of Hole U1580A (407.46–528.58 m CSF-A; 407.46–529.59 m CCSF) (Figure **F9**). Coring of the igneous intervals in this sequence yielded excellent recovery (average = ~84%). All igneous rocks recovered at Site U1580 are classified as aphyric or slightly plagioclase and/or olivine phyric basalts, with 10 igneous units defined on the basis of differences in macro- and microscopic texture and identifiable contacts (see Figure **F14** in the Site U1580 chapter [Bohaty et al., 2023b]). Throughout the recovered basalts, olivine crystals, as phenocrysts or in the groundmass, are completely replaced by alteration phases (predominantly clay minerals), contributing to the overall moderate-to-high degree of alteration of these units. In addition to near-continuous recovery of igneous successions, isolated basalt fragments were also recovered in primarily sedimentary intervals. For instance, Lithostratigraphic Unit XIII (478.53–490.54 m CSF-A; 478.53–490.54 m CCSF), which mainly comprises calcareous chalk, claystone, and siltstone, also contains three unoriented pieces of basalt; these basalt cobbles are distinct from the igneous units above and below Lithostratigraphic Unit XIII and likely represent a thin interval of basalt not coherently recovered at ~488 m CSF-A.

The intercalation of igneous bodies and sediment packages in Hole U1580A implies that these igneous units represent either lateral intrusions (sills) or that they were emplaced as lava flows on which sediments were deposited after each eruption. Based on several lines of evidence, we tentatively interpret this igneous succession as sills. Sharp igneous contacts and broad chilled margins (without volcanic glass), slow gradational changes in crystallinity (grain size) toward coarsely crystalline interiors, and certain mineralogic textures (subophitic and doleritic) of the recovered units resemble sills rather than lava flows. Additional compelling evidence for sill intrusions into sedimentary deposits is the thermal overprint or baking (contact metamorphism) of the adjacent sedimentary lithology, which is repeatedly observed in Hole U1580A. Similar reactions may also appear beneath thick lava flows but would not be expected above a flow because any sediments deposited on an existing lava body should be younger in age.

The recovery of such an extensive (>120 m) sill complex near the center of the Agulhas Plateau and at such high stratigraphic position (with respect to the bulk of the seismically defined plateau basement) was not expected. According to biostratigraphically constrained ages, the igneous bodies in Hole U1580A are located in sediments of late Cenomanian to Turonian or possibly Coniacian age (Figure **F9**; see **Chronostratigraphy** in the Site U1580 chapter [Bohaty et al., 2023b]). Therefore, if these units are sills, they must be younger than the age of the host sediment. Such late-stage or rejuvenated magmatism of oceanic plateaus is often characterized by alkaline composition. However, preliminary geochemical data of the recovered basalts (Sites U1579 and U1580) indicate that the sills have a tholeiitic composition (see **Geochemistry** in the Site U1580 chapter [Bohaty et al., 2023b]), which is characteristic of the main plateau building phase of oceanic LIPs. Postcruise research on the igneous units cored at Site U1580 will investigate links to the two igneous bodies that were also cored 98 km away at the base of Hole U1579D and are also tentatively interpreted as sills (see **Igneous petrology** in the Site U1580 chapter [Bohaty et al., 2023b]).

4.2.3.3. Micropaleontology

The sedimentary intervals of the 525.58 m succession cored at Site U1580 contain calcareous nannofossils, foraminifera, siliceous microfossils, and palynomorphs in varying abundance and preservation state (see Figure **F18** in the Site U1580 chapter [Bohaty et al., 2023b]). Calcareous nannofossils are abundant and moderately to well preserved in Paleogene and Pleistocene sediments (~0–209.1 m CSF-A), whereas abundance of calcareous nannofossils is more variable and preservation is generally poor to moderate in Cretaceous sediments (~209.1–491 m CSF-A), and some samples are barren. Despite variable preservation and abundance, nannofossils are present throughout the recovered sediment and provide excellent biostratigraphic control for the Paleogene and reasonably good control for the Cretaceous (Figure **F9**; see Figure **F19** in the Site U1580 chapter [Bohaty et al., 2023b]). Foraminifera are abundant and generally well preserved in the upper part of Site U1580. Below ~115 m CSF-A, foraminiferal abundance decreases and preservation deteriorates, although in some intervals of poor preservation delicate morphological features such as pore structures are preserved. Radiolarian fragments, as well as pyritized diatoms and radiolarians, were encountered in only a few samples from Site U1580. Trace numbers of palynofacies consisting of black phytoclasts are present in the Paleocene to lower Eocene sediments, whereas dinoflagellate cysts (dinocysts), miospores, and black phytoclasts are rare to abundant in the Cretaceous sediments, with some samples showing thermal alteration in the color of the palynomorphs (see Figure **F23** in the Site U1580 chapter [Bohaty et al., 2023b]).

4.2.3.4. Paleomagnetism

Paleomagnetic measurements were undertaken on all archive section halves from Holes U1580A and U1580B and on 68 discrete samples from Hole U1580A. Demagnetization experiments and rock magnetic analyses were also performed to constrain magnetic polarity and the magnetic mineralogy of the sedimentary and igneous units defined at Site U1580 (Figure **F9**). Paleomagnetic results indicate that the units sampled at Site U1580 are reliable recorders of magnetic field direction. Magnetic polarity was determined for 61 of the 68 cores measured from Hole U1580A and all four cores measured from Hole U1580B. Fifteen magnetic reversals were identified, and normal and reversed polarity intervals were correlated to chrons within the GPTS from the GTS2020 (Gradstein et al., 2020; Ogg, 2020). In combination with biostratigraphic results, these reversals were successfully correlated to the GPTS and span from the top of Chron C25n to the top of Chron C33n (~57–74 Ma; Thanetian–Campanian) (see Figure **F24** and Table **T11**, both in the Site U1580 chapter [Bohaty et al., 2023b]).

Rock magnetic results from Site U1580 indicate that the dominant magnetic mineralogy is a combination of both ferrimagnetic and antiferromagnetic minerals, likely magnetite and hematite. Both mineral groups occur in sedimentary Lithostratigraphic Unit I through Lithostratigraphic Subunit IIc (~0–300 m CSF-A), which transitions to dominantly ferrimagnetic minerals in Lithostratigraphic Units III–XIV (~300–530 m CSF-A). AMS measurements indicate that sedimentary units recovered at Site U1580 possess a typical oblate sedimentary fabric and that the basalts lack strong magnetic fabrics.

4.2.3.5. Stratigraphic correlation

At Site U1580, two holes were RCB cored: Hole U1580A to 533.9 m DSF (deepest recovery = 528.58 m CSF-A) and Hole U1580B from 40.0 to 77.8 m DSF (deepest recovery = 74.14 m CSF-A). In the interval where the stratigraphy of the holes overlapped (Cores 392-U1580A-5R through 8R [38.80–72.82 m CSF-A] and 392-U1580B-2R through 5R [40.00–74.14 m CSF-A]), recovery was 68% in Hole U1580A and 63% in Hole U1580B. Aligned core breaks between Holes U1580A and U1580B, and Cores 392-U1580A-5R through 8R and 392-U1580B-2R through 5R showed signs of drilling disturbance, hampering the construction of a splice, but features in individual cores may be correlated across holes. Compiled records of the cored intervals at Site U1580 demonstrate 66% recovery of the drilled interval spanning sediments of late Cenomanian to early Eocene age, as well as igneous rocks. A CCSF depth scale was constructed for Hole U1580A to enable visualization of results without overlap of recovered intervals between cores.

4.2.3.6. Chronostratigraphy

Calcareous nannofossils, planktonic and benthic foraminifera, dinocysts, and magnetostratigraphy provide age control for the uppermost Cenomanian–lower Eocene sediment cores recovered at Site U1580 (Figure **F9**; see **Micropaleontology**, **Paleomagnetism**, **Chronostratigraphy**, and Figure **F31**, all in the Site U1580 chapter [Bohaty et al., 2023b]). In the lowermost sequence of Site U1580, nannofossils constrain the age of sedimentary units interbedded with basalts (Lithostratigraphic Units XI and XIII; 466.63–471.60 m CSF-A; 478.53–490.54 m CSF-A) to the latest Cenomanian–earliest Turonian (~94 Ma). Lithostratigraphic Unit III sediments (~294–407 m CSF-A) overlying the basalts are dated to within the Coniacian–Santonian interval (85.2–86.1 Ma) using dinocyst and nannofossil biostratigraphy. Paleomagnetic results show continuous normal polarity throughout Lithostratigraphic Unit III due to deposition during what is interpreted as the C34n Superchron.

Lithostratigraphic Subunit IIc (207.11–293.51 m CSF-A) is dated to the Campanian–early Maastrichtian on the basis of nannofossil biostratigraphy and magnetostratigraphy (see Figure **F31** in the Site U1580 chapter [Bohaty et al., 2023b]). Although several polarity reversals are preliminarily correlated to the GPTS in this interval, nannofossil biostratigraphy only provides broad age constraints, and further higher resolution postcruise study is required. A hiatus is inferred at ~224 m CSF-A, truncating the lower Maastrichtian succession, with a duration of at least 2 My based on calcareous nannofossil biostratigraphy and magnetostratigraphy. The K/Pg boundary (66.04 Ma) is identified in Core 392-U1580A-22R (Figure **F9**), near 209.1 m CSF-A based on biostratigraphy and lithologic correlation to Site U1579. The exact position of the K/Pg boundary in Hole U1580A will be confirmed and/or refined during postcruise analysis.

Between ~63 and 209.1 m CSF-A, the Paleocene section of Site U1580 is continuous at the resolution of 18 shipboard bio- and magnetostratigraphic (Chrons C24r through C29r; ~56–66 Ma) age tie points (Figure **F9**). The Paleocene/Eocene boundary is identified at ~63 m CSF-A in Hole U1580A and ~62 m CSF-A in Hole U1580B based on nannofossil biostratigraphy, a distinct color change, and physical properties (see **Lithostratigraphy** and **Physical properties**, both in the Site U1580 chapter [Bohaty et al., 2023b]). Seven foraminiferal and nannofossil biostratigraphic datums provide age constraints within the lower Eocene succession (~3–63 m CSF-A), constraining the age to ~53.6–56 Ma. Because of low magnetization intensity, no magnetic reversals were identified in the lower Eocene section of Site U1580. The uppermost sediments recovered at Site U1580 (Lithostratigraphic Unit I; 0–3.42 m CSF-A), which rest on a hiatal surface above the Eocene sediments below, are dated to the Pleistocene based on foraminiferal and nannofossil biostratigraphy.

4.2.3.7. Geochemistry

The geochemistry program at Site U1580 was designed to characterize the composition of bulk sediment and IW and diagnose the abundance of volatile hydrocarbons for routine safety monitoring. Methane above the detection limit was not found in any samples. Propene (17.4 ppmv), isopentane (5.8 ppmv), and iso-hexane (3.9 ppmv) were detected at ~87 m CSF-A.

IW samples were analyzed in Hole U1580A to 356.16 m CSF-A, below which IW was not extractable. IW alkalinity, pH, and major anion and cation concentrations all show distinctive downhole

trends. Alkalinity values decrease from roughly 3.0 mM at the top of the sedimentary sequence to 0.3 mM at 311.27 m CSF-A (see Figure **F32** in the Site U1580 chapter [Bohaty et al., 2023b]). pH values are relatively constant at 7.4 to <7.7 throughout the upper 185 m CSF-A and increase to 7.7–8.3 below 295 m CSF-A. Of the major anions, sulfate decreases from ~28 mM at 3.75 m CSF-A to ~22 mM at ~356 m CSF-A, and chloride increases downhole from 573 mM to values exceeding 600 mM below ~300 m CSF-A (see Figure **F33** in the Site U1580 chapter [Bohaty et al., 2023b]). The major cation sodium shows a slight decrease from its seawater value (481 mM) in the upper part of the hole to ~328 m CSF-A; below this depth, it decreases to 452 mM at 356.16 m CSF-A. Calcium increases from ~10.7 mM at 3.75 m CSF-A to 86.0 mM at ~343 m CSF-A. Magnesium inversely mirrors the calcium profile and decreases from 51.1 mM at 3.75 m CSF-A to 3.0 mM at 343.81 m CSF-A. Potassium notably decreases downhole from 11.7 mM at 3.75 m CSF-A to 1.2 mM at 343.81 m CSF-A.

In total, 83 sediment samples from Site U1580 were analyzed for bulk carbon and nitrogen content to 485.99 m CSF-A. Total carbon (TC) and $CaCO_3$ range 0–14.5 wt% and 0–97.2 wt%, respectively, which is consistent with the observed pelagic nannofossil oozes and chalks, zeolitic sand/siltstones, limestone, and claystone lithologies (Figure **F9**). Average TOC is 0.4 ± 1.2 wt% with minimum and maximum concentrations of 0 and 9.3 wt%, respectively. Five samples with TOC content exceeding 1 wt% are from below ~315 m CSF-A, and two samples composed of calcareous siltstone and black claystone exceed 5 wt% and are from the lowest part of the hole deeper than 410 m CSF-A.

Eleven samples from nine representative sills drilled at Site U1580 were selected for ICP-AES analyses. Based on classic discrimination diagrams for igneous rocks (see Figure **F37** in the Site U1580 chapter [Bohaty et al., 2023b]), all samples classify as tholeiitic basalts.

4.2.3.8. Physical properties

Physical properties of sediments and igneous rocks recovered at Site U1580 were measured on whole-round core sections, split half core sections, and discrete samples to a total depth of 528.58 m CSF-A in Hole U1580A. Complementary downhole logging data sets were also collected from Hole U1580A (see **Downhole measurements** in the Site U1580 chapter [Bohaty et al., 2023b]). Between ~40 and 74 m CSF-A, cores from Hole U1580A and Hole U1580B overlap stratigraphically. Measured variations in physical properties arise from lithification with increasing burial depth and from variations in lithologic composition. The upper part of this interval shows small variations in MS, NGR, *P*-wave velocity, and density (Lithostratigraphic Unit I and Lithostratigraphic Subunits IIa and IIb; 0–207.11 m CSF-A). The overall higher *P*-wave velocities and densities and color change toward darker and more reddish layers in the lower part of Lithostratigraphic Subunit IIb are attributed to diagenetic changes and an increase in clay content. Anomalous physical properties downhole were recorded in the zeolitic sandstone, siltstones, and claystones of Lithostratigraphic Subunit IIIa (293.51–349.98 m CSF-A), characterized by a decrease in bulk density, increase in porosity, low *P*-wave velocities (as low as ~2000 m/s), and a sharp drop in thermal conductivity compared to the strata above and below. Increased MS and NGR values also correlate with the zeolitic sediments of Lithostratigraphic Unit III (293.51–407.46 m CSF-A) (Figure **F9**). Deconvolved Natural Gamma Radiation Logger (NGRL) spectral data indicate that potassium is enriched to ~0.5–2.0 wt% in the zeolitic sandstones to claystones of Lithostratigraphic Unit III (see Figure **F42** in the Site U1580 chapter [Bohaty et al., 2023b]), likely reflecting an increase in authigenic minerals rich in potassium such as glauconite and celadonite. Exceptional peaks in NGR (related to high uranium content) were also observed in a few dark layers in Cenomanian–Turonian sediments (Lithostratigraphic Unit XII; ~471.6–478.53 m CSF-A; 471.60–478.53 m CCSF) sandwiched between basalt layers (Lithostratigraphic Units XI and XIII).

4.2.3.9. Downhole measurements

Downhole measurements at Site U1580 consisted of wireline logging in Hole U1580A without downhole temperature measurements. In addition to standard sonic and MS data, high-resolution density, natural gamma ray, neutron porosity, electrical resistivity, and FMS and UBI imagery provide a continuous borehole record, documenting lithologies of unrecovered stratigraphic intervals where coring gaps occurred in Hole U1580A (see Figure **F47** in the Site U1580 chapter [Bohaty et al., 2023b]). HSGR data from the HNGS downhole log indicate that sediments of Lithostrati-

graphic Units II (~3–294 m WMSF) and III (~294–407 m WMSF) occupy two distinct compositional domains of potassium/thorium ratios. Potassium-rich Lithostratigraphic Unit III is characterized by anomalously high porosity (>60%), which is confirmed by MAD analysis (see **Physical properties**). The integrated interpretation of downhole data is instrumental to identify the true thickness of sediments and nature of their contacts with basalts below 407 m WMSF (see **Lithostratigraphy** and **Igneous petrology**, both in the Site U1580 chapter [Bohaty et al., 2023b]). The UBI and FMS images display various degrees of alteration/fracturing in basalts and sharp transitions to the interbedded sediments. The sedimentary rocks sandwiched between basalt units are characterized by elevated uranium content with peaks at about 2 ppm. The cross-dipole setup of acoustic logging enables a detailed core-to-seismic integration that includes analysis of elastic anisotropy.

4.3. Site U1581

4.3.1. Background and objectives

Site U1581 is located on the deep, flat part of the Transkei Basin (35°40.8654′S, 29°39.0055′E) at 4591 m water depth. This area of the Transkei Basin has a smooth bathymetry with water depths between 4000 m and 4600 m, and no apparent dip can be recognized in the site's vicinity. The site is located on the crossing point of Seismic Lines AWI-20050008 and AWI-20050014. The seismic data show that the Transkei Basin is characterized by the mounded structure of the Agulhas Drift, an elongate sediment drift about 220 m thick and rising about 200 m above the seafloor (Figure **F10**). This sequence shows a number of high-amplitude internal reflections. Below the base Reflector P (pink line, Figure **F10**) of the Agulhas Drift, the reflection characteristics change to lower reflectivity. The Agulhas Drift is underlain by the M Drift, a sediment drift formed during the Oligocene and Miocene (Schlüter and Uenzelmann-Neben, 2008b). The M Drift shows a strike almost perpendicular to the Agulhas Drift, which is indicative of a strong change in the direction of the prevalent bottom current. Reflector M dominates the seismic image of the M Drift in the middle of the sequence. Reflector E forms the base of Seismic Unit 2, which is only up to 30 m thick. Reflectors K-T and B characterize the deepest seismic unit above rugged oceanic basement (Figure **F10**).

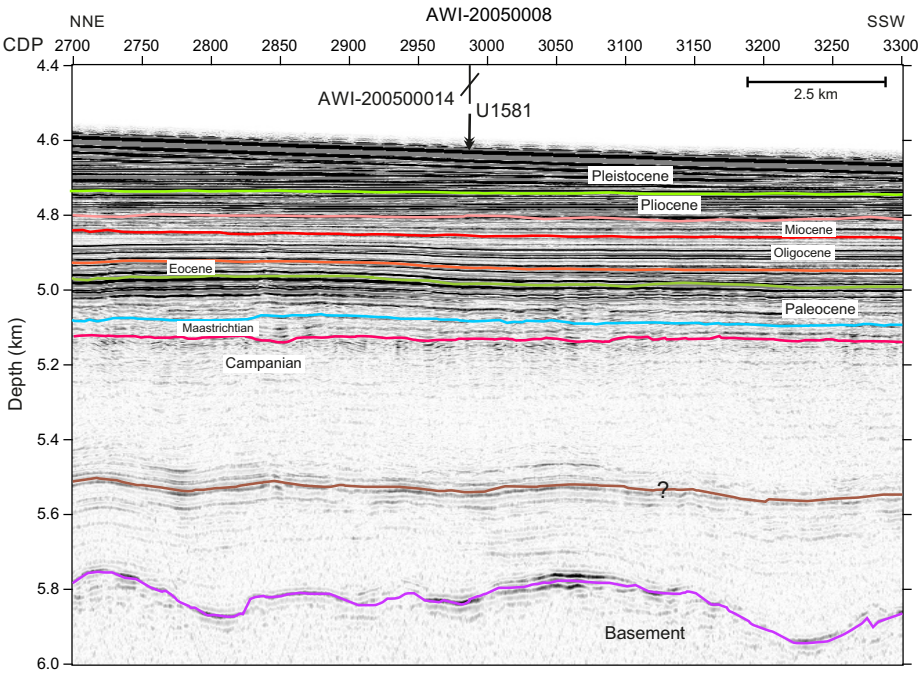

Figure F10. Seismic Line AWI-20050008 showing Site U1581. Preliminary interpretation of seismic units according to the chronostratigraphic model are shown. The marked purple reflection corresponds in structure to the top of basement (Figure F5), the brown reflection to what was originally interpreted as a black shale prior to drilling, the pale green reflection to Reflector O, the red reflection to Reflector M, and the rose reflection to Reflector P. CDP = common depth point.

Site U1581 was chosen to recover an Upper Cretaceous and Paleogene sedimentary record, as well as a partial Neogene sequence. This site was especially dedicated to target Reflector B in the Cretaceous sequence. This reflector was interpreted to represent black shales, and recovery of material from the reflector and above/below was intended to provide information on the formation of black shales in connection with ocean anoxia. Integration of seismic profiles with the drilling results will allow direct dating of the observed Seismic Unconformities K-T, E, O, M, and P and interpreting their causes. Further objectives concern paleoenvironment and paleodepth of the Transkei Basin. At this site, critical intervals of ocean–climate transitions such as Mi1 and Oi1 glaciations, the PETM, the K/Pg boundary, and OAEs 2 and 3 were expected to be documented in the sedimentary record.

4.3.2. Operations

After completing the 338 nmi voyage to Site U1581, the vessel arrived on site at 2345 h on 9 March 2022. The thrusters were lowered, and the ship was switched to full DP mode at 2357 h. The APC/XCB bottom-hole assembly (BHA) was assembled, and we began tripping pipe to the seafloor. We attempted to shoot the first APC core from 4573.8 meters below sea level (mbsl); however, this resulted in no recovery (water core). Two additional attempts from 4578.8 and 4583.8 mbsl also resulted in no recovery. Hole U1581A was successfully spudded at 2115 h on 10 March, recovering 6.88 m, and the seafloor was calculated at 4591.4 mbsl. APC coring continued to 207.2 m CSF-A (Core 24H). The APCT-3 tool was run on Cores 4H, 7H, 10H, and 13H, with good data collected for all four. Pressure in the pipe increased while drilling the rathole of Core 24H. A mud sweep was pumped, and the core barrel was pulled back to the surface while the crew continued to circulate and condition the hole with an additional two mud sweeps. Site U1581 hole locations, water depths, and the number of cores recovered are listed in Table **T1**.

The core barrel recovered 8.11 m (Core 392-U1581A-25G; the designation for a core with an uncertain depth). A fray in the core line was discovered and repaired. Cores 26H–29H advanced to 233.8 m CSF-A. We then switched to the HLAPC system. Cores 30F–38F advanced to 276.1 m CSF-A. We then switched to the XCB system, and Cores 39X–41X advanced to 300.5 m CSF-A; however, strong swells and resultant low recovery and poor core quality led to the termination of coring in Hole U1581A at 1800 h on 13 March. A total of 40 cores (plus a ghost core) were taken in Hole U1581A over a 300.5 m interval (recovery = 90.9%). Total time on Hole U1581A was 104.4 h (4.35 days).

The drill string was pulled out of Hole U1581A, and pipe was tripped back to the vessel. The bit cleared the rig floor at 0825 h on 14 March. It was determined that a compassionate evacuation was needed for a crew member. An attempt was made to recover the acoustic positioning beacon; however, it was ultimately deemed lost.

The vessel was switched from DP to cruise mode at 0945 h, and the thrusters were up and secured at 1014 h, beginning the sea passage to Gqeberha (formerly known as Port Elizabeth). The vessel arrived at the edge of the Gqeberha harbor at approximately 0700 h on 15 March. Clearance for the departing crew member was received at 1300 h, and they disembarked the vessel via launch at 1402 h. We then began the transit back to Site U1581, arriving just before noon on 16 March. The BHA with a C-4 bit was made up and tripped to 4499.7 m DRF before a slip and cut of the drilling line. Hole U1581B was spudded at 0230 h on 17 March. An RCB barrel with a center bit was used to drill ahead to 289 m CSF-A, with several mud sweeps during the drill down. The ROP during the drill down averaged 46.2 m/h. The center bit was recovered, and coring commenced with Core 2R at 1445 h on 17 March. Coring continued through 24 March with Core 74R at 997.1 m CSF-A, the final depth for Hole U1581B.

In preparation for downhole logging, the hole was swept with sepiolite mud to flush cuttings and the bit released at 1835 h on 24 March. The hole was further displaced with mud, and the bottom of the drill string was placed at 77.8 m CSF-A for downhole logging.

The first downhole logging run was with the Versatile Seismic Imager (VSI). The tool began its descent but encountered a solid ledge at 222.4 m CSF-A. The tool was worked up and down for almost an hour, but was unsuccessful at passing the ledge. The decision was made to bring the tool

back to surface and lower the drill pipe to cover the ledge. The VSI cleared the rig floor, and the drill pipe was run in to 408.5 m CSF-A. Because of the lack of daylight for another VSI run, a modified triple combo tool string was made up with the DSI in place of the HRLA unit. The tool string consisted of the HNGS, HLDS, DSI, and MSS.

Upon make-up, a problem was found with power to the lower portion of the tool string. This was replaced, and the tool string was deployed. At 2606.8 m DRF (still within the water column), there was growing evidence of an electrical fault with the tool. The tool was brought back to the surface, where it was repaired and redeployed. The triple combo tool reached 1300.0 m DRF but was again showing an electrical fault, and the decision was made to terminate logging. The tool string was pulled out of the hole, and the cause of the electrical fault was much later determined to be the conductors in the collector and pinched conductors in the logging head. The triple combo tools were disassembled, and the drill string was tripped back to the vessel, clearing the seafloor at 0555 h and the rig floor at 1510 h on 26 March, ending Hole U1581B. A total of 73 cores were taken in Hole U1581B over a 708.1 m interval (recovery = 76%). Total time on Hole U1581B was 243.12 h (10.13 days).

4.3.3. Principal results

4.3.3.1. Lithostratigraphy

A ~994 m thick Pleistocene–Campanian sedimentary succession composed of calcareous and siliciclastic sediments was recovered at Site U1581 (Figure **F11**). The upper part of the succession is relatively carbonate rich, whereas the lower part is dominantly siliciclastic in composition. The sedimentary sequence is divided into Lithostratigraphic Units I and II, both of which are further divided into two subunits (Ia, Ib, IIa, and IIb) (Figure **F11**).

Lithostratigraphic Unit I (0.00–390.05 m CSF-A) is a 390 m sequence of Pleistocene–upper Paleocene biogenic ooze with variable amounts of sand, silt, and clay. The unit is divided into two subunits (Ia and Ib) on the basis of a higher concentration of siliciclastic material in Lithostratigraphic Subunit Ib. Lithostratigraphic Subunit Ia (Hole U1581A = 0.00–198.24 m CSF-A) consists principally of greenish gray, light yellowish brown, and light brown clayey nannofossil ooze with biosilica, nannofossil ooze, and grayish green foraminiferal ooze with sand, silt, and clay intervals. Where fully recovered, the basal contacts of thin sand intervals that overlie nannofossil oozes are typically sharp or erosive. Carbonate content in Lithostratigraphic Subunit Ia is highly variable, ranging ~20–80 wt% in biogenic intervals and <1 wt% in siliciclastic intervals (Figure **F11**). Lithostratigraphic Subunit Ib (Hole U1581A = 198.24–292.11 m CSF-A; Hole U1581B = 289.00–390.05 m CSF-A) consists predominantly of siliciclastic sand, silt, and clay with occasional intervals that are nannofossil rich. Biogenic sediments are less common in Lithostratigraphic Subunit Ib and occur as irregular, thin layers within thick packages of sand and silt. Siliciclastic sediments consist of medium- to fine-grained sand and silt layers that are massive or laminated and are occasionally normally graded. Carbonate content is generally low (<2 wt%) in Lithostratigraphic Subunit Ib, except for in discrete decimeter-scale nannofossil-rich intervals, where it can be as high as ~40 wt%. The contact between Lithostratigraphic Units I and II at 390.05 m CSF-A is marked by a change in lithology from intercalated siliciclastic and calcareous sediments to dominantly siliciclastic sediments, as well as a decrease in average carbonate content (Figure **F11**).

Lithostratigraphic Unit II (395.70–994.02 m CSF-A) is a ~598 m thick middle Paleocene to Campanian sequence of siliciclastic sediments consisting of sand, silt, and clay and sandstone, siltstone, and claystone. This unit is divided into two subunits (IIa and IIb) based on the degree of lithification (clay versus claystone). Lithostratigraphic Subunit IIa is ~90 m thick and consists of dark to very dark greenish gray fine-grained sand and silt, clayey silt, and very dark greenish gray or black clay, clay with silt, and minor greenish gray to black silicified siltstone with glauconite. Bedding ranges from massive to laminated, with normal grading in some intervals. Well-preserved inoceramids (bivalves) and other shell fragments are observed macroscopically throughout the subunit. The contact between Lithostratigraphic Subunits IIa and IIb is sharp, with Lithostratigraphic Subunit IIb marked by a sharp decline in MS, an increase in dry density, and a decrease in porosity. Lithostratigraphic Subunit IIb is ~508 m thick and consists of dark to very dark greenish gray siltstone, fine- to medium-grained sandstone, and very dark greenish gray or black claystone (Figure

F11). The sand layers become less frequent downhole and are not present below ~791 m CSF-A. Mass transport deposition is inferred from repeated fining upward sequences of sand to silt or silt with soft-sediment deformation features such as convolute lamination or load casts. However, finer grain sizes in Lithostratigraphic Unit II (clays and fine silts) suggest a more distal location with respect to the sediment source in comparison to Lithostratigraphic Unit I.

4.3.3.2. Micropaleontology

The 994.02 m sedimentary succession recovered at Site U1581 consists of varying proportions of siliciclastic sediment and biogenic ooze that contain calcareous nannofossils, foraminifera, dinocysts, radiolarians, and diatoms in varying abundance and preservation state (see Figure F10 in the Site U1581 chapter [Bohaty et al., 2023c]). In Lithostratigraphic Subunit Ia (0–198.24 m CSF-A; Pleistocene to late Miocene), calcareous nannofossils and foraminifera are generally abundant and moderately to well preserved. Reworking of nannofossils is particularly prevalent in more siliciclastic rich sediments. Diatoms and other siliceous microfossils (including radiolarians and silicoflagellates) are common to abundant and well preserved in the uppermost ~7 m of the sequence.

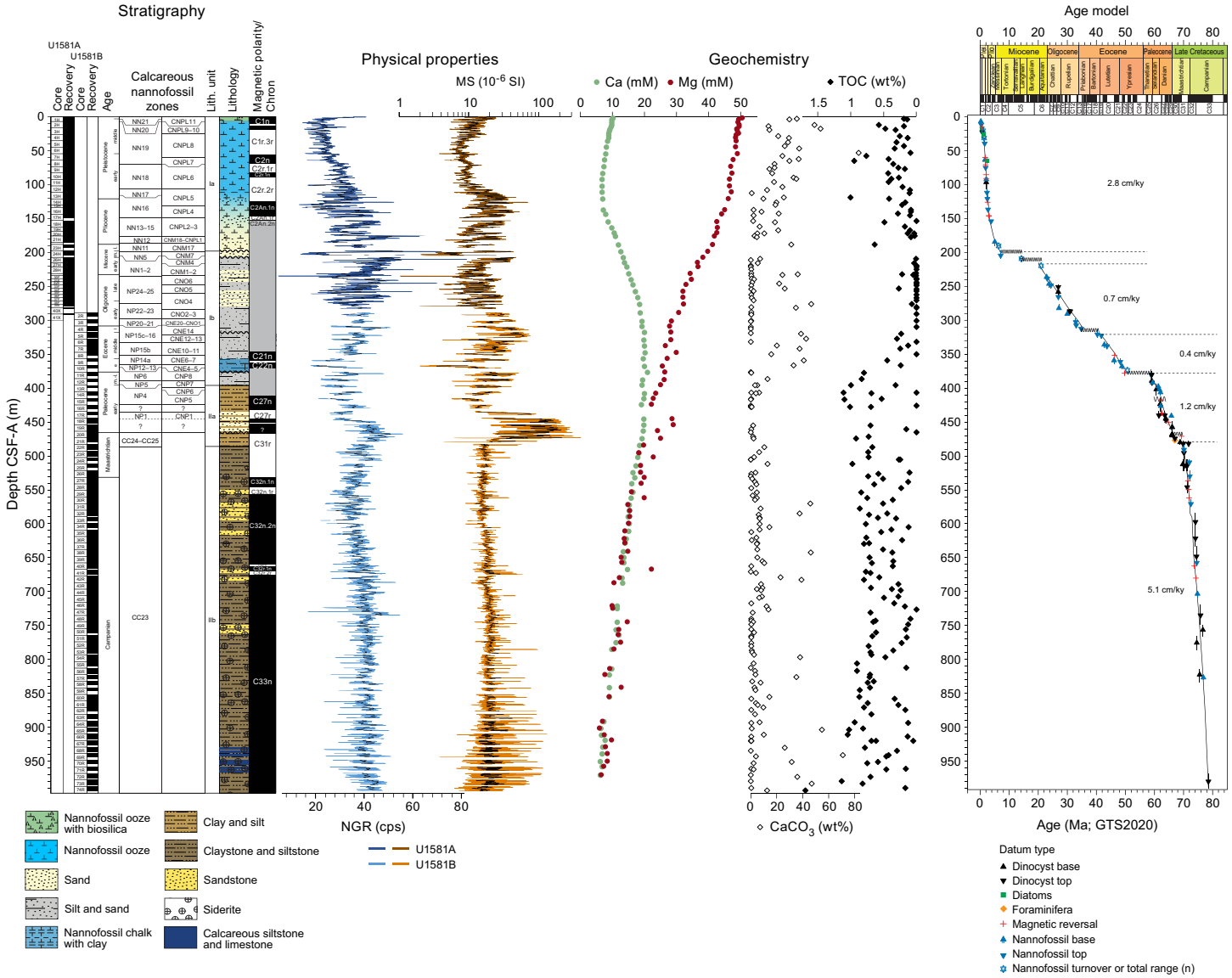

Figure F11. Stratigraphic summary, Site U1581. Calcareous nannofossil zones: NP following Martini (1971); CC following Sissingh (1977); CN following Agnini et al. (2014). Black NGR data = 15-point moving average, cps = counts per second, black WRMSL MS data = 25-point moving average. Ca (green circles) and Mg concentrations (red circles) are from pore waters. Carbonate (white diamonds) and TOC (black diamonds) contents are from bulk sediments (open circles). Age model is based on biostratigraphy and magnetostratigraphy, with reference to the GTS2020 (Gradstein et al., 2020) with estimated sedimentation rates.

Below this, moderately preserved diatoms are present in few to rare numbers to ~110 m CSF-A, whereas radiolarians are common to ~93 m CSF-A and present in few numbers to ~175 m CSF-A. Dinocysts are well preserved when present, but their abundance varies throughout Lithostratigraphic Subunit Ia from present in the Pleistocene and Pliocene to sparse in the Miocene.

In Lithostratigraphic Subunit Ib (198.24–390.05 m CSF-A; late Miocene–middle Paleocene), calcareous nannofossils are common to abundant and moderately preserved in many samples; however, they are occasionally rare or absent entirely in some intervals, particularly in coarser grained lithologies. Foraminifera are abundant but poorly to moderately preserved at the top of this subunit. Below ~240 m CSF-A, foraminifera are either absent or present in low numbers and poorly preserved. Siliceous microfossils are absent in this subunit. Poor preservation of dinocysts and miospores continues into the top of Lithostratigraphic Subunit IIb between ~198 and 243 m CSF-A. Dinocysts and miospores are rare to common in the Oligocene (~247–283 m CSF-A), absent in the Eocene (~294–371 m CSF-A), and common to abundant in the Paleocene (~378–396 m CSF-A).

In Lithostratigraphic Unit II (395.70–994.02 m CSF-A; Paleocene–Campanian), calcareous nannofossil abundance and preservation varies significantly. Nannofossils are present in few to common numbers in only some Paleocene samples, and many samples are completely barren. Nannofossils are generally present but low in abundance in Cretaceous samples, but they are surprisingly well preserved, particularly between ~470 and 770 m CSF-A. Below this depth, abundance decreases and preservation deteriorates, with the lowermost sediments devoid of nannofossils. Foraminifera are almost entirely absent in the >63 µm size fraction in Lithostratigraphic Unit II; however, small foraminifera <20 µm are observed in smear slides throughout the unit. Pyritized diatom fragments are common throughout much of this unit. Although they are often fragmented, some samples contain nearly complete pyritized diatom valves. Preservation of dinocysts and miospores is moderate to good in Lithostratigraphic Unit II. Both are common to abundant throughout all samples investigated and contain rich and diverse assemblages, which will provide ample opportunity for postcruise study of the terrestrial and marine paleoenvironmental evolution of the region.

The siliciclastic component of Site U1581 sediments includes coarse-grained units with sharp bases and normal grading that are interpreted as turbidites. As a result, an uncertain proportion of the microfossils found in the sediments of Site U1581 were likely transported from nearby shallower settings. Consequently, there is a significant component of reworked microfossils throughout the sedimentary succession at Site U1581, which complicates identification of the biohorizon tops. However, the biohorizons identified demonstrate a clear age progression, suggesting that transported sediments were deposited quasi-contemporaneously.

4.3.3.3. Paleomagnetism

Paleomagnetic measurements were undertaken on archive section halves from Holes U1581A and U1581B and on 110 discrete samples from both holes. Paleomagnetic experiments included alternating field demagnetization, AMS, and IRM acquisition. These experiments were performed to constrain magnetic polarity and the magnetic mineralogy of sedimentary units from Site U1581. Paleomagnetic results are of variable quality, and magnetic polarity could only be determined from ~50% of the cores recovered from Hole U1581A and ~65% from Hole U1581B. From cores with clear magnetic polarity, nineteen reversals were identified and correlated to chrons within the GPTS from the GTS2020 (Gradstein et al., 2020; Ogg, 2020) (see Table **T11** in the Site U1581 chapter [Bohaty et al., 2023c]). These include Chrons C1n through C2Ar (Pleistocene–Pliocene) in Hole U1581A and Chrons C20r through C33n (middle Eocene–Campanian) in Hole U1581B (Figure **F11**). Rock magnetic results indicate that the magnetic mineralogy comprises both ferrimagnetic and antiferromagnetic minerals. There is no observable trend in magnetic mineralogy with depth or between sedimentary units. AMS measurements indicate that the majority of samples from Site U1581 possess a typical oblate sedimentary fabric; however, samples from the basal ~75 m of Lithostratigraphic Subunit IIb possess a prolate fabric, possibly indicating a tectonic imprint.

4.3.3.4. Chronostratigraphy

Calcareous nannofossils, planktonic foraminifera, diatoms, dinocysts, and magnetostratigraphy provide age control for the Campanian to Pleistocene sediment sequence recovered at Site U1581 (Figure **F11**). For the Campanian–Paleocene interval, nannofossils and dinocysts provide biostratigraphic age constraints that guided correlation of paleomagnetic reversals in Lithostratigraphic Unit II and the lower part of Lithostratigraphic Subunit Ib (994.02–367.45 m CSF-A) to the GPTS (Ogg, 2020). The lowermost strata recovered at Site U1581 are dated to ~78.5 Ma based on nannofossil biostratigraphy. Consistent normal polarity from the base of the hole (994.02 m CSF-A) to 675.68 m CSF-A further constrains the age of the oldest sediment cored to younger than 79.9 Ma, within Chron C33n. Biostratigraphic datums also constrain two paleomagnetic reversals at ~676 and ~658 m CSF-A to the Chron C33n/C32r.2r and C32r.1r/C32n.2n reversals, respectively (Figure **F11**). The Campanian/Maastrichtian boundary (72.17 Ma) is identified at ~532 m CSF-A based on nannofossil biostratigraphy. Upsection, several additional nannofossil and dinocyst biohorizons constrain three paleomagnetic reversals at ~558, 545, and 532 m CSF-A to the Chron C32n.2n/C32n.1r, C32n.1r/C32n.1n, and C32n.1n/C31r reversals, respectively. Dinoflagellate biostratigraphy indicates an early Maastrichtian age for the strata between ~532 and 467 m CSF-A. The Maastrichtian–Danian stratigraphy at Site U1581 is complex (see Figure **F32** in the Site U1581 chapter [Bohaty et al., 2023c]), with one or more possible hiatuses, significant reworking, and a complicated magnetic polarity signal. Shipboard biostratigraphic and magnetostratigraphic analysis suggests that the K/Pg boundary and upper Maastrichtian is missing at a hiatus in Core 392-U1581B-20R at ~466–467 m CSF-A.

The Paleocene sequence recovered at Site U1581 also has a complex stratigraphy, with varying sedimentation rates and at least two hiatuses based on age constraints from dinocysts, nannofossils, and paleomagnetic reversals (see Figure **F30** in the Site U1581 chapter [Bohaty et al., 2023c]). The sequence from ~466 to 444 m CSF-A has predominantly normal polarity and contains a number of dinocyst biohorizon bases, which are associated with the first phase following the mass extinction at the K/Pg boundary. Nannofossils from this interval comprise a dominantly reworked Maastrichtian assemblage, but nannofossil markers for the base of the Paleocene are identified at ~444 m CSF-A. Dinocyst biostratigraphy constrains the age of the interval at ~439–436 m CSF-A to 64.0–63.4 Ma. The paleomagnetic signal through this sequence is complex and will be refined in postcruise research. The top of the Paleocene interval is dated to older than 58.80 Ma at ~382 m CSF-A based on nannofossil biostratigraphy. There is a significant change in the assemblage at this stratigraphic level, indicating another hiatus and that much of the upper Paleocene and lower Eocene is missing at Site U1581.

The base of the Eocene section recovered at Site U1581 is placed at ~367 m CSF-A and dated to ~50.65 Ma based on nannofossil biostratigraphy. Nannofossil biostratigraphy indicates a late middle Eocene age at ~321 m CSF-A, and low sedimentation rates (~0.4 cm/ky) were calculated for the lowermost Eocene section. Nannofossil biostratigraphy further supports the presence of a hiatus or highly condensed interval at ~315 m CSF-A spanning the middle to upper Eocene. A lower Oligocene to lower Miocene sedimentary succession between ~306 and 215 m CSF-A is constrained by 14 calcareous nannofossil and dinocyst biostratigraphic datums (Figure **F11**; see Figure **F30** in the Site U1581 chapter [Bohaty et al., 2023c]). Because of a poor paleomagnetic signal, no magnetic reversals were identified in this interval. Nannofossil biostratigraphy dates the interval at ~215 m CSF-A to 20.98 Ma (early Miocene). Above this depth, there are two hiatuses or highly condensed intervals in the Miocene succession spanning ~21 to 7 Ma.

The age-depth model for the uppermost Miocene to Pleistocene sedimentary succession at Site U1581 is constrained by 20 diatom, dinocyst, and calcareous nannofossil biostratigraphic datums and 8 magnetic reversals (see Figure **F31** in the Site U1581 chapter [Bohaty et al., 2023c]). Nannofossil biostratigraphy dates the base of this interval to ~7 Ma at ~186 m CSF-A and the top of this interval to 0.29 Ma at ~1 m CSF-A. Sedimentation rates are interpreted to be relatively constant through the Pliocene–Pleistocene interval, although the frequent occurrence of turbidites likely means that sedimentation rates vary at a finer scale (see Figure **F31** in the Site U1581 chapter [Bohaty et al., 2023c]).

4.3.3.5. Geochemistry

The geochemistry program at Site U1581 was designed to characterize the composition of bulk sediment and IW and report on the presence and abundance of volatile hydrocarbons for routine safety monitoring. Methane values range 0.1–1458.2 ppmv. Hydrocarbons with longer chain lengths up to n-hexane (C_6) were detected from 490.52 to 990.12 m CSF-A (bottom of Hole U1581B). The consistent presence of higher hydrocarbons up to hexane in the lower part of Hole U1581B is consistent with a thermogenic origin of the hydrocarbons. Notably, ethane/methane (C_2/C_1) ratios are markedly elevated between 490.52 and 655.22 m CSF-A, with a maximum at 610 m CSF-A.

IW samples were analyzed in Holes U1581A and U1581B to 978.88 m CSF-A, and IW was extractable in all but the lowermost sample from Core 392-U1581B-74R (990.02 m CSF-A). Alkalinity values increase from roughly 3.4 mM in the shallowest sample at 2.96 m CSF-A to 10.0 mM at 74.81 m CSF-A. Alkalinity values then decrease to 1.4 mM at 277.5 m CSF-A and remain relatively constant between 0.831 and 2.335 mM below this depth. pH values range ~7.5–8.1 to ~625 m CSF-A, and ammonium values follow a trend quite similar to alkalinity in all Hole U1581A samples, with a maximum value of approximately 1146 µM at ~100 m CSF-A before decreasing to ~257 µM at ~256 m CSF-A. Ammonium then steadily increases to the bottom of the hole to 1098 µM (see Figure **F34** in the Site U1581 chapter [Bohaty et al., 2023c]).

Of the major anions, sulfate decreases from 28.4 mM at 2.96 m CSF-A to 14.0 mM at ~138 m CSF-A. Sulfate then increases slightly to 18.3 mM at 358.31 m CSF-A before decreasing again to 3.8 mM at 722.91 m CSF-A. Chloride decreases downhole from 574 mM in the uppermost part of the section to as low as 455.5 mM in the deepest part of the section. Sodium shows a marked increase in variability below ~200 m CSF-A, with concentrations ranging ~440–527 mM (see Figure **F34** in the Site U1581 chapter [Bohaty et al., 2023c]). Magnesium concentrations decrease downhole from 50.7 to 6.7 mM at the bottom of the hole. Calcium decreases from 10.3 mM at 2.96 m CSF-A to 6.9 mM at 93.81 m CSF-A before increasing to a maximum concentration of 21.1 mM at 377.71 m CSF-A. Below ~400 m CSF-A, calcium concentrations decrease to ~6 mM at the base of the section. Potassium concentrations decrease from a maximum of 11.4 mM at 19.37 m CSF-A to 1.2 mM at 600.70 m CSF-A. Below this depth, potassium concentrations remain stable between ~1 and 2 mM.

In total, 204 sediment samples were analyzed for bulk carbon and nitrogen analyses at Site U1581. TC and carbonate weight percentages range 0–10.1 and 0–83.4 wt%, respectively, which is consistent with the deposition of pelagic biogenic oozes and lithologic observations (Figure **F11**). Greater variability and overall the highest carbonate content is observed in biogenic oozes between the seafloor and 198 m CSF-A. Below 200 m CSF-A, inorganic carbon and carbonate content typically decrease to below 10 wt% and average 1.0 and 8.1 wt%, respectively. The main carbonate mineral phase is likely calcite in the biogenic ooze above 200 m CSF-A; however, in the more siliciclastic sediments below 200 m CSF-A, the carbonate content may include other carbonate minerals, including siderite and dolomite. Despite uncertainty in the carbonate mineral phases present, carbonate carbon persists in selected samples to the bottom of the analyzed sedimentary section (~993 m CSF-A). The average TOC content is 0.5 ± 0.3 wt% with minimum and maximum concentrations of 0 and 1.7 wt%, respectively. Average TOC is slightly elevated to 0.6 wt% from 200 m CSF-A to the base of the recovered section at Site U1581.

4.3.3.6. Physical properties

Standard measurements of physical properties were made on cores from Holes U1581A and U1581B using the WRMSL, Section Half Multisensor Logger (SHMSL), and NGRL track instruments. Discrete measurements were also made for MAD analysis, thermal conductivity, and *P*-wave velocities on the PWC system.

Core disturbance was common in Hole U1581A cores collected with the APC, HLAPC, and XCB systems, affecting the continuous track measurements of physical properties for cores. Discrete sampling for thermal conductivity and MAD analyses avoided core disturbance wherever readily identifiable. Many of the clay-rich lithologies at Site U1581 expanded in volume upon recovery, likely altering some physical properties. In Hole U1581B, the trends in physical properties show a

continuation of observations recorded in Hole U1581A. Average NGR levels and deconvolved uranium, thorium, and potassium concentrations are higher at Site U1581 compared to the two previous sites on the Agulhas Plateau, reflecting lower carbonate content and higher clay content in the Transkei Basin (Figure **F11**; see Figures **F39** and **F40**, both in the Site U1581 chapter [Bohaty et al., 2023c]). *P*-wave velocity, thermal conductivity, and bulk density values all increase downhole through the biogenic oozes of Lithostratigraphic Subunit Ia in the upper 198.24 m. At the Lithostratigraphic Subunit Ia/Ib boundary (198.24 m CSF-A), a sharp ~0.2–0.3 g/cm^3 increase in bulk density occurs where a hiatus is indicated by biostratigraphic analysis (see **Micropaleontology** and **Chronostratigraphy**, both in the Site U1581 chapter [Bohaty et al., 2023c]). Finer scale changes in physical properties at Site U1581, such as in NGR and MS (Figure **F11**), are associated with decimeter-scale nannofossil ooze/chalk beds, which are likely turbiditic in origin (see **Lithostratigraphy** in the Site U1581 chapter [Bohaty et al., 2023c]). A major increase in MS to ~400 instrument units (IU) occurs in the clayey silts and silty clays of Lithostratigraphic Subunit IIa (395.70–486.07 m CSF-A) and corresponds with the K/Pg boundary interval. The grain density of claystones in Lithostratigraphic Subunit IIb (486.07–994.02 m CSF-A) is high (~2.75–2.85 g/cm^3) and likely relates to the presence of authigenic minerals such as pyrite and siderite. *P*-wave velocity at Site U1581 increases downhole relatively linearly from ~1650 m/s at the seafloor to ~2200 m/s at the base of Lithostratigraphic Unit II (994.02 m CSF-A).

4.3.3.7. Downhole measurements

Downhole measurements at Site U1581 included formation temperature measurements in Hole U1581A and limited downhole logging data. Because of electrical connection problems during downhole logging in Hole U1581B, only natural gamma ray downhole logging data were collected between ~80 and 220 m WMSF using the Enhanced Digital Telemetry Cartridge (EDTC) run at the top of the triple combo tool string (see **Operations**). The logging data provide downhole natural gamma ray data across the poorly recovered interval at the base of Pliocene–Pleistocene deposits (see **Lithostratigraphy** and **Chronostratigraphy** in the Site U1581 chapter [Bohaty et al., 2023c]). These data allow for detailed correlation between Cores 392-U1581A-10H through 26H and downhole logging data. Borehole formation temperatures were measured using the APCT-3 tool during recovery of Cores 392-U1581A-4H (35.4 m CSF-A), 7H (54.4 m CSF-A), 10H (92.4 m CSF-A), and 13H (120.9 m CSF-A). Temperature measurements were of good quality, displaying characteristic thermal cooling curves (see Figure **F47** in the Site U1581 chapter [Bohaty et al., 2023c]). A geothermal gradient of ~37.0°C/km and a heat flow of ~47.3 mW/m^2 were calculated using Bullard's method (Bullard, 1954).

4.4. Site U1582

4.4.1. Background and objectives

The northern Agulhas Plateau is characterized by a rough topography and a number of basement highs separated by depressions with only a thin sedimentary cover. In between the interpreted basement highs, thicker sediment packages filling depressions or sediment drifts are observed. This distribution of sedimentary sequences attests to the strong erosional/nondepositional influence of the Agulhas Retroflection, as well as Circumpolar Deepwater flowing over the northern Agulhas Plateau. Furthermore, the northern slope of the Agulhas Plateau lies under the influence of North Atlantic Deepwater and Antarctic Bottom Water, both of which shape sediment drifts. Site U1582 is located on the flank of one of those basement highs (37°1.5002′S, 24°59.7168′E) at 3441 m water depth, where a small ledge is formed (Figure **F12**). The seismic data show basement below an ~100 m thick sedimentary sequence, which is characterized by Reflectors M and LE (see **Background**). The uppermost part of basement further shows only few internal reflections (Figure **F12**), which differs from the seismic character of the basement at Sites U1579 and U1580. This has been interpreted to represent more homogeneous basalt at Site U1582.

Site U1582 was selected to recover both the thin Paleogene–Cretaceous sedimentary cover and basement samples. This site was especially dedicated to recover an extended record of basement material to unravel the nature of the basement and provide information on its age and geochemistry. Additional objectives include identifying potential late-stage magmatism and its effect on sedimentary sequences. Integration of seismic profiles with the drilling results will allow direct dating

of the observed Seismic Unconformities M and LE and interpreting their causes, and recovery of the sediment/basement interface will provide information on the age of the oldest sediments above the basement as well as the water depth and environment at the time of deposition. At this site, a thin sediment sequence from the mid-Cretaceous to mid-Paleogene was expected to be drilled, spanning the long-term climate transition from the Cretaceous greenhouse to potentially the early Paleogene. The recovery of basement rocks at this site on the northern Agulhas Plateau was expected to help address fundamental questions about the formation of this LIP.

4.4.2. Operations

The vessel arrived at Site U1582 at 1420 h on 27 March 2022. The thrusters were lowered starting at 1424 h, the vessel was switched from cruise to DP mode at 1440 h, and the rig floor was given the all clear. A new C-7 bit with a mechanical bit release was made up, and a four-stand RCB BHA was run into the hole starting at 1645 h. The drill pipe was lowered to 3378.3 m DRF, the sinker bars were installed, and the RCB core barrel was deployed. Site U1582 hole locations, water depths, and the number of cores recovered are listed in Table **T1**.

The first coring attempt at 2340 h was a water core. Starting on 28 March, four more attempts were made to get the first core. On the sixth attempt, Hole U1582A was spudded at 0405 h, with Core 1R recovering 1.9 m. The seafloor was established at 3429.4 mbsl. Coring continued, and basement was reached at 42.7 m CSF-A. Half cores were taken on Cores 6R and 7R. Core 7R was cored to 48.0 m CSF-A, but more than 100% was recovered (48.68 m CSF-A). Coring was terminated at 1915 h to trip out of the hole because severe weather was expected over the site within 24 h.

The pipe was tripped out of the hole, clearing the seafloor at 1945 h. On 29 March at 0215 h, the pipe trip was completed with the BHA at the rig floor. The bit cleared the rig floor at 0455 h, ending Hole U1582A. The rig floor was secured at 0600 h, and the vessel was switched to cruise mode at 0604 h. The thrusters were raised and secured by 0618 h, and the sea passage for waiting on weather began with the vessel transiting north at 10.6 kt. The vessel turned and took a westerly heading at 1818 h. Beginning on 31 March, the vessel turned south and then east to return to Site U1582. A total of seven cores were taken in Hole U1582A over a 48 m interval (recovery = 38.5%). Total time on Hole U1582A was 38.16 h (1.59 days).

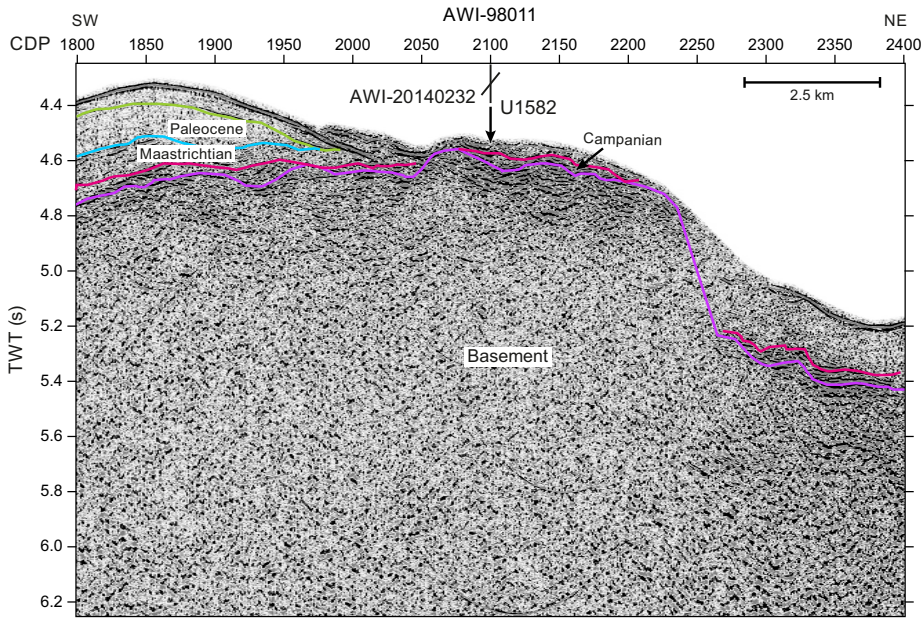

Figure F12. Seismic Line AWI-98011 showing Site U1582. Preliminary interpretation of seismic units according to the chronostratigraphic model is shown. The marked purple reflection corresponds in structure to the top of basement (Figure F4), the magenta reflection to Reflector M, the blue reflection to Reflector LE, and the green reflection to Reflector LO. CDP = common depth point, TWT = two-way traveltime.

On 1 April, the vessel arrived back at Site U1582. The thrusters were lowered starting at 1228 h, and the ship was switched to DP mode at 1245 h, ending the waiting on weather window. The vessel was positioned 10 m west of Hole U1582A. A new C-7 RCB bit was made up, and the BHA and pipe were tripped to the seafloor. A core barrel with a center bit was dropped, and Hole U1582B was spudded at 2315 h on 1 April. Seafloor was set at 3440.7 m DRF (by offset). Hole U1582B was drilled down to a hard contact at 36.3 m CSF-A. The center bit was retrieved, and coring began at approximately 0530 h on 2 April. Core 2R was on deck at 1100 h. The ROP was very slow, averaging just over 1 m/h because the hard basalt formation and shallow depth of the hole limited how much weight could be put on the bit. Coring continued to 3 April, and Core 5R was recovered at a final depth of 55.6 m CSF-A (recovery to 53.73 m CSF-A).

The weather over the site was expected to deteriorate over the next 2 days, thus forcing us off site and into an early transit to Cape Town, South Africa. Coring was terminated at 0230 h on 3 April, and the pipe was tripped back to the vessel. The bit cleared the rig floor at 1250 h, ending Hole U1582B and Site U1582. The vessel was switched to cruise mode at 1236 h, the thrusters were raised and secured by 1249 h, and we began our sea passage to Cape Town, South Africa, at 1250 h with the vessel making a wide turn to the northwest. A total of four cores were taken in Hole U1582B over a 19.3 m interval (recovery = 52.2%). Total time on Hole U1582B was 48 h (2.0 days). Expedition 392 officially ended with the first line ashore at 1154 h on 7 April.

4.4.3. Principal results

4.4.3.1. Lithostratigraphy

Site U1582 consists of a 40.92 m sequence of sediments overlying a 16.9 m interval of basalt with intercalated thin layers of sediment. The sequence recovered at Site U1582 is divided into Lithostratigraphic Units I and II (Figure **F13**). Lithostratigraphic Unit I is entirely comprised of sediments and further divided into Lithostratigraphic Subunits Ia and Ib, and Lithostratigraphic Unit II consists of pillow basalts with interspersed sediments.

Lithostratigraphic Unit I (Hole U1582A = 0.00–40.42 m CSF-A; Hole U1582B = 36.30–36.83 m CSF-A) is a ~40 m thick sequence of clayey nannofossil ooze, clayey silt, and clayey nannofossil ooze with sand and manganese nodules in the upper sections and limestone with manganese nodules at the base (Figure **F13**; see Figure **F2** in the Site U1582 chapter [Bohaty et al., 2023d]). The unit is divided into Lithostratigraphic Subunits Ia and Ib based on a downhole increase in lithification. Both subunits contain variable amounts of sand, silt, clay, and manganese nodules. Lithostratigraphic Subunit Ia consists of light brown clayey silt, nannofossil ooze, clayey nannofossil ooze with sand, and manganese nodules. At 2.00–2.11 m CSF-A, there is a dark brown, ~11 cm manganese nodule, and there are additional small nodules of manganese throughout the entire subunit. From 7.32 m CSF-A to the base of the subunit, medium to coarse sand-sized and occasionally pebble-sized manganese nodules are present. The contact between Lithostratigraphic Subunits Ia and Ib was not recovered and occurs in an interval of poor recovery between Cores 392-U1582A-4R and 5R (21.71–31.07 m CSF-A).

Lithostratigraphic Subunit Ib consists of limestone, with one cobble-sized manganese nodule at 45.5 m CSF-A. The limestone ranges from light gray to pale yellow and contains clasts of altered basalt and carbonate intraclasts, including pebble-sized angular calcite crystals. Manganese dendrites are also present in the light gray limestone. Carbonate content decreases from ~30 wt% at 0.83 m CSF-A to <5 wt% at 2.48 m CSF-A and remains below 10 wt% to 21.57 m CSF-A. The contact between Lithostratigraphic Units I and II was not recovered.

Lithostratigraphic Unit II (Hole U1582A = 40.42–48.68 m CSF-A; Hole U1582B = 36.83–53.73 m CSF-A) is ~17 m thick and consists largely of pillow basalts with occasional layers/pockets of sediments between pillow basalts (Figure **F13**; see Figure **F2** in the Site U1582 chapter [Bohaty et al., 2023d]). The sediment includes limestones and volcaniclastic material; the limestones range from pale yellow to light brown to light grayish green. In the pale yellow and light brown limestones, limonite is present at contacts with the basalt. Dendritic manganese and calcite veins are also present in the limestone intervals.

4.4.3.2. Igneous petrology

Igneous rocks were first reached at 40.92 m CSF-A in Hole U1582A and 36.83 m CSF-A in Hole U1582B, below sedimentary Lithostratigraphic Subunit Ib (Figure **F13**). In Hole U1582A, Lithostratigraphic Unit II is comprised of a 7.76 m sequence of pillow lava basalts with thin, intercalated limestone pockets. Thirteen igneous units were identified and defined as individual inflationary pillow lava lobes in Hole U1582A. The sedimentary material in Lithostratigraphic Unit II consists of thin (<10 cm) limestones and is considered to be pockets of carbonate sediment that occupy interstices between individual pillow lobes.

The upper part of Lithostratigraphic Unit II in Hole U1582A (Igneous Units 1–3) is composed of predominantly plagioclase phyric pillow basalts, which all show a yellowish brown alteration pattern. There is abundant fresh glass along the chilled contacts of the pillows, as well as an outer layer of palagonized (weathered) glass. The basalt in the interior of the lobes is fine-grained, moderately to highly altered, and sparsely plagioclase phyric. Many intervals are also moderately vesicular with typical, radially arranged vesicle trains inward of the chilled margin, with all of the vesicles filled with calcite. The common yellowish brown color of the basalts in the upper part of Lithostratigraphic Unit II indicates considerable weathering and oxidation. The lower part of

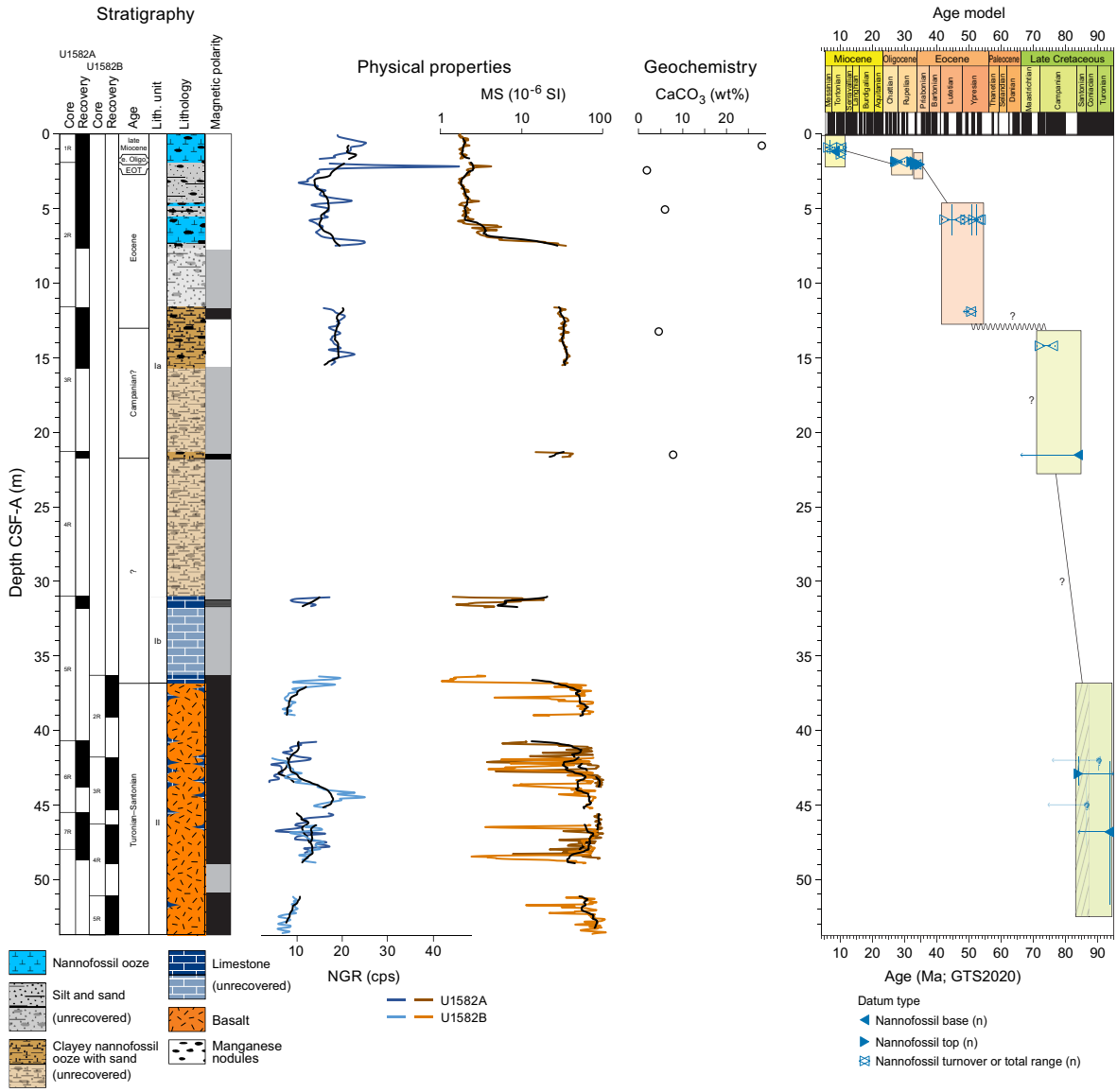

Figure F13. Stratigraphic summary, Site U1582. Black NGR data = 15-point moving average, cps = counts per second, WRMSL MS data = 25-point moving average. Carbonate contents are from bulk sediments (open circles). Age model is based on biostratigraphy, with reference to the GTS2020 (Gradstein et al., 2020).

Lithostratigraphic Unit II in Hole U1582A (Igneous Units 4–13) is also composed of predominantly plagioclase phyric pillow basalts. However, most of these basalt units possess a natural gray color and show no or only minor signs of oxyhydroxide staining, indicating a lesser degree of oxidative weathering than the uppermost basalts of the succession.

Hole U1582B was spudded about 20 m away from Hole U1582A and delivered the same principle lithologies, although igneous rocks were first encountered ~4 m shallower (36.83 m CSF-A) below sedimentary Lithostratigraphic Subunit Ib. A 16.86 m sequence of pillow lava basalts was penetrated before drilling ceased at 53.69 m CSF-A in Hole U1582B. The ~4 m shallower occurrence of the igneous basement in comparison to Hole U1582A may attest to the considerable lateral variability of pillow lava flow fields, which likely created an irregular sediment/basalt contact at this site. In total, 27 igneous units were identified in Hole U1582B, including 26 pillow lava units and one sequence of a hyaloclastite breccia. As in Hole U1582A, the pillow lava units were defined and interpreted as individual inflationary lava lobes.

The entire igneous succession cored in Holes U1582A and U1582B is interpreted as a stack of pillow lava lobes based on observed structures such as curved chilled margins, the presence of thick (fresh and altered) glass rinds along these margins, radially arranged vesicle trains, and concentric vesicle bands parallel to the curved margins (see Figures **F10** and **F11**, both in the Site U1582 chapter [Bohaty et al., 2023d]). The basalts recovered in both holes are characterized by the presence of pockets or intervals of interpillow carbonate sediment often recovered in direct contact with the pillow rims. The presence of calcareous nannofossils in at least some of these carbonate pockets rules out a purely diagenetic origin of the carbonate. Instead, the evidence of mingling of plastic lava with unconsolidated sediments is tentatively interpreted as peperite, implying an interaction of lava and coexisting sediment during eruption.

4.4.3.3. Micropaleontology

The 53.73 m succession recovered at Site U1582 contains calcareous nannofossils and foraminifera in varying abundance. The sediments are barren of siliceous microfossils, and samples from the site were not processed for palynomorphs because of the nature of the sediment and time constraints near the end of the expedition. The sedimentary succession recovered at the site above basalt (Hole U1582A = 0–40.92 m CSF-A; Hole U1482B = 36.30–36.83 m CSF-A) primarily consists of nannofossil ooze with abundant manganese nodules, together with clayey silt and sand (Lithostratigraphic Subunit Ia; 0–21.76 m CSF-A) overlying limestone (Lithostratigraphic Subunit Ib; Hole U1582A = 31.00–40.92 m CSF-A; Hole U1528B = 36.30–36.83 m CSF-A) and indicates a highly condensed section dated to the Miocene to Campanian(?) (Figure **F13**). Basalt was encountered at 40.92 m CSF-A in Hole U1582A and 36.83 m CSF-A in Hole U1582B (Lithostratigraphic Unit II). The basalt shows clear pillow structures with thin intervals of intercalated sediment that contain sparse nannofossils that indicate a Santonian to Turonian age.

Calcareous nannofossils are abundant and moderately to poorly preserved in the nannofossil ooze of Lithostratigraphic Subunit Ia (0–21.76 m CSF-A). The clayey silt and clayey sand beds in this subunit are barren or nearly barren of nannofossils. Nannofossil preservation generally decreases from the top of the hole through Lithostratigraphic Subunit Ia. Nannofossils are very rare and poorly preserved in the limestone of Lithostratigraphic Subunit Ib. In contrast, nannofossils are present in rare to few numbers and moderately preserved in the greenish gray limestone intercalated with basalt, whereas they are rarer and show poorer preservation in the yellowish brown limestones associated with the basalt. Foraminifera are present in the upper four cores of Hole U1582A (Lithostratigraphic Subunit Ia; 0–21.73 m CSF-A), and preservation deteriorates downhole from good to poor.

4.4.3.4. Paleomagnetism

Paleomagnetic measurements were undertaken on all archive section halves from Holes U1582A and U1582B and on four discrete samples from Hole U1582A. Demagnetization experiments were performed on both sedimentary and igneous units recovered from Site U1582. Results indicate that the sampled units at Site U1582 are reliable recorders of magnetic field directions. Magnetic polarity was constrained from all measured cores. Intervals of both positive and negative inclination were identified in Hole U1582A, indicative of reversed and normal geomagnetic polarity,

respectively (Figure **F13**). All measured cores from Hole U1582B had negative inclination (normal polarity). Because of the condensed sediment interval collected in each hole, correlation to the GPTS (Gradstein et al., 2020; Ogg, 2020) was difficult; however, we suggest a correlation with Chron C34n of the predominantly normal polarity zone observed from ~21 m CSF-A downhole (see **Chronostratigraphy**).

4.4.3.5. Chronostratigraphy

Calcareous nannofossils, foraminifera, and magnetostratigraphy provide age control for the Campanian(?) to upper Miocene sediments recovered at Site U1582 in Lithostratigraphic Unit I (Figure **F13**). The sedimentary cover is very thin (~40 m) at Site U1582 yet represents a long period of time (as much as 70 My), indicating very low sedimentation rates and/or significant erosion. The presence of abundant manganese nodules is consistent with this observation. The low sedimentation rates and other processes such as reworking of older sediment and burrowing, together with coring disturbance, make this a particularly challenging site for chronostratigraphy. Because of significant mixing, the youngest age diagnostic taxa within a given sample or set of samples was used for biostratigraphic age assessment, with outlier bioevents excluded that appear to result from drilling disturbance or contamination.

Nannofossils and magnetostratigraphy provide age constraints for the basalt and sediments of Lithostratigraphic Unit II (Hole U1582A = 48.68–40.92 m CSF-A; Hole U1582B = 53.73–36.83 m CSF-A). The limestones intercalated with basalt contain a sparse, moderately preserved Late Cretaceous nannofossil assemblage. Nannofossil marker taxa suggest an early Turonian to Santonian age (~93.7–84 Ma). The broad age interpretation of Turonian–Santonian is consistent with the persistent normal magnetic polarity of the basalt, which can therefore be assigned to Superchron C34n (Figure **F13**). Given the sparse nature of the assemblages, postcruise research may provide additional nannofossil age constraints for the sediments recovered within the basalts.

The lowermost sediments recovered above basalt at Site U1582 are limestones in Lithostratigraphic Subunit Ib (Hole U1582A = 40.92–31.07 m CSF-A; Hole U1582B = 36.83–36.30 m CSF-A), which contain only very rare and poorly preserved Cretaceous nannofossils that provide no additional age control. The limestone shows normal magnetic polarity with no reversals between it and the basalt below. This may suggest that the limestone was deposited during the long Cretaceous Normal Superchron (C34n), indicating an age of Santonian or older; however, this age assessment is very tentative.

The nannofossil ooze, clayey silt, sand, and manganese nodules of Lithostratigraphic Subunit Ia (Hole U1581A = 21.76–0 m CSF-A) show predominantly reversed magnetic polarity with some intervals of normal polarity usually associated with manganese nodules. Nannofossil assemblages in this subunit often include a significant component of reworking and presence of multiple biostratigraphic marker taxa indicating broad age ranges (Figure **F13**). The 21.76–11.90 m CSF-A interval of Lithostratigraphic Subunit Ia contains a solely Cretaceous nannofossil assemblage with background taxa similar to those in the sediment intercalated with the basalt of Lithostratigraphic Unit II, indicating a Campanian to earliest Maastrichtian age despite the dominance of older (Coniacian) species. The dominantly reversed polarity of this interval also precludes a Coniacian age. However, the possibility that the nannofossil assemblage is entirely reworked through this interval cannot be discounted.

Samples between 11.90 and 7.63 m CSF-A contain assemblages of mixed ages with a significant component of older material reworked into younger sediment, together with likely contamination from younger material due to fall-in. However, although the nannofossil assemblage contains Cretaceous taxa similar to those in the deeper samples, the presence of Paleogene nannofossils indicate an early Eocene or younger age for this interval.

The 6.76–4.71 m CSF-A interval is assigned an early to early middle Eocene age (~54–47 Ma) based on nannofossil biostratigraphy, and the 1.98–1.85 m CSF-A interval is assigned an Eocene to mid-Oligocene age (~35–27 Ma). Nannofossils indicate a late Miocene age between ~10.9 and 5.5 Ma for the 1.35–0.43 m CSF-A interval. Foraminifera in the mudline sample indicate a very young (Pleistocene–recent) age for the seafloor.

4.4.3.6. Geochemistry

The geochemistry program at Site U1582 was designed to characterize the composition of bulk sediment and IW and report on the presence and abundance of volatile hydrocarbons for routine safety monitoring.

A total of six headspace samples were taken and analyzed for routine safety monitoring. Hydrocarbons in headspace samples were detected in Hole U1582A. Methane was above the detection limit in three samples, with concentrations of 0.7 and 0.5 ppmv in samples from Cores 2R and 3R, respectively. Hydrocarbons with longer chain lengths up to n-hexane (C_6) were not detected in any of the headspace samples.

Samples for IW were collected from the upper 15 m of Hole U1582A, where soft sediment was present. Alkalinity values range 2.4–2.9 mM. pH values range 7.6–7.7. No further shipboard analyses were completed on IW samples from Site U1582 because of the small number of samples collected.

In total, five sediment samples were obtained for bulk carbon, nitrogen, and sulfur analyses at Site U1582. TC and carbonate weight percentages (where carbonate is reported as calcium carbonate weight percentage) range 0.2–3.4 and 1.9–28.1 wt% at Site U1582, respectively. Carbonate is elevated (28.1 wt% as $CaCO_3$) in the uppermost sample (0.82 m CSF-A) from Lithostratigraphic Subunit Ia, which is a clayey nannofossil ooze that encompasses the upper 21.71 m at this site, as compared to Lithostratigraphic Subunit Ib below 31 m CSF-A, which averages 5.2 wt% $CaCO_3$ (Figure **F13**). In Lithostratigraphic Subunit Ib, inorganic carbon averages 0.6 wt%. TOC is zero for all samples except Sample 1R-1, 82–83 cm, which has a concentration of <0.1 wt%. Total nitrogen was measured but remained below 0.1 wt% (average = 0.04 wt%), which is at or close to the detection limit, for the samples analyzed from Hole U1582A.

Total sulfur concentrations range from below detection limit to 0.4 wt%.

4.4.3.7. Physical properties

Standard measurements of physical properties were made on cores from Holes U1582A and U1582B using the WRMSL, SHMSL, and NGRL. Discrete measurements were also made for MAD analysis, thermal conductivity, and *P*-wave velocities on the PWC system. Physical properties data from Site U1582 show a progression with depth that delineates the poorly consolidated clayey nannofossil ooze of Lithostratigraphic Subunit Ia (0–21.76 m CSF-A) from the underlying lithified limestone of Lithostratigraphic Subunit Ib (Hole U1582A = 31.00–40.92 m CSF-A) and from the deeper pillow basalts with interspersed pockets of limestone in Lithostratigraphic Unit II (Hole U1582B = 36.83–53.73 m CSF-A) (Figure **F13**). Lithostratigraphic Subunit Ia contains unlithified sediment with high porosity (65–82 vol%), low MAD bulk density (1.40–1.62 g/cm^3), low PWC *P*-wave velocities (~1600 m/s), and low thermal conductivity (0.9–1.2 W/[m·K]). In comparison, the underlying more lithified limestones of Lithostratigraphic Subunit Ib have much lower porosity (~25%), higher average PWC *P*-wave velocity (~3000 m/s), and higher bulk density (~2.33 g/cm^3). The dark colored pillow basalts (L* = ~20–40) of Lithostratigraphic Unit II have higher NGR values (~20 counts/s) and higher MS (~500–1000 IU) than the light-colored basalt (Figure **F13**).

5. Preliminary scientific assessment

Expedition 392 recovered sedimentary sequences and igneous rocks at three sites on the Agulhas Plateau (Sites U1579, U1580, and U1582) and a sedimentary sequence from one site in the Transkei Basin (Site U1581) (Figures **F3**, **F14**, **F15**). The main sedimentary sections recovered at the Agulhas Plateau sites span the lowermost Miocene through uppermost Cenomanian and comprise a wide range of lithologies from nannofossil oozes/chalks to zeolitic sandstones (Figures **F14**, **F16**). Several key stratigraphic intervals that were well recovered at the Agulhas Plateau sites include the Oligocene–Miocene transition and a nearly complete spliced Oligocene sequence at Site U1579, the EOT at Site U1579, the Paleocene/Eocene boundary at Site U1580 (double cored), the K/Pg boundary at Sites U1579 and U1580, and the upper Campanian at Sites U1579 and U1580 (Figure **F15**). The thick sedimentary sequence cored in the Transkei Basin at Site U1581

also contains several important stratigraphic intervals, including an expanded Campanian claystone sequence and, potentially, the K/Pg boundary (requiring further stratigraphic analysis postcruise) (Figures **F14**, **F15**).

Igneous rocks cored at Sites U1579 and U1580 are classified as plagioclase-clinopyroxene phyric basalts, aphyric or slightly plagioclase basalts, and olivine phyric basalts. At both sites, the basalt units are interbedded with sedimentary units (Figure **F14**). The intercalation of igneous bodies and sediment packages implies that these units represent either lateral intrusions (sills) or that they were emplaced as lava flows on which sediments were deposited after each eruption. Based on several lines of evidence, the igneous successions at these sites are tentatively interpreted as sills. Preliminary geochemical analysis of the recovered basalts from both sites indicates that they have a tholeiitic composition, which is characteristic of the main plateau building phase of oceanic LIPs.

A sequence of plagioclase phyric pillow basalts was recovered at Site U1582, providing information on the eruptive nature of the Agulhas Plateau magmatism (Figure **F14**). The broadly constrained early Turonian–Santonian biostratigraphic age (~84–94 Ma) of the interpillow carbonate sediments may place these lavas several million years younger than the postulated formation age of the Agulhas Plateau based on seismic studies and plate tectonic reconstructions (95–105 Ma) (e.g., Gohl and Uenzelmann-Neben, 2001; Gohl et al., 2011). Direct radiometric dating of plagioclase phenocrysts of the Site U1582 basalts should be possible and will determine whether the reconstructions need to be revised or, alternatively, whether this pillow lava field belongs to a late

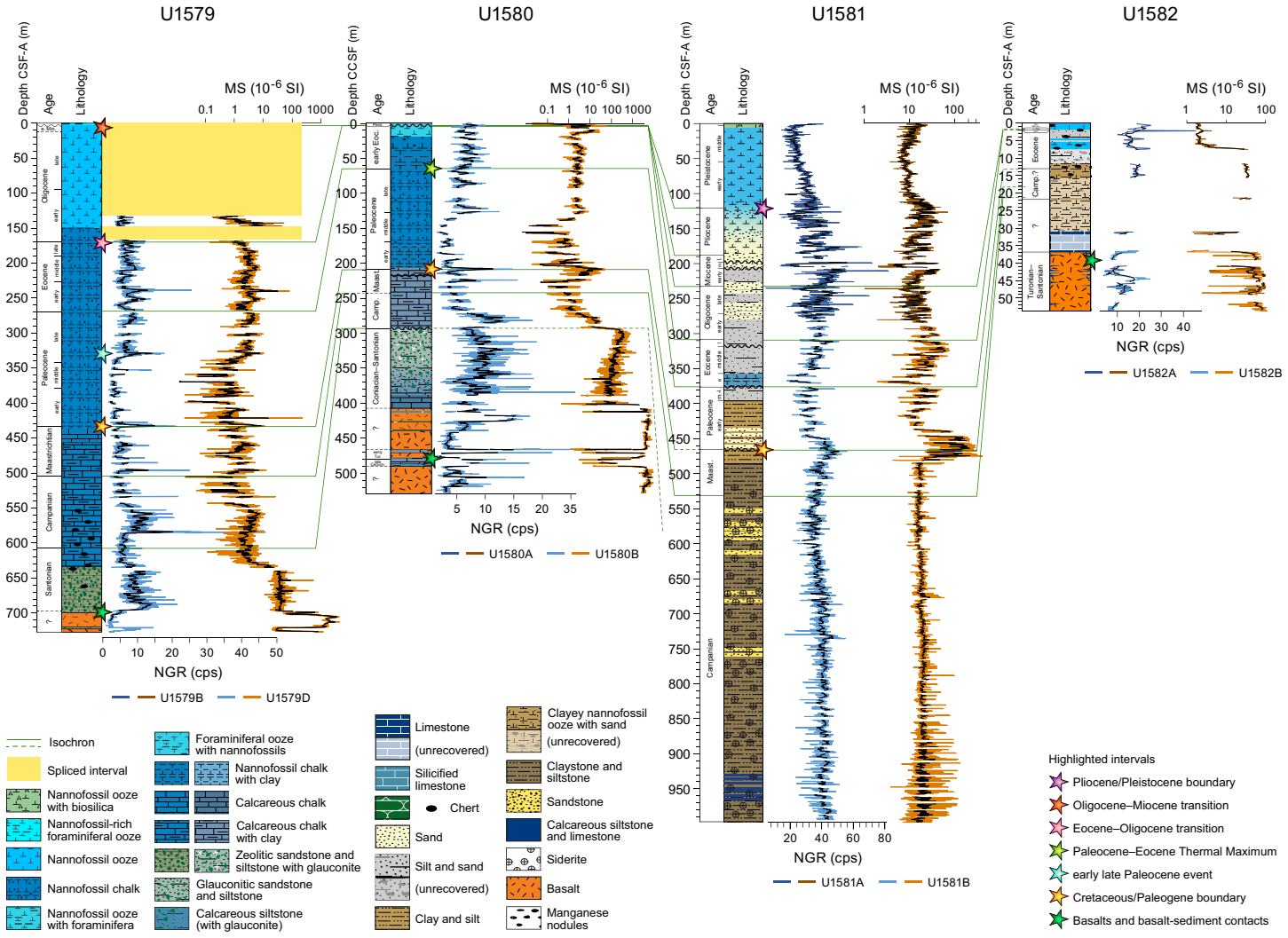

Figure F14. Lithologic summary with NGR and MS, Sites U1579–U1582. cps = counts per second.

rejuvenated or posterosional stage of volcanism. However, preliminary shipboard portable X-ray fluorescence spectrometry (pXRF) analyses indicate a tholeiitic composition for the Site U1582 pillow lavas, which may indicate that these basalts represent the main phase of Agulhas Plateau volcanism.

Unfavorable weather conditions during the last week of the expedition prevented the recovery of deep basement samples at Site U1582; instead of the intended 300 m CSF-A, we could only drill to ~50 m CSF-A. However, as has been outlined above, the recovered basement cores will allow dating pillow lava flows and thus bear huge potential to add to the reconstruction of the emplacement of the Agulhas Plateau. Geochemical and age comparison with material retrieved at Maud Rise during Ocean Drilling Program (ODP) Leg 113 and the Northeast Georgia Rise during ODP Leg 114 will further contribute to a better understanding of the development of this LIP obstructing the African–Southern Ocean gateway during the Late Cretaceous.

Drilling at Site U1581 revealed that an interpreted black shale reflector deep in the sedimentary sequence did not form the top of an organic-rich layer. However, the combination of recovered thin layers of siltstones, anisotropy observed for MS in the deepest cores recovered at Site U1581, peaks in *P*-wave velocity and density, and the computation of synthetic seismograms and thus core-log-seismic integration with dates from the sills recovered at Sites U1579 and U1580 will allow a study of the farfield effect that the emplacement of the Agulhas Plateau sills may have created.

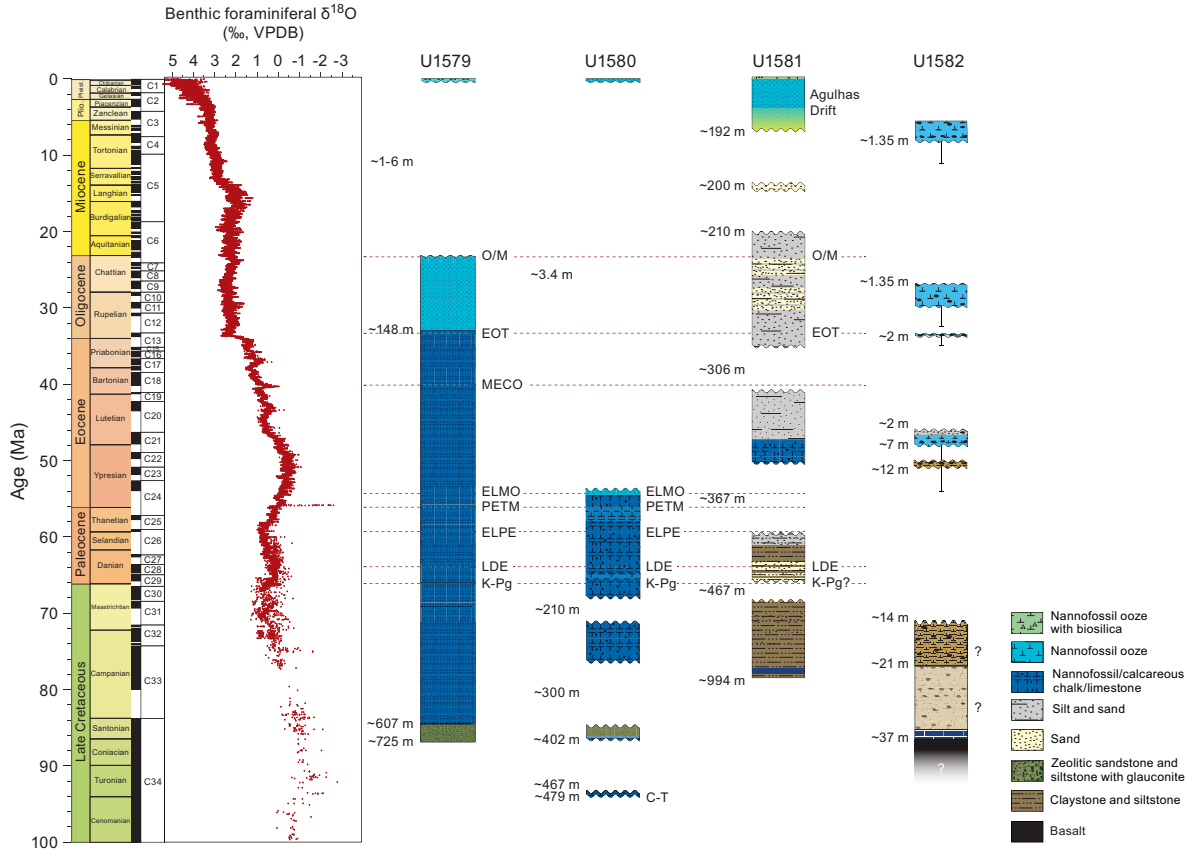

Figure F15. Lithostratigraphic overview of recovered sediments, Expedition 392. Benthic foraminiferal oxygen isotopes are compiled by combining CENOGRID of Westerhold et al. (2020) with the Cretaceous compilation of Huber et al. (2018). VPDB = Vienna Peedee belemnite. Sediments (excluding basalts from Sites U1579 and U1580) recovered at Sites U1579–U1582 are shown, each indicating hiatuses, indicators of stratigraphic depth of the sequence (on the CSF-A scale), and key climatic events and named sedimentary sequences. O/M = Oligocene/Miocene boundary, EOT = Eocene–Oligocene transition, MECO = Middle Eocene Climatic Optimum, ELMO = Eocene layer of mysterious origin, PETM = Paleocene/Eocene Thermal Maximum, ELPE = early late Paleocene hyperthermal event, LDE = Latest Danian Event, K/Pg = Cretaceous/Paleogene boundary, C-T = Cenomanian–Turonian interval.

In addition to these highlighted examples, the cores, downhole logging data, and IW samples collected at Expedition 392 sites will allow most of the main expedition objectives to be addressed. These objectives broadly fall into three areas: (1) age, origin, and evolution of the Agulhas Plateau, (2) paleoceanographic and climate history, and (3) rock-water interactions and chemical evolution of the Agulhas Plateau. The objectives of Expedition 392 also directly address the critical questions posed by the 2050 Science Framework Strategic Objectives:

- Earth's climate system: unraveling ice sheet history, sea level changes, and ocean-atmosphere interactions;
- Feedbacks in the Earth system: constraining the processes that regulate or destabilize the Earth system;
- The oceanic life cycle of tectonic plates: investigating the genesis, aging, motion, and destruction of oceanic plates; and
- Global cycles of energy and matter: determining the role, mechanisms, and magnitude of Earth system cycles.

Key aspects and research questions that will be pursued in postcruise studies are briefly outlined below.

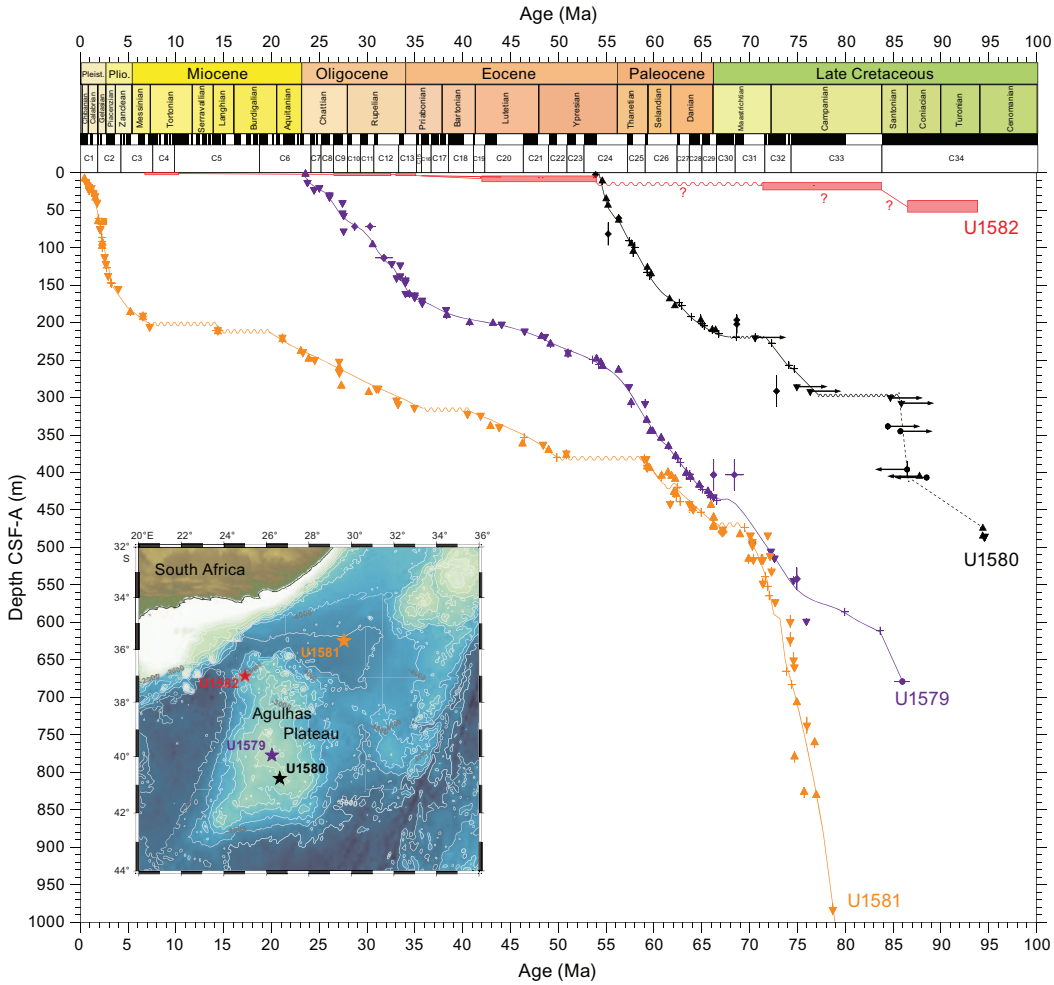

Figure F16. Age-depth plots, Expedition 392. The four sedimentary sequences recovered at the Agulhas Plateau and Transkei Basin are shown. Ages according to the GTS2020 (Gradstein et al., 2020). Insert map modified from Figure F3. Upward triangle = nannofossil base, downward triangle = nannofossil top, diamond = foraminiferal datum, circle = dinocyst datum, plus sign = magnetic polarity reversal, vertical line = datum depth uncertainty, horizontal line = age uncertainty, horizontal arrow = sediment could be younger (left arrow) or older (right arrow) than the position of the datum, wavy line = unconformity, pale red box = assemblage based age ranges for Site U1582, question mark = uncertainty.

5.1. Age, origin, and evolution of the Agulhas Plateau

- The successful recovery of igneous rocks at Sites U1579, U1580, and U1582 containing fresh plagioclase suitable for $^{40}Ar/^{39}Ar$ dating should yield reliable ages, thereby answering fundamental questions regarding the emplacement age of the Agulhas Plateau.
- The timing of the potential sill intrusions at Site U1580 will be particularly informative, both for understanding the temporal window in which magmatism occurred on the Agulhas Plateau and, potentially, also for identifying regional, or even global, impacts of LIP volcanism on circulation and climate in the Late Cretaceous.
- Radiometric dating (U/Pb) of the calcite veins in basalts will yield additional age constraints documenting the postemplacement alteration history of the Agulhas Plateau igneous units recovered at Sites U1579, U1580, and U1582.
- Radiogenic (e.g., Sr, Nd, Hf, Pb, and Os) and stable (e.g., O on fresh glass and mineral phases) isotope ratios from igneous rocks recovered at Sites U1579, U1580, and U1582 will allow characterization of the magma source composition and comparison with other regional or global LIPs.
- Abundant occurrence of fresh clinopyroxene and some chromium-rich spinel in the igneous material from Sites U1579, U1580, and U1582 will allow for the reconstruction of the primitive melt (including volatile) compositions from melt inclusions (e.g., in olivine, spinel, or pyroxene) to evaluate melting processes and extents, temperatures and depths. These planned investigations will enable evaluation of whether a mantle plume drove Agulhas Plateau magmatism.
- At Site U1582, combined petrological and trace element data on whole rocks and in particular on fresh glass (representing the melt composition) can be used to constrain the magma source temperature and degrees and depths of melting (e.g., Fitton et al., 2004; Herzberg et al., 2007; Husen et al., 2013; Putirka, 2008), crucial for distinguishing LIP formation models. Additionally, the analysis of CO_2 and other volatile gases in fresh glass from the basalt recovered at Site U1582 will provide information on the paleoenvironment during emplacement of the magmatic material.
- Benthic foraminiferal assemblages and organic-walled microfossils (miospores) at Sites U1579 and U1580 will provide insight into the paleobathymetric evolution of the Agulhas Plateau and, importantly, allow testing of whether areas of the central and southern Agulhas Plateau was subaerially exposed during its early stages of formation.
- The recovery for the first time of Upper Cretaceous igneous and sedimentary sequences from the Agulhas Plateau provides an opportunity to revise and complement existing plate kinematic reconstructions of the early Southern Ocean and the relative motion of Africa. Paleolatitudinal constraints derived from paleomagnetic and geochronologic analyses will improve our understanding of the formation of evolving gateways and the role of the Agulhas Plateau as a volcanotectonic barrier in the context of Gondwana breakup. Although the Agulhas Plateau is thought to have formed at 65°–58°S during the mid-Cretaceous (100–95 Ma), there is significant uncertainty in the timing and position (latitude) of emplacement because of the current lack of data.

5.2. Paleoceanographic and climate history

- The recovery at Site U1579 of rhythmically bedded limestone and claystones with striking white and red alternations, coupled with a good magnetostratigraphic record and nannofossil biostratigraphy, will reveal the pacing of Campanian climate by orbital forcing and also contribute to timescale development for this understudied interval of the Cretaceous.
- An expanded Campanian mudstone succession recovered at Site U1581 (Figures **F14**, **F15**, **F16**) will permit reconstruction of ocean and climate conditions adjacent to the Agulhas Plateau during the Late Cretaceous and Paleocene using organic-walled microfossils and terrestrial and marine organic biomarkers, providing information on ocean connectivity between the Atlantic and Indian through the Southern Ocean, as well as terrestrial climate history.
- The excellent preservation of nannofossils in the Campanian section at Site U1581 will provide an unprecedented opportunity to examine coccolithophore evolution over this time interval. Initial shipboard investigation revealed an intriguing combination of southern high-latitude and mid-latitude assemblages present at the site.

- The good recovery of the K/Pg boundary interval at Sites U1579 and U1580 will provide new materials for high-resolution investigations of the boundary event (Figures **F14**, **F15**, **F16**). Because the Agulhas Plateau was located in relative proximity to the Deccan Traps (western India) at the end of the Cretaceous, detailed study of the new sequences recovered during Expedition 392 should allow for examination of the timing and effects of Deccan volcanism in the context of the boundary impact event.
- The expanded Late Cretaceous and early Paleogene sedimentary sequences recovered at Sites U1579–U1581 contain abundant calcareous microfossils, which will provide a good basis for calcareous nannofossil and foraminiferal paleoecological studies and improvement of biostratigraphic frameworks for the southern high latitudes.
- The abundant occurrence and good preservation state of foraminifera in the Miocene–Maastrichtian sequences and inoceramids (bivalves) in the Campanian sequences will additionally provide potential for conventional oxygen and carbon isotope analysis, as well as clumped isotope analysis, for reconstruction of paleotemperature over both long and short timescales through the Cretaceous and Paleogene.
- Two nearly complete Paleocene records were recovered at Sites U1579 and U1580 and will provide an excellent opportunity to study that time interval in the Southern Hemisphere where many records have unconformities or low carbonate content (Figures **F14**, **F15**, **F16**). These new materials recovered during Expedition 392 will be particularly ideal for examining plankton evolution following the K/Pg mass extinction.
- A Paleocene/Eocene boundary section was recovered at Site U1580 at relatively shallow subseafloor depths (~60 m) in two parallel holes (Figures **F14**, **F15**, **F16**). In contrast to most deep-sea records, Site U1580 sediments remain carbonate rich across the boundary, without a clay layer that typically results from carbonate dissolution during the PETM. The minimal carbonate dissolution at Site U1580 places a new constraint on the degree of carbonate compensation depth shoaling during the PETM, and also presents a unique opportunity to study the morphology, ecology, and geochemistry of planktonic and benthic foraminifera during the event. Foraminifera-based stable isotope investigations at Site U1580 may reveal an exceptionally complete record, particularly of the earliest phases of the event's onset, which is typically truncated by carbonate dissolution at other well-studied sites.
- Results from preliminary rock magnetic experiments performed on discrete sediment samples collected from Expedition 392 highlight distinct variations in magnetic mineralogy at Sites U1579 and U1580, with some variations correlating with observed changes in IW geochemistry, and others with major environmental crises (e.g., K/Pg and Eocene hyperthermal events). These results suggest that magnetic mineralogy can be used as an environmental proxy to highlight changes in diagenesis, redox conditions, and paleoclimate throughout the sampled sedimentary packages.
- Paleogene sediments from Sites U1579 and U1580 are suitable for Nd isotope analyses of fish teeth and debris, which will allow fingerprinting of deepwater masses and tracing their pathways as oceanic gateways opened in the Cretaceous and Paleogene.
- A nearly complete Oligocene record extending through the Oligocene–Miocene transition was recovered at Site U1579 (Figures **F14**, **F15**, **F16**). The location of Site U1579 is well situated to examine circulation changes that occurred in conjunction with establishment of large ice sheets on Antarctica at the EOT and also the gradual initiation of the ACC through the Oligocene and Miocene. Calcareous microfossil paleoecological analysis and geochemical proxy analysis, and potentially organic biomarker analysis, will enable examination of temperature and upper water column hydrographic changes through this time interval, both from the perspective of long-term trends and orbitally paced variability. These new records from the Agulhas Plateau are also particularly well situated to shed light on the timing and regional impact of the pre-Neogene development of the Agulhas Current.
- Excellent physical properties data (natural gamma ray, density, seismic velocity, resistivity, porosity, MS, FMS, and UBI) collected both from the cores and downhole at Sites U1579 and U1580 will allow for successful core-log-seismic integration. In the absence of downhole logging data at Sites U1581 and U1582 (because of technical problems and bad weather), the physical properties data collected from the cores will be used for this purpose. Synthetic seismograms will allow the transfer of geological information to seismic data and thus the spatial extrapolation of this information. Ages and origins will be assigned to prominent

reflections. Hiatuses and condensed sections can be characterized in three dimensions, and the seismostratigraphic models for the Agulhas Plateau and Transkei Basin will be revised. Pathways of paleocurrents will be reconstructed with the potential to form the starting point for numerical simulation of sediment transport (e.g., in combination with grain size information).
- Core-log integration of exceptional natural gamma records obtained from the Paleocene and Eocene sections drilled at Sites U1579 and U1580 will also facilitate correlation to high-resolution stratigraphic records from Shatsky Rise (North Pacific, ODP Leg 198) and Walvis Ridge (South Atlantic, ODP Leg 208). Detailed intra and interbasin correlation will improve the stratigraphic framework for Expedition 392 cores and allow placement of the regional Agulhas Plateau paleoceanographic records into a global context.

5.3. Rock-water interactions and chemical evolution

- In addition to radiometric dating of the potential sill intrusions at Sites U1579 and U1580, postcruise investigations will focus on how volcanic intrusions have altered the organic-rich sediments these sills have penetrated through and the consequences of the magma-sediment interactions.
- The sediments and IW from the Agulhas Plateau Sites U1579 and U1580 provide an excellent opportunity to investigate submarine (reverse) weathering of LIP basalts and authigenic mineral formation in sediments in contact with igneous sills to assess impacts on seawater chemistry and long-term carbon cycling.

5.4. Additional research directions

- At Site U1581 in the Transkei Basin, Pliocene–Pleistocene sediments of the Agulhas Drift were well recovered and characterized by interbedded pelagic oozes and distal turbidites (Figures **F14**, **F15**). This sequence will allow for correlation to detailed seismic stratigraphy, as well as investigation of sediment provenance via comparison with onshore deposits and interpretation of sedimentary processes.
- The Pliocene–Pleistocene sequence recovered at Site U1581 also contains a good record of siliceous microfossils. Postcruise analysis of diatom accumulation and assemblage composition will allow assessment of the strength and extent of Antarctic Bottom Water flow through the Agulhas Passage during the mid-Pleistocene transition.

References

Agnini, C., Fornaciari, E., Raffi, I., Catanzariti, R., Pälike, H., Backman, J., and Rio, D., 2014. Biozonation and biochronology of Paleogene calcareous nannofossils from low and middle latitudes. Newsletters on Stratigraphy, 47(2):131–181. **https://doi.org/10.1127/0078-0421/2014/0042**

Allen, R.B., and Tucholke, B.E., 1981. Petrography and implications of continental rocks from the Agulhas Plateau, southwest Indian Ocean. Geology, 9(10):463–468. **https://doi.org/10.1130/0091-7613(1981)9<463:PAIOCR>2.0.CO;2**

Andò, A., Woodard, S.C., Evans, H.F., Littler, K., Herrmann, S., Macleod, K.G., Kim, S., Khim, B.K., Robinson, S.A., and Huber, B.T., 2013. An emerging palaeoceanographic 'missing link': multidisciplinary study of rarely recovered parts of deep-sea Santonian-Campanian transition from Shatsky Rise. Journal of the Geological Society (London, UK), 170(3):381–384. **https://doi.org/10.1144/jgs2012-137**

Arthur, M.A., Dean, W.E., and Schlanger, S.O., 1985. Variations in the global carbon cycle during the Cretaceous related to climate, volcanism, and changes in atmospheric CO_2. In Sundquist, E.T., and Broecker, W.S. (Eds.), The Carbon Cycle and Atmospheric CO_2: Natural Variations Archean to Present. Geophysical Monograph: 504–529. **https://doi.org/10.1029/GM032p0504**

Arthur, M.A., Schlanger, S.O., and Jenkyns, H.C., 1987. The Cenomanian-Turonian Oceanic Anoxic Event, II. Palaeoceanographic controls on organic-matter production and preservation. In Brooks, J., and Fleet, A.J. (Eds.), Marine Petroleum Source Rocks. Geological Society Special Publication, 26:401–420. **https://doi.org/10.1144/GSL.SP.1987.026.01.25**

Beerling, D.J., and Royer, D.L., 2011. Convergent Cenozoic CO_2 history. Nature Geoscience, 4(7):418–420. **https://doi.org/10.1038/ngeo1186**

Berner, R.A., Lasaga, A.C., and Garrels, R.M., 1983. The carbonate-silicate geochemical cycle and its effect on atmospheric carbon dioxide over the past 100 million years. American Journal of Science, 283(7):641–683. **https://doi.org/10.2475/ajs.283.7.641**

Biastoch, A., Böning, C.W., and Lutjeharms, J.R.E., 2008. Agulhas leakage dynamics affects decadal variability in Atlantic overturning circulation. Nature, 456(7221):489–492. **https://doi.org/10.1038/nature07426**

Biastoch, A., Böning, C.W., Scheinert, M., and Lutjeharms, J.R.E., 2009. The Agulhas system as a key region of the global oceanic circulation. In Nagel, W.E., Kröner, D.B., and Resch, M.M. (Eds.), High Performance Computing in Science and Engineering '08. Nagel, W.E., Kröner, D.B. and Resch, M.M.: Heidelberg (Springer), 459–469. **https://doi.org/10.1007/978-3-540-88303-6_32**

Bice, K.L., Birgel, D., Meyers, P.A., Dahl, K.A., Hinrichs, K.-U., and Norris, R.D., 2006. A multiple proxy and model study of Cretaceous upper ocean temperatures and atmospheric CO_2 concentrations. Paleoceanography and Paleoclimatology, 21(2):PA2002. **https://doi.org/10.1029/2005PA001203**

Bice, K.L., Huber, B.T., and Norris, R.D., 2003. Extreme polar warmth during the Cretaceous greenhouse? Paradox of the late Turonian $\delta^{18}O$ record at Deep Sea Drilling Project Site 511. Paleoceanography and Paleoclimatology, 18(2):1031. **https://doi.org/10.1029/2002PA000848**

Bohaty, S.M., Uenzelmann-Neben, G., Childress, L.B., Archontikis, O.A., Batenburg, S.J., Bijl, P.K., Burkett, A.M., Cawthra, H.C., Chanda, P., Coenen, J.J., Dallanave, E., Davidson, P.C., Doiron, K.E., Geldmacher, J., Gürer, D., Haynes, S.J., Herrle, J.O., Ichiyama, Y., Jana, D., Jones, M.M., Kato, C., Kulhanek, D.K., Li, J., Liu, J., McManus, J., Minakov, A.N., Penman, D.E., Sprain, C.J., Tessin, A.C., Wagner, T., and Westerhold, T., 2023a. Site U1579. In Uenzelmann-Neben, G., Bohaty, S.M., Childress, L.B., and the Expedition 392 Scientists, Agulhas Plateau Cretaceous Climate. Proceedings of the International Ocean Discovery Program, 392: College Station, TX (International Ocean Discovery Program). **https://doi.org/10.14379/iodp.proc.392.103.2023**

Bohaty, S.M., Uenzelmann-Neben, G., Childress, L.B., Archontikis, O.A., Batenburg, S.J., Bijl, P.K., Burkett, A.M., Cawthra, H.C., Chanda, P., Coenen, J.J., Dallanave, E., Davidson, P.C., Doiron, K.E., Geldmacher, J., Gürer, D., Haynes, S.J., Herrle, J.O., Ichiyama, Y., Jana, D., Jones, M.M., Kato, C., Kulhanek, D.K., Li, J., Liu, J., McManus, J., Minakov, A.N., Penman, D.E., Sprain, C.J., Tessin, A.C., Wagner, T., and Westerhold, T., 2023b. Site U1580. In Uenzelmann-Neben, G., Bohaty, S.M., Childress, L.B., and the Expedition 392 Scientists, Agulhas Plateau Cretaceous Climate. Proceedings of the International Ocean Discovery Program, 392: College Station, TX (International Ocean Discovery Program). **https://doi.org/10.14379/iodp.proc.392.104.2023**

Bohaty, S.M., Uenzelmann-Neben, G., Childress, L.B., Archontikis, O.A., Batenburg, S.J., Bijl, P.K., Burkett, A.M., Cawthra, H.C., Chanda, P., Coenen, J.J., Dallanave, E., Davidson, P.C., Doiron, K.E., Geldmacher, J., Gürer, D., Haynes, S.J., Herrle, J.O., Ichiyama, Y., Jana, D., Jones, M.M., Kato, C., Kulhanek, D.K., Li, J., Liu, J., McManus, J., Minakov, A.N., Penman, D.E., Sprain, C.J., Tessin, A.C., Wagner, T., and Westerhold, T., 2023c. Site U1581. In Uenzelmann-Neben, G., Bohaty, S.M., Childress, L.B., and the Expedition 392 Scientists, Agulhas Plateau Cretaceous Climate. Proceedings of the International Ocean Discovery Program, 392: College Station, TX (International Ocean Discovery Program). **https://doi.org/10.14379/iodp.proc.392.105.2023**

Bohaty, S.M., Uenzelmann-Neben, G., Childress, L.B., Archontikis, O.A., Batenburg, S.J., Bijl, P.K., Burkett, A.M., Cawthra, H.C., Chanda, P., Coenen, J.J., Dallanave, E., Davidson, P.C., Doiron, K.E., Geldmacher, J., Gürer, D., Haynes, S.J., Herrle, J.O., Ichiyama, Y., Jana, D., Jones, M.M., Kato, C., Kulhanek, D.K., Li, J., Liu, J., McManus, J., Minakov, A.N., Penman, D.E., Sprain, C.J., Tessin, A.C., Wagner, T., and Westerhold, T., 2023d. Site U1582. In Uenzelmann-Neben, G., Bohaty, S.M., Childress, L.B., and the Expedition 392 Scientists, Agulhas Plateau Cretaceous Climate. Proceedings of the International Ocean Discovery Program, 392: College Station, TX (International Ocean Discovery Program). **https://doi.org/10.14379/iodp.proc.392.106.2023**

Bryan, S.E., and Ernst, R.E., 2008. Revised definition of Large Igneous Provinces (LIPs). Earth-Science Reviews, 86(1–4):175–202. **https://doi.org/10.1016/j.earscirev.2007.08.008**

Bullard, E.C., 1954. The flow of heat through the floor of the Atlantic Ocean. Proceedings of the Royal Society of London, A: Mathematical and Physical Sciences, 222(1150):408–429. **https://doi.org/10.1098/rspa.1954.0085**

Charvis, P., Recq, M., Operto, S., and Brefort, D., 1995. Deep structure of the northern Kerguelen Plateau and hotspot-related activity. Geophysical Journal International, 122(3):899–924. **https://doi.org/10.1111/j.1365-246X.1995.tb06845.x**

Chen, H., Xu, Z., Bayon, G., Lim, D., Batenburg, S.J., Petrizzo, M.R., Hasegawa, T., and Li, T., 2022. Enhanced hydrological cycle during Oceanic Anoxic Event 2 at southern high latitudes: new insights from IODP Site U1516. Global and Planetary Change, 209:103735. **https://doi.org/10.1016/j.gloplacha.2022.103735**

Clarke, L.J., and Jenkyns, H.C., 1999. New oxygen isotope evidence for long-term Cretaceous climatic change in the Southern Hemisphere. Geology, 27(8):699–702. **https://doi.org/10.1130/0091-7613(1999)027%3C0699:NOIEFL%3E2.3.CO;2**

Davy, B., Hoernle, K., and Werner, R., 2008. Hikurangi Plateau: Crustal structure, rifted formation, and Gondwana subduction history. Geochemistry, Geophysics, Geosystems, 9(7):007004. **https://doi.org/10.1029/2007GC001855**

de Ruijter, W.P.M., Biastoch, A., Drijfhout, S.S., Lutjeharms, J.R.E., Matano, R.P., Pichevin, T., van Leeuwen, P.J., and Weijer, W., 1999. Indian-Atlantic interocean exchange: dynamics, estimation and impact. Journal of Geophysical Research: Oceans, 104(C9):20885–20910. **https://doi.org/10.1029/1998JC900099**

de Ruijter, W.P.M., Brummer, G.-J.A., Drijfhout, S.S., Lutjeharms, J.R.E., Peters, F., Ridderinkhof, H., van Aken, H., and van Leeuwen, P.J., 2006. Observations of the inter-ocean exchange around South Africa. Eos, Transactions of the American Geophysical Union, 87(9):97–101. **https://doi.org/10.1029/2006EO090002**

DeConto, R.M., and Pollard, D., 2003. Rapid Cenozoic glaciation of Antarctica induced by declining atmospheric CO_2. Nature, 421(6920):245–249. **https://doi.org/10.1038/nature01290**

Expedition 324 Scientists, 2010. Expedition 324 summary. In Sager, W.W., Sano, T., Geldmacher, J., and the Expedition 324 Scientists, Proceedings of the Integrated Ocean Drilling Program. 324: Tokyo (Integrated Ocean Drilling Program Management International, Inc.). **https://doi.org/10.2204/iodp.proc.324.101.2010**

Fischer, M.D., 2017. The Mozambique Ridge: evolution of a Large Igneous Province and its implication for paleocean circulation [PhD dissertation]. University of Bremen, Bremen, Germany. **https://epic.awi.de/id/eprint/45674/1/Dissertation_M_D_Fischer.pdf**

Fischer, M.D., and Uenzelmann-Neben, G., 2018. Late Cretaceous onset of current controlled sedimentation in the African–Southern Ocean gateway. Marine Geology, 395:380–396. **https://doi.org/10.1016/j.margeo.2017.11.017**

Fischer, M.D., Uenzelmann-Neben, G., Jacques, G., and Werner, R., 2016. The Mozambique Ridge: a document of massive multistage magmatism. Geophysical Journal International, 208(1):449–467. **https://doi.org/10.1093/gji/ggw403**

Fitton, J.G., Mahoney, J.J., Wallace, P.J., and Saunders, A.D., 2004. Leg 192 synthesis: origin and evolution of the Ontong Java Plateau. In Fitton, J.G., Mahoney, J.J., Wallace, P.J., and Saunders, A.D. (Eds.), Proceedings of the Ocean Drilling Program, Scientific Results. 192: College Station, TX (Ocean Drilling Program). **https://doi.org/10.2973/odp.proc.sr.192.101.2004**

Forster, A., Schouten, S., Moriya, K., Wilson, P.A., and Sinninghe Damsté, J.S., 2007. Tropical warming and intermittent cooling during the Cenomanian/Turonian Oceanic Anoxic Event 2: sea surface temperature records from the equatorial Atlantic. Paleoceanography and Paleoclimatology, 22(1):PA1219. **https://doi.org/10.1029/2006PA001349**

Frank, M., Reynolds, B.C., and Keith O'Nions, R., 1999. Nd and Pb isotopes in Atlantic and Pacific water masses before and after closure of the Panama gateway. Geology, 27(12):1147–1150. **https://doi.org/10.1130/0091-7613(1999)027<1147:NAPIIA>2.3.CO;2**

Frank, T.D., and Arthur, M.A., 1999. Tectonic forcings of Maastrichtian ocean-climate evolution. Paleoceanography and Paleoclimatology, 14(2):103–117. **https://doi.org/10.1029/1998PA900017**

Friedrich, O., Norris, R.D., Bornemann, A., Beckmann, B., Pälike, H., Worstell, P., Hofmann, P., and Wagner, T., 2008. Cyclic changes in Turonian to Coniacian planktic foraminiferal assemblages from the tropical Atlantic Ocean. Marine Micropaleontology, 68(3):299–313. **https://doi.org/10.1016/j.marmicro.2008.06.003**

Friedrich, O., Norris, R.D., and Erbacher, J., 2012. Evolution of middle to Late Cretaceous oceans—a 55 m.y. record of Earth's temperature and carbon cycle. Geology, 40(2):107–110. **https://doi.org/10.1130/G32701.1**

Geldmacher, J., van den Bogaard, P., Heydolph, K., and Hoernle, K., 2014. The age of Earth's largest volcano; Tamu Massif on Shatsky Rise (northwest Pacific Ocean). International Journal of Earth Sciences, 103(8):2351–2357. **https://doi.org/10.1007/s00531-014-1078-6**

Georgen, J.E., Lin, J., and Dick, H.J.B., 2001. Evidence from gravity anomalies for interactions of the Marion and Bouvet hotspots with the Southwest Indian Ridge: effects of transform offsets. Earth and Planetary Science Letters, 187(3):283–300. **https://doi.org/10.1016/S0012-821X(01)00293-X**

Gohl, K., Eagles, G., Netzeband, G., Grobys, J.W.G., Parsiegla, N., Schlüter, P., Leinweber, V., Larter, R.D., Uenzelmann-Neben, G., and Udintsev, G.B., 2007. Geophysical survey reveals tectonic structures in the Amundsen Sea embayment, West Antarctica. In Cooper, A., Raymond, C., and the ISAES Editorial Team (Eds.), Antarctica: a keystone in a changing world. Survey, U.S.G. USGS Open-File Report, 2007-1047-SRP-047. **https://doi.org/10.3133/ofr20071047SRP047**

Gohl, K., and Uenzelmann-Neben, G., 2001. The crustal role of the Agulhas Plateau, southwest Indian Ocean: evidence from seismic profiling. Geophysical Journal International, 144(3):632–646. **https://doi.org/10.1046/j.1365-246x.2001.01368.x**

Gohl, K., Uenzelmann-Neben, G., and Grobys, N., 2011. Growth and dispersal of a Southeastern African Large Igneous Province. South African Journal of Geology, 114(3–4):379–386. **https://doi.org/10.2113/gssajg.114.3-4.379**

Gradstein, F.M., Ogg, J.G., Schmitz, M.D., and Ogg, G.M. (Eds.), 2020. The Geologic Time Scale 2020: Amsterdam (Elsevier BV). **https://doi.org/10.1016/C2020-1-02369-3**

Gruetzner, J., Jiménez Espejo, F.J., Lathika, N., Uenzelmann-Neben, G., Hall, I.R., Hemming, S.R., LeVay, L.J., and the Expedition 361 Scientists, 2019. A new seismic stratigraphy in the Indian-Atlantic Ocean gateway resembles major paleo-oceanographic changes of the last 7 Ma. Geochemistry, Geophysics, Geosystems, 20(1):339–358. **https://doi.org/10.1029/2018GC007668**

Hall, I.R., Hemming, S.R., LeVay, L.J., Barker, S.R., Berke, M.A., Brentegani, L., Caley, T., Cartagena-Sierra, A., Charles, C.D., Coenen, J.J., Crespin, J.G., Franzese, A.M., Gruetzner, J., Xibin, H., Hines, S.K.V., Jimenez Espejo, F.J., Just, J., Koutsodendris, A., Kubota, K., Lathika, N., Norris, R.D., Pereira dos Santos, T., Robinson, R., Rolison, J.M., Simon, M.H., Tangunan, D., van der Lubbe, J.J.L., Yamane, M., and Hucai, Z., 2017. Expedition 361 summary. In Hall, I.R., Hemming, S.R., LeVay, L.J., and the Expedition 361 Scientists, South African Climates (Agulhas LGM Density Profile). Proceedings of the International Ocean Discovery Program, 361: College Station, TX (International Ocean Discovery Program). **https://doi.org/10.14379/iodp.proc.361.101.2017**

Hanan, B.B., Blichert-Toft, J., Pyle, D.G., and Christie, D.M., 2004. Contrasting origins of the upper mantle revealed by hafnium and lead isotopes from the Southeast Indian Ridge. Nature, 432(7013):91–94. **https://doi.org/10.1038/nature03026**

Hay, W.W., DeConto, R.M., Wold, C.N., Wilson, K.M., Voigt, S., Schulz, M., Wold, A.R., Dullo, W.-C., Ronov, A.B., Balukhovsky, A.N., Söding, E., Barrera, E., and Johnson, C.C., 1999. Alternative global Cretaceous paleogeography. In Barrera, E., and Johnson, C.C. (Eds.), Evolution of the Cretaceous Ocean-Climate System. Special Paper - Geological Society of America 332. **https://doi.org/10.1130/0-8137-2332-9.1**

Herzberg, C., Asimow, P.D., Arndt, N., Niu, Y., Lesher, C.M., Fitton, J.G., Cheadle, M.J., and Saunders, A.D., 2007. Temperatures in ambient mantle and plumes: constraints from basalts, picrites, and komatiites. Geochemistry, Geophysics, Geosystems, 8(2):Q02006. **https://doi.org/10.1029/2006GC001390**

Heydolph, K., Murphy, D.T., Geldmacher, J., Romanova, I.V., Greene, A., Hoernle, K., Weis, D., and Mahoney, J., 2014. Plume versus plate origin for the Shatsky Rise oceanic plateau (NW Pacific): insights from Nd, Pb and Hf isotopes. Lithos, 200–201:49–63. **https://doi.org/10.1016/j.lithos.2014.03.031**

Hoernle, K., Hauff, F., van den Bogaard, P., Werner, R., Mortimer, N., Geldmacher, J., Garbe-Schönberg, D., and Davy, B., 2010. Age and geochemistry of volcanic rocks from the Hikurangi and Manihiki oceanic plateaus. Geochimica et Cosmochimica Acta, 74(24):7196–7219. **https://doi.org/10.1016/j.gca.2010.09.030**

Huber, B.T., Hobbs, R.W., Bogus, K.A., Batenburg, S.J., Brumsack, H.-J., do Monte Guerra, R., Edgar, K.M., Edvardsen, T., Garcia Tejada, M.L., Harry, D.L., Hasegawa, T., Haynes, S.J., Jiang, T., Jones, M.M., Kuroda, J., Lee, E.Y., Li, Y.-X., MacLeod, K.G., Maritati, A., Martinez, M., O'Connor, L.K., Petrizzo, M.R., Quan, T.M., Richter, C., Riquier, L., Tagliaro, G.T., Wainman, C.C., Watkins, D.K., White, L.T., Wolfgring, E., and Xu, Z., 2019. Expedition 369 summary. In Hobbs, R.W., Huber, B.T., Bogus, K.A., and the Expedition 369 Scientists, Australia Cretaceous climate and tectonics. Proceedings of the International Ocean Discovery Program, 369: College Station, TX (International Ocean Discovery Program). **https://doi.org/10.14379/iodp.proc.369.101.2019**

Huber, B.T., Hodell, D.A., and Hamilton, C.P., 1995. Middle–Late Cretaceous climate of the southern high latitudes: Stable isotopic evidence for minimal equator-to-pole thermal gradients. Geological Society of America Bulletin, 107(10):1164–1191. **https://doi.org/10.1130/0016-7606(1995)107<1164:MLCCOT>2.3.CO;2**

Huber, B.T., MacLeod, K.G., Watkins, D.K., and Coffin, M.F., 2018. The rise and fall of the Cretaceous hot greenhouse climate. Global and Planetary Change, 167:1–23. **https://doi.org/10.1016/j.gloplacha.2018.04.004**

Huber, B.T., Norris, R.D., and MacLeod, K.G., 2002. Deep-sea paleotemperature record of extreme warmth during the Cretaceous. Geology, 30(2):123–126. **https://doi.org/10.1130/0091-7613(2002)030<0123:DSPROE>2.0.CO;2**

Husen, A., Almeev, R.R., Holtz, F., Koepke, J., Sano, T., and Mengel, K., 2013. Geothermobarometry of basaltic glasses from the Tamu Massif, Shatsky Rise oceanic plateau. Geochemistry, Geophysics, Geosystems, 14(10):3908–3928. **https://doi.org/10.1002/ggge.20231**

Intergovernmental Panel on Climate Change, 2022. Climate Change 2022: Impacts, Adaptation and Vulnerability: New York (Cambridge University Press).

Jackson, M.G., and Carlson, R.W., 2011. An ancient recipe for flood-basalt genesis. Nature, 476(7360):316–319. **https://doi.org/10.1038/nature10326**

Jackson, M.G., Carlson, R.W., Kurz, M.D., Kempton, P.D., Francis, D., and Blusztajn, J., 2010. Evidence for the survival of the oldest terrestrial mantle reservoir. Nature, 466(7308):853–856. **https://doi.org/10.1038/nature09287**

Jacques, G., Hauff, F., Hoernle, K., Werner, R., Uenzelmann-Neben, G., Garbe-Schönberg, D., and Fischer, M., 2019. Nature and origin of the Mozambique Ridge, SW Indian Ocean. Chemical Geology, 507:9–22. **https://doi.org/10.1016/j.chemgeo.2018.12.027**

Jenkyns, H.C., 2003. Evidence for rapid climate change in the Mesozoic–Palaeogene greenhouse world. Philosophical Transactions of the Royal Society, A: Mathematical, Physical and Engineering Sciences, 361(1810):1885–1916. **https://doi.org/10.1098/rsta.2003.1240**

Jenkyns, H.C., 2010. Geochemistry of oceanic anoxic events. Geochemistry, Geophysics, Geosystems, 11(3):Q03004. **https://doi.org/10.1029/2009GC002788**

Jung, C., Voigt, S., Friedrich, O., Koch, M.C., and Frank, M., 2013. Campanian-Maastrichtian ocean circulation in the tropical Pacific. Paleoceanography, 28(3):562–573. **https://doi.org/10.1002/palo.20051**

König, M., and Jokat, W., 2010. Advanced insights into magmatism and volcanism of the Mozambique Ridge and Mozambique Basin in the view of new potential field data. Geophysical Journal International, 180(1):158–180. **https://doi.org/10.1111/j.1365-246X.2009.04433.x**

Kump, L.R., and Pollard, D., 2008. Amplification of Cretaceous warmth by biological cloud feedbacks. Science, 320(5873):195. **https://doi.org/10.1126/science.1153883**

Lutjeharms, J.R.E., 1996. The exchange of water between the South Indian and South Atlantic Oceans. In Wefer, G., Berger, W.H., Siedler, G., and Webb, D.J. (Eds.), The South Atlantic: Present and Past Circulation. Berlin (Springer-Verlag), 125–162.

Lutjeharms, J.R.E., 2006. The Agulhas Current: Berlin (Springer-Verlag). **https://doi.org/10.1007/3-540-37212-1**

Lutjeharms, J.R.E., and Ansorge, I.J., 2001. The Agulhas Return Current. Journal of Marine Systems, 30(1–2):115–138. **https://doi.org/10.1016/S0924-7963(01)00041-0**

MacLeod, K.G., and Huber, B.T., 1996. Reorganization of deep ocean circulation accompanying a Late Cretaceous extinction event. Nature, 380(6573):422–425. **https://doi.org/10.1038/380422a0**

MacLeod, K.G., Isaza Londoño, C., Martin, E.E., Jiménez Berrocoso, Á., and Basak, C., 2011. Changes in North Atlantic circulation at the end of the Cretaceous greenhouse interval. Nature Geoscience, 4(11):779–782. **https://doi.org/10.1038/ngeo1284**

MacLeod, K.G., Martin, E.E., and Blair, S.W., 2008. Nd isotopic excursion across Cretaceous Ocean Anoxic Event 2 (Cenomanian-Turonian) in the tropical North Atlantic. Geology, 36(10):811–814. **https://doi.org/10.1130/G24999A.1**

Mantyla, A.W., and Reid, J.L., 1995. On the origins of deep and bottom waters of the Indian Ocean. Journal of Geophysical Research: Oceans, 100(C2):2417–2439. **https://doi.org/10.1029/94JC02564**

Marks, K.M., and Tikku, A.A., 2001. Cretaceous reconstructions of East Antarctica, Africa and Madagascar. Earth and Planetary Science Letters, 186(3–4):479–495. **https://doi.org/10.1016/S0012-821X(01)00262-X**

Martini, E., 1971. Standard Tertiary and Quaternary calcareous nannoplankton zonation. Proceedings of the Second Planktonic Conference, Roma, 1970:739–785.

Murphy, D.P., and Thomas, D.J., 2012. Cretaceous deep-water formation in the Indian sector of the Southern Ocean. Paleoceanography and Paleoclimatology, 27(1):PA1211. **https://doi.org/10.1029/2011PA002198**

Murphy, D.P., and Thomas, D.J., 2013. The evolution of Late Cretaceous deep-ocean circulation in the Atlantic basins: neodymium isotope evidence from South Atlantic drill sites for tectonic controls. Geochemistry, Geophysics, Geosystems, 14(12):5323–5340. **https://doi.org/10.1002/2013GC004889**

Niemi, T.M., Ben-Avraham, Z., Hartnady, C.J.H., and Reznikov, M., 2000. Post-Eocene seismic stratigraphy of the deep ocean basin adjacent to the southeast African continental margin: a record of geostrophic bottom current systems. Marine Geology, 162(2–4):237–258. **https://doi.org/10.1016/S0025-3227(99)00062-6**

O'Brien, C.L., Robinson, S.A., Pancost, R.D., Sinninghe Damsté, J.S., Schouten, S., Lunt, D.J., Alsenz, H., Bornemann, A., Bottini, C., Brassell, S.C., Farnsworth, A., Forster, A., Huber, B.T., Inglis, G.N., Jenkyns, H.C., Linnert, C., Littler,

K., Markwick, P., McAnena, A., Mutterlose, J., Naafs, B.D.A., Püttmann, W., Sluijs, A., van Helmond, N.A.G.M., Vellekoop, J., Wagner, T., and Wrobel, N.E., 2017. Cretaceous sea-surface temperature evolution: Constraints from TEX_{86} and planktonic foraminiferal oxygen isotopes. Earth-Science Reviews, 172:224–247. **https://doi.org/10.1016/j.earscirev.2017.07.012**

O'Connor, L.K., Robinson, S.A., Naafs, B.D.A., Jenkyns, H.C., Henson, S., Clarke, M., and Pancost, R.D., 2019. Late Cretaceous temperature evolution of the southern high latitudes: a TEX_{86} perspective. Paleoceanography and Paleoclimatology, 34(4):436–454. **https://doi.org/10.1029/2018PA003546**

Ogg, J.G., 2020. Geomagnetic Polarity Time Scale. In Gradstein, F.M., Ogg, J.G., Schmitz, M., and Ogg, G. (Eds.), Geologic Time Scale 2020. Amsterdam (Elsevier), 159–192. **https://doi.org/10.1016/B978-0-12-824360-2.00005-X**

Parsiegla, N., Gohl, K., and Uenzelmann-Neben, G., 2008. The Agulhas Plateau: structure and evolution of a Large Igneous Province. Geophysical Journal International, 174(1):336–350. **https://doi.org/10.1111/j.1365-246X.2008.03808.x**

Petrizzo, M.R., Watkins, D.K., MacLeod, K.G., Hasegawa, T., Huber, B.T., Batenburg, S.J., and Kato, T., 2021. Exploring the paleoceanographic changes registered by planktonic foraminifera across the Cenomanian-Turonian boundary interval and Oceanic Anoxic Event 2 at southern high latitudes in the Mentelle Basin (SE Indian Ocean). Global and Planetary Change, 206:103595. **https://doi.org/10.1016/j.gloplacha.2021.103595**

Pietsch, R., and Uenzelmann-Neben, G., 2015. The Manihiki Plateau—a multistage volcanic emplacement history. Geochemistry, Geophysics, Geosystems, 16(8):2480–2498. **https://doi.org/10.1002/2015GC005852**

Poulsen, C.J., Gendaszek, A.S., and Jacob, R.L., 2003. Did the rifting of the Atlantic Ocean cause the Cretaceous thermal maximum? Geology, 31(2):115–118. **https://doi.org/10.1130/0091-7613(2003)031<0115:DTROTA>2.0.CO;2**

Poulsen, C.J., and Zhou, J., 2013. Sensitivity of Arctic climate variability to mean state: insights from the Cretaceous. Journal of Climate, 26(18):7003–7022. **https://doi.org/10.1175/JCLI-D-12-00825.1**

Putirka, K., 2008. Excess temperatures at ocean islands: Implications for mantle layering and convection. Geology, 36(4):283–286. **https://doi.org/10.1130/G24615A.1**

Read, J.F., and Pollard, R.T., 1999. Deep inflow into the Mozambique Basin. Journal of Geophysical Research: Oceans, 104(C2):3075–3090. **https://doi.org/10.1029/1998JC900078**

Robinson, S.A., Murphy, D.P., Vance, D., and Thomas, D.J., 2010. Formation of "Southern Component Water" in the Late Cretaceous: evidence from Nd-isotopes. Geology, 38(10):871–874. **https://doi.org/10.1130/G31165.1**

Robinson, S.A., and Vance, D., 2012. Widespread and synchronous change in deep-ocean circulation in the North and South Atlantic during the Late Cretaceous. Paleoceanography and Paleoclimatology, 27(1):PA1102. **https://doi.org/10.1029/2011PA002240**

Royer, D.L., Berner, R.A., Montañez, I.P., Tabor, N.J., and Beerling, D.J., 2004. CO_2 as a primary driver of Phanerozoic climate. GSA Today, 14(3):3–10. **https://doi.org/10.1130/1052-5173(2004)014<4:CAAPDO>2.0.CO;2**

Sager, W.W., Kim, J., Klaus, A., Nakanishi, M., and Khankishieva, L.M., 1999. Bathymetry of Shatsky Rise, northwest Pacific Ocean: implications for ocean plateau development at a triple junction. Journal of Geophysical Research: Solid Earth, 104(B4):7557–7576. **https://doi.org/10.1029/1998JB900009**

Sager, W.W., Zhang, J., Korenaga, J., Sano, T., Koppers, A.A.P., Widdowson, M., and Mahoney, J.J., 2013. An immense shield volcano within the Shatsky Rise oceanic plateau, northwest Pacific Ocean. Nature Geoscience, 6(11):976–981. **https://doi.org/10.1038/ngeo1934**

Sandwell, D.T., and Smith, W.H.F., 1997. Marine gravity anomaly from Geosat and ERS 1 satellite altimetry. Journal of Geophysical Research: Solid Earth, 102(B5):10039–10054. **https://doi.org/10.1029/96JB03223**

Schlanger, S.O., and Jenkyns, H., 1976. Cretaceous oceanic anoxic events: causes and consequences. Geologie en Mijnbouw, 55.

Schlüter, H.U., and Uenzelmann-Neben, G., 2007. Seismostratigraphic analysis of the Transkei Basin: a history of deep sea current controlled sedimentation. Marine Geology, 240(1–4):99–111. **https://doi.org/10.1016/j.margeo.2007.02.015**

Schlüter, P., and Uenzelmann-Neben, G., 2008a. Conspicuous seismic reflections in Upper Cretaceous sediments as evidence for black shales off South Africa. Marine and Petroleum Geology, 25(10):989–999. **https://doi.org/10.1016/j.marpetgeo.2007.10.003**

Schlüter, P., and Uenzelmann-Neben, G., 2008b. Indications for bottom current activity since Eocene times: The climate and ocean gateway archive of the Transkei Basin, South Africa. Global and Planetary Change, 60(3–):416–428. **https://doi.org/10.1016/j.gloplacha.2007.07.002**

Sewall, J.O., van de Wal, R.S.W., van der Zwan, K., van Oosterhout, C., Dijkstra, H.A., and Scotese, C.R., 2007. Climate model boundary conditions for four Cretaceous time slices. Climate of the Past, 3(4):647–657. **https://doi.org/10.5194/cp-3-647-2007**

Sijp, W.P., von der Heydt, A.S., Dijkstra, H.A., Flögel, S., Douglas, P.M.J., and Bijl, P.K., 2014. The role of ocean gateways on cooling climate on long time scales. Global and Planetary Change, 119:1–22. **https://doi.org/10.1016/j.gloplacha.2014.04.004**

Sinninghe Damsté, J.S., van Bentum, E.C., Reichart, G.-J., Pross, J., and Schouten, S., 2010. A CO_2 decrease-driven cooling and increased latitudinal temperature gradient during the mid-Cretaceous Oceanic Anoxic Event 2. Earth and Planetary Science Letters, 293(1–2):97–103. **https://doi.org/10.1016/j.epsl.2010.02.027**

Sissingh, W., 1977. Biostratigraphy of Cretaceous calcareous nannoplankton. Geologie en Mijnbouw, 56:37–65.

Stracke, A., Hofmann, A.W., and Hart, S.R., 2005. FOZO, HIMU, and the rest of the mantle zoo. Geochemistry, Geophysics, Geosystems, 6(5):Q05007. **https://doi.org/10.1029/2004GC000824**

Tejada, M.L.G., Mahoney, J.J., Castillo, P.R., Ingle, S.P., Sheth, H.C., and Weis, D., 2004. Pin-pricking the elephant: evidence on the origin of the Ontong Java Plateau from Pb-Sr-Hf-Nd isotopic characteristics of ODP Leg 192 basalts. In Fitton, J.G., Mahoney, J.J., Wallace, P.J., and Saunders, A.D. (Eds.), Origin and Evolution of the Ontong

Java Plateau. Geological Society Special Publication, 229: 133–150. **https://doi.org/10.1144/GSL.SP.2004.229.01.09**

Tejada, M.L.G., Mahoney, J.J., Duncan, R.A., and Hawkins, M.P., 1996. Age and geochemistry of basement and alkalic rocks of Malaita and Santa Isabel, Solomon Islands, southern margin of Ontong Java Plateau. Journal of Petrology, 37(2):361–394. **https://doi.org/10.1093/petrology/37.2.361**

Tejada, M.L.G., Mahoney, J.J., Neal, C.R., Duncan, R.A., and Petterson, M.G., 2002. Basement geochemistry and geochronology of Central Malaita, Solomon Islands, with implications for the origin and evolution of the Ontong Java Plateau. Journal of Petrology, 43(3):449–484. **https://doi.org/10.1093/petrology/43.3.449**

Tetley, M.G., Williams, S.E., Gurnis, M., Flament, N., and Müller, R.D., 2019. Constraining absolute plate motions since the Triassic. Journal of Geophysical Research: Solid Earth, 124(7):7231–7258. **https://doi.org/10.1029/2019JB017442**

Timm, C., Hoernle, K., Werner, R., Hauff, F., van den Bogaard, P., Michael, P., Coffin, M.F., and Koppers, A., 2011. Age and geochemistry of the oceanic Manihiki Plateau, SW Pacific: new evidence for a plume origin. Earth and Planetary Science Letters, 304(1–2):135–146. **https://doi.org/10.1016/j.epsl.2011.01.025**

Toggweiler, J.R., and Russell, J., 2008. Ocean circulation in a warming climate. Nature, 451(7176):286–288. **https://doi.org/10.1038/nature06590**

Tomczak, M., and Godfrey, J.S., 1994. Hydrology of the Indian Ocean. In Tomczak, M., and Godfrey, J.S. (Eds.), Regional Oceanography. Amsterdam (Pergamon), 221–236. **https://doi.org/10.1016/B978-0-08-041021-0.50016-3**

Toole, J.M., and Warren, B.A., 1993. A hydrographic section across the subtropical South Indian Ocean. Deep Sea Research, Part I: Oceanographic Research Papers, 40(10):1973–2019. **https://doi.org/10.1016/0967-0637(93)90042-2**

Totterdell, J.M., Struckmeyer, H.I.M., Boreham, C.J., Mitchell, C.H., Monteil, E., and Bradshaw, B.E., 2008. Mid–Late Cretaceous organic-rich rocks from the eastern Bight Basin: implications for prospectivity. In Blevin, J.E., Bradshaw, B.E., and Uruski, C. (Eds.), Eastern Australasian Basins Symposium III. Petroleum Exploration Society of Australia Special Publication, 137–158.

Tsikos, H., Jenkyns, H.C., Walsworth-Bell, B., Petrizzo, M.R., Forster, A., Kolonic, S., Erba, E., Premoli Silva, I., Baas, M., Wagner, T., and Sinninghe Damsté, J.S., 2004. Carbon-isotope stratigraphy recorded by the Cenomanian–Turonian Oceanic Anoxic Event: correlation and implications based on three key localities. Journal of the Geological Society (London, UK), 161(4):711–719. **https://doi.org/10.1144/0016-764903-077**

Tucholke, B.E., and Carpenter, G.B., 1977. Sediment distribution and Cenozoic sedimentation patterns on the Agulhas Plateau. Geological Society of America Bulletin, 88(9):1337–1346. **https://doi.org/10.1130/0016-7606(1977)88<1337:SDACSP>2.0.CO;2**

Tucholke, B.E., Embley, R.W., and Schlee, J.S., 1984. Cenozoic regional erosion of the abyssal seafloor off South Africa. In Schlee, J.S., Interregional Unconformities and Hydrocarbon Accumulation. AAPG Memoir, 36: 145–164. **https://doi.org/10.1306/M36440C11**

Uenzelmann-Neben, G., 1998. Sedimentation and tectonics of Agulhas Ridge and Agulhas Plateau. Berichte zur Polar und Meeresforschung, 273:22.

Uenzelmann-Neben, G., 2001. Seismic characteristics of sediment drifts: an example from the Agulhas Plateau, southwest Indian Ocean. Marine Geophysical Research, 22(5):323–343. **https://doi.org/10.1023/A:1016391314547**

Uenzelmann-Neben, G., 2002. Contourites on the Agulhas Plateau, SW Indian Ocean: indications for the evolution of currents since Palaeogene times. In Stow, D.A.V., Pudsey, C.J., Howe, J.A., Faugères, J.-C., and Viana, A.R. (Eds.), Deep-Water Contourite Systems: Modern Drifts and Ancient Series, Seismic and Sedimentary Characteristics. Memoirs - Geological Society of London, 22: 271–288. **https://doi.org/10.1144/GSL.MEM.2002.022.01.20**

Uenzelmann-Neben, G., 2005. Southeastern Atlantic and southwestern Indian Ocean: reconstruction of the sedimentary and tectonic development since the Cretaceous AISTEK-1: Agulhas Transect. Berichte zur Polar- und Meeresforschung, 73.

Uenzelmann-Neben, G., 2010. Margins of Africa - the interdependency of deep and shallow studies. Presented at the Inkaba yeAfrica Annual Workshop, Potsdam, Germany.

Uenzelmann-Neben, G., 2014. The expedition of the research vessel "Sonne" to the Mozambique Ridge in 2014 (SO232): Bremerhaven, Germany (Alfred-Wegener-Institut).

Uenzelmann-Neben, G., Bohaty, S.M., and Kulhanek, D.K., 2020. Expedition 392 Scientific Prospectus: Agulhas Plateau Cretaceous Climate: International Ocean Discovery Program **https://doi.org/10.14379/iodp.sp.392.2020**

Uenzelmann-Neben, G., Gohl, K., Ehrhardt, A., and Seargent, M., 1999. Agulhas Plateau, SW Indian Ocean: new evidence for excessive volcanism. Geophysical Research Letters, 26(13):1941–1944. **https://doi.org/10.1029/1999GL900391**

Uenzelmann-Neben, G., and Huhn, K., 2009. Sedimentary deposits on the southern South African continental margin: Slumping versus non-deposition or erosion by oceanic currents? Marine Geology, 266(1):65–79. **https://doi.org/10.1016/j.margeo.2009.07.011**

Uenzelmann-Neben, G., Weber, T., Grützner, J., and Thomas, M., 2017. Transition from the Cretaceous ocean to Cenozoic circulation in the western South Atlantic — a twofold reconstruction. Tectonophysics, 716:225–240. **https://doi.org/10.1016/j.tecto.2016.05.036**

van Aken, H.M., Ridderinkhof, H., and de Ruijter, W.P.M., 2004. North Atlantic deep water in the south-western Indian Ocean. Deep Sea Research, Part I: Oceanographic Research Papers, 51(6):755–776. **https://doi.org/10.1016/j.dsr.2004.01.008**

van Hinsbergen, D.J.J., de Groot, L.V., van Schaik, S.J., Spakman, W., Bijl, P.K., Sluijs, A., Langereis, C.G., and Brinkhuis, H., 2015. A paleolatitude calculator for paleoclimate studies. PloS One, 10(6):e0126946. **https://doi.org/10.1371/journal.pone.0126946**

Voigt, S., Jung, C., Friedrich, O., Frank, M., Teschner, C., and Hoffmann, J., 2013. Tectonically restricted deep-ocean circulation at the end of the Cretaceous greenhouse. Earth and Planetary Science Letters, 369–370:169–177. **https://doi.org/10.1016/j.epsl.2013.03.019**

Westerhold, T., Marwan, N., Drury, A.J., Liebrand, D., Agnini, C., Anagnostou, E., Barnet, J.S.K., Bohaty, S.M., De Vleeschouwer, D., Florindo, F., Frederichs, T., Hodell, D.A., Holbourn, A.E., Kroon, D., Lauretano, V., Littler, K., Lourens, L.J., Lyle, M., Pälike, H., Röhl, U., Tian, J., Wilkens, R.H., Wilson, P.A., and Zachos, J.C., 2020. An astronomically dated record of Earth's climate and its predictability over the last 66 million years. Science, 369(6509):1383–1387. **https://doi.org/10.1126/science.aba6853**

You, Y., Lutjeharms, J.R.E., Boebel, O., and de Ruijter, W.P.M., 2003. Quantification of the interocean exchange of intermediate water masses around southern Africa. Deep Sea Research, Part II: Topical Studies in Oceanography, 50(1):197–228. **https://doi.org/10.1016/S0967-0645(02)00384-3**

Zhou, J., Poulsen, C.J., Pollard, D., and White, T.S., 2008. Simulation of modern and middle Cretaceous marine $\delta^{18}O$ with an ocean-atmosphere general circulation model. Paleoceanography and Paleoclimatology, 23(3):PA3223. **https://doi.org/10.1029/2008PA001596**

Zindler, A., and Hart, S., 1986. Chemical geodynamics. Annual Review of Earth and Planetary Sciences, 14:493–570. **https://doi.org/10.1146/annurev.ea.14.050186.002425**